# Jordan Journal of Mechanical and Industrial Engineering (JJMIE)

JJMIE is a high-quality scientific journal devoted to fields of Mechanical and Industrial Engineering. It is published by The Hashemite University in corporation with the Jordanian Scientific Research Support Fund.



## SUBMISSION ADDRESS:


Prof. **Nabil Anagreh** , Editor-in-Chief
Jordan Journal of Mechanical & Industrial Engineering,
Hashemite University,
PO Box 330127, Zarqa, 13133 , Jordan
E-mail: jjmie@hu.edu.jo

Hashemite Kingdom of Jordan

Hashemite University

# Jordan Journal of
# Mechanical and Industrial Engineering

# JJMIE

*An International Peer-Reviewed Scientific Journal*

*Financed by Scientific Research Support Fund*

http://jjmie.hu.edu.jo/

ISSN 1995-6665

# Jordan Journal of Mechanical and Industrial Engineering (JJMIE)

JJMIE is a high-quality scientific journal devoted to fields of Mechanical and Industrial Engineering. It is published by The Jordanian Ministry of Higher Education and Scientific Research in corporation with the Hashemite University.

**Introduction:** The Editorial Board is very committed to build the Journal as one of the leading international journals in mechanical and industrial engineering sciences in the next few years. With the support of the Ministry of Higher Education and Scientific Research and Jordanian Universities, it is expected that a heavy resource to be channeled into the Journal to establish its international reputation. The Journal's reputation will be enhanced from arrangements with several organizers of international conferences in publishing selected best papers of the conference proceedings.

**Aims and Scope:** *Jordan Journal of Mechanical and Industrial Engineering* (JJMIE) is a refereed international journal to be of interest and use to all those concerned with research in various fields of, or closely related to, mechanical and industrial engineering disciplines. *Jordan Journal of Mechanical and Industrial Engineering* aims to provide a highly readable and valuable addition to the literature which will serve as an indispensable reference tool for years to come. The coverage of the journal includes all new theoretical and experimental findings in the fields of mechanical and industrial engineering or any closely related fields (Materials, Manufacturing, Management, Design, Thermal and Fluid, Energy, Control, Mechatronics, and Biomedical). The journal also encourages the submission of critical review articles covering advances in recent research of such fields as well as technical notes.

## Guide for Authors

**Manuscript Submission:**
High-quality submissions to this new journal are welcome now and manuscripts may be either submitted online or email.

**Online:** For online and email submission upload one copy of the full paper including graphics and all figures at the online submission site, accessed via http://jjmie.hu.edu.jo. The manuscript must be written in MS Word 2010 Format. All correspondence, including notification of the Editor's decision and requests for revision, takes place by e-mail and via the Author's homepage, removing the need for a hard-copy paper trail.

**Submission address and contact:**
Prof. Nabil Anagreh
Editor-in-Chief
*Jordan Journal of Mechanical & Industrial Engineering,*
Hashemite University,
PO Box 330127, Zarqa, 13115, Jordan
E-mail: jjmie@hu.edu.jo

**Types of contributions***:* Original research papers and Technical reports

**Corresponding author:** Clearly indicate who is responsible for correspondence at all stages of refereeing and publication, including post-publication. Ensure that telephone and fax numbers (with country and area code) are provided in addition to the e-mail address and the complete postal address. Full postal addresses must be given for all co-authors.

**Original material:** Submission of an article implies that the work described has not been published previously (except in the form of an abstract or as part of a published lecture or academic thesis), that it is not under consideration for publication elsewhere, that its publication is approved by all authors and that, if accepted, it will not be published elsewhere in the same form, in English or in any other language, without the written consent of the Publisher. Authors found to be deliberately contravening the submission guidelines on originality and exclusivity shall not be considered for future publication in this journal.

**Withdrawing:** If the author chooses to withdraw his article after it has been assessed, he shall reimburse JJMIE with the cost of reviewing the paper.

## Manuscript Preparation:

**General:** Editors reserve the right to adjust style to certain standards of uniformity. Original manuscripts are discarded after publication unless the Publisher is asked to return original material after use. Please use MS Word 2010 for the text of your manuscript.

**Structure:** Follow this order when typing manuscripts: Title, Authors, Authors title, Affiliations, Abstract, Keywords, Introduction, Main text, Conclusions, Acknowledgements, Appendix, References, Figure Captions, Figures and then Tables. Please supply figures imported into the text AND also separately as original graphics files. Collate acknowledgements in a separate section at the end of the article and do not include them on the title page, as a footnote to the title or otherwise.

**Text Layout:** Use 1.5 line spacing and wide (3 cm) margins. Ensure that each new paragraph is clearly indicated. Present tables and figure legends on separate pages at the end of the manuscript. If possible, consult a recent issue of the journal to become familiar with layout and conventions. All footnotes (except for table and corresponding author footnotes) should be identified with superscript Arabic numbers. To conserve space, authors are requested to mark the less important parts of the paper (such as records of experimental results) for printing in smaller type. For long papers (more than 4000 words) sections which could be deleted without destroying either the sense or the continuity of the paper should be indicated as a guide for the editor. Nomenclature should conform to that most frequently used in the scientific field concerned. Number all pages consecutively; use 12 or 10 pt font size and standard fonts.

**Corresponding author:** Clearly indicate who is responsible for correspondence at all stages of refereeing and publication, including post-publication. The corresponding author should be identified with an asterisk and footnote. Ensure that telephone and fax numbers (with country and area code) are provided in addition to the e-mail address and the complete postal address. Full postal addresses must be given for all co-authors. Please consult a recent journal paper for style if possible.

**Abstract:** A self-contained abstract outlining in a single paragraph the aims, scope and conclusions of the paper must be supplied.

**Keywords:** Immediately after the abstract, provide a maximum of six keywords (avoid, for example, 'and', 'of'). Be sparing with abbreviations: only abbreviations firmly established in the field may be eligible.

**Symbols:** All Greek letters and unusual symbols should be identified by name in the margin, the first time they are used.

**Units:** Follow internationally accepted rules and conventions: use the international system of units (SI). If other quantities are mentioned, give their equivalent in SI.

**Maths:** Number consecutively any equations that have to be displayed separately from the text (if referred to explicitly in the text).

**References:** All publications cited in the text should be presented in a list of references following the text of the manuscript.

*Text:* Indicate references by number(s) in square brackets in line with the text. The actual authors can be referred to, but the reference number(s) must always be given.

*List:* Number the references (numbers in square brackets) in the list in the order in which they appear in the text.

**Examples:**

**Reference to a journal publication:**

[1] M.S. Mohsen, B.A. Akash, "Evaluation of domestic solar water heating system in Jordan using analytic hierarchy process". Energy Conversion & Management, Vol. 38 (1997) No. 9, 1815-1822.

**Reference to a book:**

[2] Strunk Jr W, White EB. The elements of style. 3rd ed. New York: Macmillan; 1979.

**Reference to a conference proceeding:**

[3] B. Akash, S. Odeh, S. Nijmeh, "Modeling of solar-assisted double-tube evaporator heat pump system under local climate conditions". 5th Jordanian International Mechanical Engineering Conference, Amman, Jordan, 2004.

**Reference to a chapter in an edited book:**

[4] Mettam GR, Adams LB. How to prepare an electronic version of your article. In: Jones BS, Smith RZ, editors. Introduction to the electronic age, New York: E-Publishing Inc; 1999, p. 281-304

**Free Online Color :** If, together with your accepted article, you submit usable color and black/white figures then the journal will ensure that these figures will appear in color on the journal website electronic version.

**Tables:** Tables should be numbered consecutively and given suitable captions and each table should begin on a new page. No vertical rules should be used. Tables should not unnecessarily duplicate results presented elsewhere in the manuscript (for example, in graphs). Footnotes to tables should be typed below the table and should be referred to by superscript lowercase letters.

**Notification:** Authors will be notified of the acceptance of their paper by the editor. The Publisher will also send a notification of receipt of the paper in production.

**Copyright:** All authors must sign the Transfer of Copyright agreement before the article can be published. This transfer agreement enables Jordan Journal of Mechanical and Industrial Engineering to protect the copyrighted material for the authors, but does not relinquish the authors' proprietary rights. The copyright transfer covers the exclusive rights to reproduce and distribute the article, including reprints, photographic reproductions, microfilm or any other reproductions of similar nature and translations.

**Proof Reading:** One set of page proofs in MS Word 2010 format will be sent by e-mail to the corresponding author, to be checked for typesetting/editing. The corrections should be returned within **48 hours**. No changes in, or additions to, the accepted (and subsequently edited) manuscript will be allowed at this stage. Proofreading is solely the author's responsibility. Any queries should be answered in full. Please correct factual errors only, or errors introduced by typesetting. Please note that once your paper has been proofed we publish the identical paper online as in print.

**Author Benefits:**

*No page charges:* Publication in this journal is free of charge.

*Free offprints:* One journal issues of which the article appears will be supplied free of charge to the corresponding author and additional offprint for each co-author. Corresponding authors will be given the choice to buy extra offprints before printing of the article.

JJMIE

Volume 9 Number 2, April.2015
ISSN 1995-6665
Pages 75 - 84

Jordan Journal of Mechanical and Industrial Engineering

# Controlling of Chaos Synchronization

Mohammad Ababneh *

*Mechatronics Engineering Department, the Hashemite University, 13115 Zarqa, Jordan*

*Received 15 Feb 2015* *Accepted 29 March 2015*

**Abstract**

In the present paper, Linear Quadratic Regulator (LQR) and dual properties are employed to solve the observer-based synchronization problem. The synchronization is designed for nominal chaotic system, then it is applied to systems with uncertain parameters and systems with time-delays to investigate its tolerance to such systems. Moreover, to solve the nonlinear problem, which exist in chaotic systems, the optimal linearization technique is adopted to transform the nonlinear system into equivalent linear models. By linearizing the chaotic system and constructing linear models at every operating point, and then applying algebraic Riccati equation, the observer design problem is solved and chaotic synchronization is established. Numerical Simulations are used to demonstrate the effectiveness and feasibility of this design.



**Keywords:** *Chaos Synchronization, LQR, Observer Based Design, Chaotic Systems.*

## 1. Introduction

The investigation of chaos synchronization has been an active research topic in recent years [1-3]. Its applications are found in many engineering systems, such as mechanical systems, electromechanical systems, and industrial systems. For example, the Horizontal Platform System (HPS) is a mechanical system that exhibits rich chaotic dynamics and its synchronization was investigated in [4]. The drive and response systems were assumed to be disturbed by model uncertainties and external disturbances, the system parameters were assumed to be well-known. Using the update laws and the finite-time control theory, a robust adaptive controller was derived to synchronize the two uncertain systems in a finite time.

Furthermore, an adaptive synchronization method for a chaotic Permanent Magnet Synchronous Motor (PMSM) was developed in [5]. An adaptive synchronization method for a chaotic permanent magnet synchronous motor under model parameter variations was presented. Convergence of the closed-loop system responses was achieved by using a Lyapunov function.

Moreover, the synchronization and control of a chaotic supply chain management system was presented in [6]. The synchronization was performed using Lyapunov stability theory. And synchronization and control of chaotic supply chain management system were realized numerically.

Synchronization of chaos occurs when two systems adjust their motion to each other due to a coupling between them. It is important to highlight the relevance of chaos synchronization, especially in mechanical systems, optics and fluid dynamics. Furthermore, handling the parameter uncertainties and time delays is key element in the line of research. For example, in [7], Fourier series expansion and adaptive bounding technique were used to deal with periodical uncertainty. Using Lyapunov stability theory, the adaptive controller accomplished a hybrid function projective synchronization of a class of chaotic system with unknown time-varying parameters. Then using parameter updating laws, the nominal values of the unknown time-varying parameters were estimated.

However, in [8], only an adaptive bounding technique was used to handle such systems, where the master-slave synchronization problem of chaotic Lur'e systems was investigated. Only quantized sampled measurements were available for the controller. Using Lyapunov functional, an exponential asymptotical synchronization of master and slave system was achieved.

Moreover, in [9], the synchronization of chaos systems using fuzzy logic was addressed, where synchronization was achieved for uncertain nonlinear system with parameter uncertainties. The fuzzy modeling of chaotic systems using the Takagi-Sugeno (TS) model was used to provide many linearized systems for the nonlinear system under consideration. Then, the uncertainty decomposition was worked out by incorporating the uncertainties of the chaotic system in the fuzzy linear model. Where the uncertain chaotic system was expressed as set of linear models. Afterwards, an observer-based synchronization was performed for each linear model, and synchronization performed as the solution to a linear matrix inequality problem.

* Corresponding author. e-mail: ababneh@hu.edu.jo.

In all the studies mentioned above, complex mathematical models with computationally demanding approaches were required. Motivated by this reason, LQR method, which is a simpler and a more efficient method, was chosen for the present work [10, 11]. Therefore, the LQR and dual properties are employed to solve the observer-based synchronization problem from control point of view. And the chaos synchronization is applied to systems with uncertain parameters and systems with time-delays to investigate its tolerance to such systems. In order to highlight the advantage of this method, a comparison of its performance and the one's in [9] is made at the end of section 5.

The rest of the present paper is organized as follows. In section 2, the design of chaotic synchronized systems is presented. In section 3, the optimal linear method is discussed and the generation of linearized models around operating points is shown. In section 4, the linear quadratic control is discussed and the observer-based synchronization is derived. In Section 5, the effectiveness of the optimal linear model is demonstrated as simulation results, and discussion of these results is conducted in the same section. Finally, conclusions are presented in section 6.

## 2. Design of Chaotic Synchronized Systems

In the present paper, the observer approach is used to synchronize response system to drive system subjected to parameter uncertainties or time delays. Synchronization occurs when the states of the response system track the states of the drive system as time tends to infinity. Now, consider the following uncertain and time-delayed nonlinear drive system:

$$\begin{aligned} \dot{x}_c(t) &= f\,(x_c(t-t_0),\rho) \\ y_c(t) &= C\,(x_c(t-t_0),\rho) \end{aligned} \tag{1}$$

and a nominal nonlinear response system in the form:

$$\begin{aligned} \dot{\hat{x}}_c(t) &= \hat{f}\,(\hat{x}_c(t)) \qquad \hat{x}_c(0) = x_o \\ \hat{y}_c(t) &= C\,(\hat{x}_c(t)) \end{aligned} \tag{2}$$

where $f:\Re^n \to \Re^n$ and $\hat{f}:\Re^n \to \Re^n$ are nonlinear functions, $x_c(t) \in \Re^n$ $\hat{x}_c(t) \in \Re^n$ are the state vectors for the drive and response systems, $\rho \in \Re^p$ represents the parameter uncertainty and $t_0$ represents the delay time. Also, $y_c(t) \in \Re^n$ and $\hat{y}_c(t) \in \Re^n$ are the output vectors for the drive and response, respectively, and $C$ is the constant output matrix.

There are many definitions of synchronization available in the literature; a working definition is to consider that the response system is synchronized to the drive system if the following criterion is satisfied [12]:

$$\lim_{t\to\infty}\left\| x(t) - \hat{x}(t) \right\| = 0 \tag{3}$$

The synchronization phenomenon may be viewed as an observer-design problem, and depending on the structure of the system, different approaches may be possible. Therefore, it is essential to have an observer-design, such that the error signal converges to zero globally and asymptotically, in this way the response is synchronized to the drive in the sense of equation (3). Noting that the chaotic systems in equations (1) and (2) are highly nonlinear, we shall introduce a technique for the linearization in the following section.

## 3. Optimal Linearization Method

Our approach in the present paper starts with Optimal Linearization Method (OLM) [13], in which a local linear model around every operating point of the system trajectory is obtained. Therefore, we deal with many linear models instead of one nonlinear model. Furthermore, OLM minimizes the modeling error between the original nonlinear system and its local linear model around each operating point of the system trajectory.

Now, consider a family of nonlinear systems of the form:

$$\dot{x}(t) = f(x(t)) + g(x(t))u(t) \tag{4}$$

where $f:\Re^n \to \Re^n$ and $g:\Re^n \to \Re^{n\times m}$ are smooth nonlinear functions, $x(t) \in \Re^n$ is the state vector, and $u(t) \in \Re^m$ is the control input.

Suppose that it is desired to find a linear model $(A_j, B_j)$ around an operating point $x_j$, in the form:

$$\dot{x}(t) = A_j x(t) + B_j u(t) \tag{5}$$

with $A_j$ and $B_j$ being constant matrices of appropriate dimensions. One way to do this is to use the truncated Taylor expansion; however, if the operating point is not the origin, this will result in affine rather than a linear model. And in general the model is not local in both the state and the control terms.

The basic idea is to construct a local linear model, in both *x* and *u*, that approximates the dynamical behavior of the original nonlinear system in the vicinity of the operating state $x_j$; therefore, it is necessary to find two constant matrices, $A_j$ and $B_j$, in the vicinity of operating point $x_j$ such that the following two condition are satisfied:

$$f(x(t)) + g(x(t))u(t) \approx A_j\, x(t) + B_j\, u(t) \tag{6}$$

$$f(x_j) + g(x_j)u(t) = A_j\, x_j + B_j\, u(t) \tag{7}$$

Since the control input $u(t)$ is arbitrary, one should choose:

$$B_j = g(x_j) \tag{8}$$

So that equations (6) and (7) become quite simple:

$$f\,(x\,(t)) \approx A_j x\,(t) \tag{9}$$

and:

$$f\,(x_j) = A_j x_j\,. \tag{10}$$

Let $a_i^T$ denotes the *ith* row of matrix $A_j$, then equations (9) and (10) can be rewritten as:

$$f_i(x(t)) \approx a_i^T x, \quad i = 1,2,...,n \tag{11}$$

and:

$$f_i(x_j) = a_i^T x_j, \quad i = 1,2,...,n \tag{12}$$

where $f_i : \Re^n \to \Re^n$ is the *ith* row of function $f$. Then, expanding the left-hand side of equation (11) about $x_j$, and neglecting the second and higher order terms since they relatively small, we obtain:

$$f_i(x_j) + [\nabla f_i(x_j)]^T (x(t) - x_j) \approx a_i^T x(t) \tag{13}$$

where $\nabla f_i(x_j) : \Re^n \to \Re^n$ is the gradient column-vector of $f_i$ evaluated at $x_j$. Using equation (12), one can rewrite equation (13) as:

$$[\nabla f_i(x_j)]^T (x(t) - x_j) \approx a_i^T (x(t) - x_j) \tag{14}$$

in which $x(t)$ is arbitrary state but should be close to $x_j$ for a good approximation.

To determine a constant vector $a_i^T$ such that it is close as much as possible to $\left[\nabla f_i(x_j)\right]^T$ and also satisfies $a_i^T x_j = f_i(x_j)$, we may consider the following constrained minimization problem:

$$\min \ E = \frac{1}{2}\left\|\nabla f_i(x_j) - a_i\right\|_2^2 \ \text{ subject to}$$

$$a_i^T x_j = f_i(x_j) \tag{15}$$

Notice that this is a convex constrained optimization problem. Therefore, the first order necessary condition for a minimization of E is also sufficient, which is:

$$\nabla_{a_i} E + \lambda \nabla_{a_i} (a_i^T x_j - f_i(x_j)) = 0 \tag{16}$$

where:

$$a_i^T x_j = f_i(x_j) \tag{17}$$

in which $\lambda$ is the Lagrange multiplier and the subscript $a_i$ in $\nabla_{a_i}$ indicates that the gradient is taken with respect to $a_i$. This then results in:

$$a_i - \nabla f_i(x_j) + \lambda x_j = 0, \tag{18}$$

By solving equation (18) with $x_j \neq 0$, this results in:

$$\lambda = \frac{x_j^T \nabla f_i(x_j) - f_i(x_j)}{\left\|x_j\right\|_2^2} x_j, \tag{19}$$

Substituting equation (19) into equation (18) for $\lambda$, for both $x_j \neq 0$ and $x_j = 0$, yields:

$$a_i = \begin{bmatrix} \nabla f_i(x_j) + \dfrac{f_i(x_j) - x_j^T \nabla f_i(x_j)}{\left\|x_j\right\|_2^2} x_j & , x_j \neq 0 \\ \nabla f_i(x_j) \ , & x_j = 0 \end{bmatrix} \tag{20}$$

Note that equation (20) is the linearized systems taken at the operating points of the system trajectory. To this end, the subject of the present paper and the optimal linearization method have been introduced. In the following section, the LQR and observer-based synchronization is discussed.

## 4. Linear Quadratic Control

An important case of optimal control is the Linear Quadratic Regulator (LQR), where a measure of the quadratic continuous time cost function:

$$J = \tfrac{1}{2}\int_0^\infty \left[X^T(t)Q(t)X(t) + u^T(t)R(t)u(t)\right] dt \tag{21}$$

is minimized. Subject to linear dynamic constraints as given in the linearized models from the previous section, the $Q$ and $R$ matrices are positive definite matrices to ensure the cost measure remain positive. In addition, the negative feedback controller is in the form:

$$u(t) = -Kx(t) \tag{22}$$

It has been shown in optimal control theory that the feedback controller $K$ is given by $K = R^{-1}B^T S$ where S is the solution of the well-known Algebraic Riccati equation[14]:

$$A^T S + SA - SBR^{-1}B^T S + Q = 0 \tag{23}$$

where $S$ is symmetrical solution matrix. Note that the relationship between problem of state feedback controller and problem of observer design is duality relationship. In other words, both problems have similar solutions. Moreover, if we have a system of ($A$, $B$, $C$), then the system ($A^T$, $C^T$, $B^T$) is known as the dual system [15].

In general, the closed-loop system is given by:

$$\dot{x}(t) = (A - BK)x(t) \tag{24}$$

and the observer design is given by:

$$\dot{\hat{x}}(t) = A\hat{x}(t) - Bu(t) + L\left(y(t) - \hat{y}(t)\right) \tag{25}$$

and:

$$\hat{y}(t) = C\hat{x}(t) \tag{26}$$

where the $L$ is observer matrix, then the error dynamics is $e(t) = \dot{x}(t) - \dot{\hat{x}}(t)$ and:

$$\dot{e}(t) = (A - LC)e(t). \tag{27}$$

We can clearly see that error dynamic of equation (27) is dual to closed loop system of:

$$AS_e + S_e A^T - S_e C^T R^{-1} C S_e + Q = 0 \tag{28}$$

where $S_e$ is symmetrical solution matrix, and using duality property the observer matrix can be calculated as $L = S_e C^T R^{-1}$.

## 5. Simulation Results and Discussions

Observer-based synchronization is accomplished by forcing the error dynamics to zero as expressed in equation (3). This synchronization is performed for every linearized system $A_j$ of equation (7) around every operating point $x_j$ of the trajectory. In this section, simulation is implemented using two typical systems: Chua circuit and Chen system. The dimensionless form of Chua circuit is obtained as [16]:

$$\begin{aligned} \dot{x}_1(t) &= \alpha\left[x_2(t) - x_1(t) - g_{NL}(x_1(t))\right] \\ \dot{x}_2(t) &= x_1(t) - x_2(t) + x_3(t) \\ \dot{x}_3(t) &= -\beta x_2(t) \end{aligned} \tag{29}$$

where $g_{NL}(x_1(t)) = m_2 x_1(t) + m_3 x_1(t)^3$. The system has a complex attractor with nominal parameters $\alpha = 9, \beta = (14\frac{2}{7}), m_2 = -5/7, m_3 = -8/7$.

Referring back to section 3, the OLM for the Chua's linearized system was calculated as:

$$A_j \begin{cases} \begin{bmatrix} \alpha(m_2-1) - 3\alpha m_3 x_1^2 + \dfrac{2\alpha m_3 x_1^4}{\|x_j\|_2^2} & \alpha + \dfrac{2\alpha m_3 x_1^3 x_2}{\|x_j\|_2^2} & \dfrac{2\alpha m_3 x_1^3 x_3}{\|x_j\|_2^2} \\ 1 & -1 & 1 \\ 0 & -\beta & 0 \end{bmatrix} & for\ \|x_j\|_2^2 \neq 0 \\ \begin{bmatrix} \alpha(m_2-1) - 3\alpha m_3 x_1^2 & \alpha & 0 \\ 1 & -1 & 1 \\ 0 & -\beta & 0 \end{bmatrix} & for\ \|x_j\|_2^2 = 0 \end{cases} \tag{30}$$

After finding the linearized model, the drive state vector $\begin{bmatrix} x_1 & x_2 & x_3 \end{bmatrix}^T$ and its synchronized drive states vector $\begin{bmatrix} \hat{x}_1 & \hat{x}_2 & \hat{x}_3 \end{bmatrix}^T$ were found using equations (24) and (25), the synchronization was performed using Matlab ® with a Runge Kutta fourth-order algorithm, with a fixed integration step $\tau = 0.005$ seconds. At first, the synchronization was performed for nominal case without uncertainty and without time delay, and the simulation is shown in Figure 1, with excellent synchronization performance where response states follow drive states perfectly when time passes. Then time varying parameters uncertainties were introduced in the drive system as following:

$\alpha + \Delta\alpha = (9)(1 + \zeta \sin(10t)),$

$\beta + \Delta\beta = (14\frac{2}{7})(1 + \zeta \sin(10t)),$

and

$m_2 + \Delta m_2 = (\frac{-5}{7})(1 + \zeta \sin(10t)),$

$m_3 + \Delta m_3 = (\frac{-8}{7})(1 + \zeta \sin(10t)),$

where $\zeta$ is the percentage uncertainty. Then, nominal synchronization is applied to this uncertain drive and its performance is shown in Figure 2 with $\zeta = 10\%$; the response shows some deterioration especially in $X_2$ state. To better understand the effect of uncertainty, a measure of performance was introduces as follows:

$$\sum_{j=1}^{3} \sum_{i=1}^{n} \left( \frac{|x_i(t) - \hat{x}_i(t)|}{n} \right)_j \tag{31}$$

where $i$ represents the operating point and $j$ represents the trajectory, the tracking error for all points at increasing uncertainties in all three trajectories were taken, and then summed, averaged by the total number of sampling points, and recorded in Table 1. Note the measure worsening with the increasing of parameter uncertainty, where, roughly, the measure doubled with a small increase of uncertainty. Normalizing the measure by dividing the measures by the maximum range of trajectories, gives a better understating of the changes subjected to increasing parameter uncertainty as shown in Table 1. Note that 'the maximum range of trajectories' is the difference between the maximum value and the minimum value of the drive trajectories' points

A similar action was taken with time delay system, where the nominal synchronization was applied to the time delayed drive; the synchronization performance is shown in Figure 3 for 0.2 second delay. The delay of about 0.2 seconds was obvious in all trajectories; however, if the effect of delay is neglected, it is noted that the response states follow the drive states closely. Table 2 records the measures and normalized measures that were explained above; these readings show that the measures worsen with the increase of the delay at a steady rate.

The second typical chaotic system is Chen system which is expressed as [17]:

$$\begin{bmatrix} \dot{x}_1(t) \\ \dot{x}_2(t) \\ \dot{x}_3(t) \end{bmatrix} = \begin{bmatrix} a\ \ (x_2(t) - x_1(t)) \\ (c-a)\ \ x_1(t) - x_1(t)x_3(t) + c\,x_2(t) \\ x_1(t)x_2(t) - b\ \ x_3(t) \end{bmatrix} \tag{32}$$

The system has a complex attractor with nominal parameters $a = 35, b = 3, c = 28$. Referring back to section 3, the OLM for the Chen linearized system was calculated as:

$$A_j\begin{cases}\begin{bmatrix}-a & a & 0\\ c-a-x_{j3}+\dfrac{x_{j1}^2x_{j3}}{\|x_j\|_2^2} & c+\dfrac{x_{j1}x_{j2}x_{j3}}{\|x_j\|_2^2} & -x_{j1}+\dfrac{x_{j1}x_{j3}^2}{\|x_j\|_2^2}\\ x_{j2}-\dfrac{x_{j1}^2x_{j2}}{\|x_j\|_2^2} & x_{j1}-\dfrac{x_{j1}x_{j2}^2}{\|x_j\|_2^2} & -b-\dfrac{x_{j1}x_{j2}x_{j3}}{\|x_j\|_2^2}\end{bmatrix} & for\quad \|x_j\|_2^2\neq 0\\ \begin{bmatrix}-a & a & 0\\ c-a-x_{j3} & c & -x_{j1}\\ x_{j2} & x_{j1} & -b\end{bmatrix} & for\quad \|x_j\|_2^2=0\end{cases} \tag{33}$$

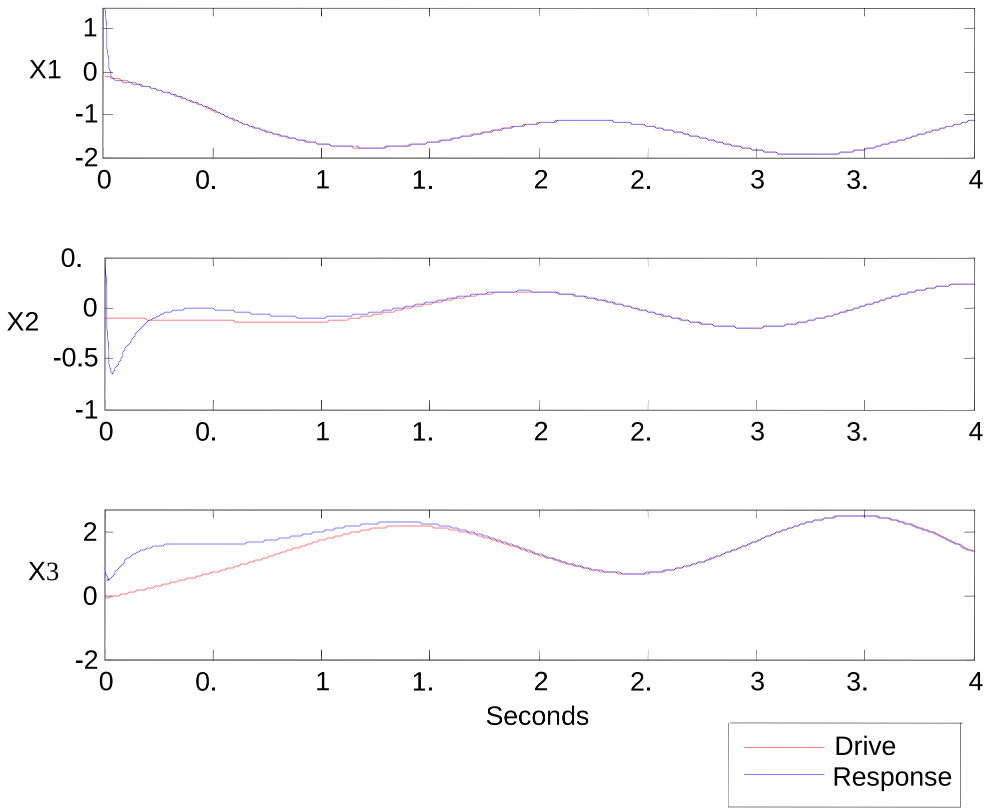


**Figure 1.** Nominal Chua's circuit synchronization

 

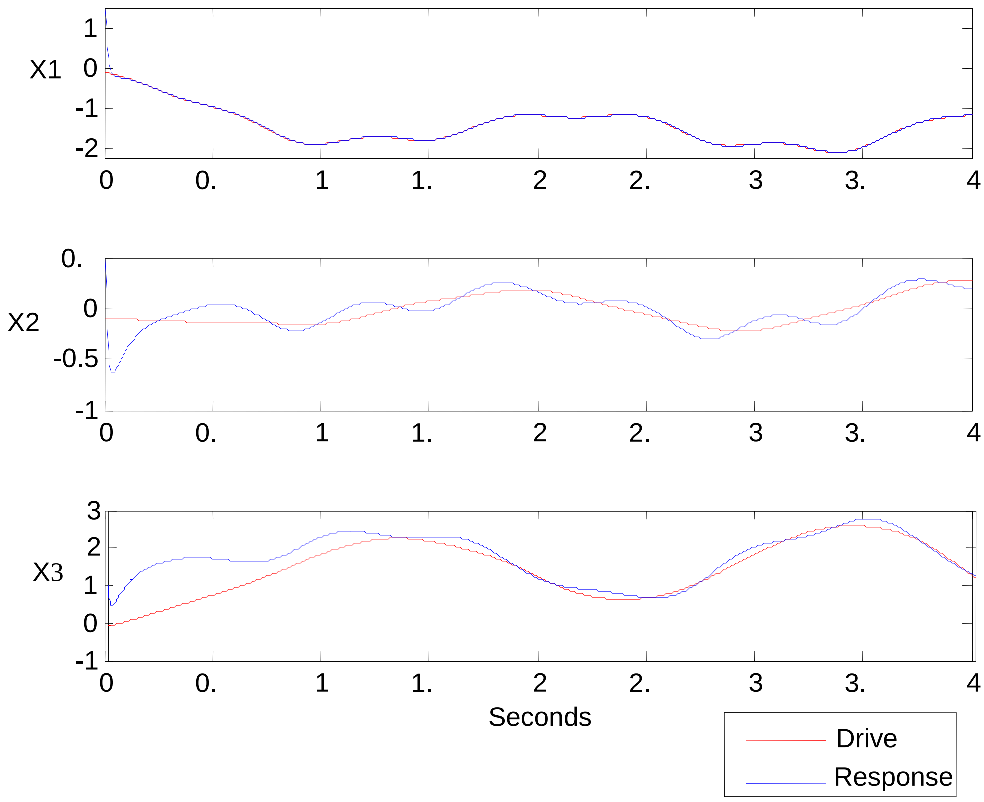


**Figure 2.** Chua's circuit synchronization with $\zeta = 10\%$

**Table 1**. Chua circuit synchronization subjected to increasing uncertainty

| Type | Nominal | 10% | 20% | 30% | 40% | 50% | 60% |
|---|---|---|---|---|---|---|---|
| Measure | 0.0094 | 0.0132 | 0.0196 | 0.0311 | 0.0499 | 0.0796 | 0.1287 |
| Normalized Measure | 0.0021 | 0.0030 | 0.0044 | 0.0070 | 0.0112 | 0.0179 | 0.0289 |
| Type | 70% | 80% | 90% | 100% | 110% | 120% | 200% |
| Measure | 0.2209 | 0.4738 | 1.9272 | 16.5683 | 203.7033 | 30181 | $3.2*10^{17}$ |
| Normalized Measure | 0.0496 | 0.1065 | 0.4331 | 3.7235 | 45.7801 | 6782.9 | $7.2*10^{17}$ |

**Table 2.** Chua's circuit synchronization subjected to increasing time delay

| Delay | Nominal | 0.025 sec | 0.050 sec | 0.075 sec | 0.1 sec | 0.2 sec | 0.3 sec |
|---|---|---|---|---|---|---|---|
| Measure | 0.0094 | 0.0668 | 0.0967 | 0.1266 | 0.1563 | 0.2764 | 0.3949 |
| Normalized Measure | 0.0021 | 0.0150 | 0.0217 | 0.0285 | 0.0351 | 0.0621 | 0.0887 |
| Delay | 0.4 sec | 0.5 sec | 0.6 sec | 0.7 sec | 0.8 sec | 0.9 sec | 1.0 sec |
| Measure | 0.5065 | 1.8261 | 0.6993 | 0.7759 | 0.8376 | 0.8839 | 0.9145 |
| Normalized Measure | 0.1138 | 0.4104 | 0.1572 | 0.1744 | 0.1882 | 0.1986 | 0.2055 |

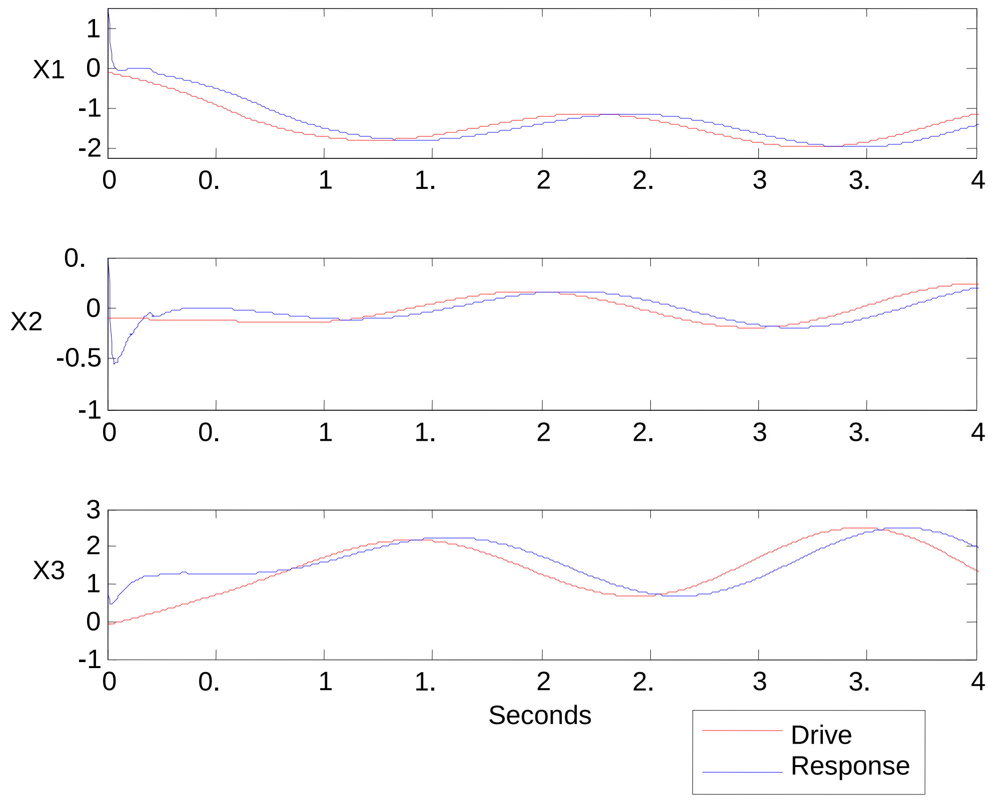


**Figure 3**.Chua's circuit synchronization subjected to a 0.2 second delay

Now, the drive state vector $[x_1 \quad x_2 \quad x_3]^T$ and its synchronized drive states vector $[\hat{x}_1 \quad \hat{x}_2 \quad \hat{x}_3]^T$ were found using equations (24) and (25), the synchronization was performed using Matlab ® with a Runge Kutta fourth-order algorithm, with a fixed integration step $\tau = 0.005$ seconds. At first the synchronization was performed for nominal case without uncertainty neither time delay, and the simulation is shown in Figure 4, with excellent synchronization performance were response states follow drive states perfectly when time elapses. Then time varying parameters uncertainties were introduced in the drive system as following:

$$b + \Delta b = (3)(1 + \zeta \sin(10t)),$$
$$a + \Delta a = (35)(1 + \zeta \sin(10t))$$
$$c + \Delta c = (28)(1 + \zeta \sin(10t)),$$

where $\zeta$ is the percentage uncertainty. And nominal synchronization applied to this uncertain drive and its performance is shown in Figure 5 with $\zeta = 30\%$, the response shows some deterioration; however, it was noted that the Chen system performed much better than the Chua circuit at low parameter uncertainties. And this is clear when comparing Table 1 with Table 3. To better understand the effect of uncertainty, a measure of performance for increasing uncertainties was recorded in Table 3. Note the measure worsening with the increase of parameter uncertainty at a steady rate, then reach the instability at $\zeta = 170\%$. Normalizing the measure, as explained above, gives a better understating of the changes subjected to the increase of parameter uncertainty as shown in Table 3, where the normalized measure was relatively low for $\zeta \leq 100\%$.

A similar action was taken with time delay system, where the nominal synchronization is applied to the time delayed drive; the synchronization performance is shown in Figure 6 for 0.2 second delay. The delay of about 0.2 seconds was obvious in all trajectories; however, if the effect of the delay is neglected, the response states follow the drive states closely, and this is similar to the performance in Chua circuit. Table 4 records the measures and normalized measures that were explained above; the measures worsen with the increase of the delay. However, the measure after 0.5 seconds started to fluctuate by decreasing then increasing; this is due to the distortion in the response signal because of the significant delay; it is also due to the fast dynamics of the Chen system.

Comparing this method with other methods, as the one in [9], will highlight the advantage of this method. The Chua circuit with parameter uncertainties was chosen to perform the comparison. As recorded in Table 5 below, most of the cases of parameter uncertainties shown a better performance in this method than the one in [9]. Therefore, this indicates the efficiency of this method.

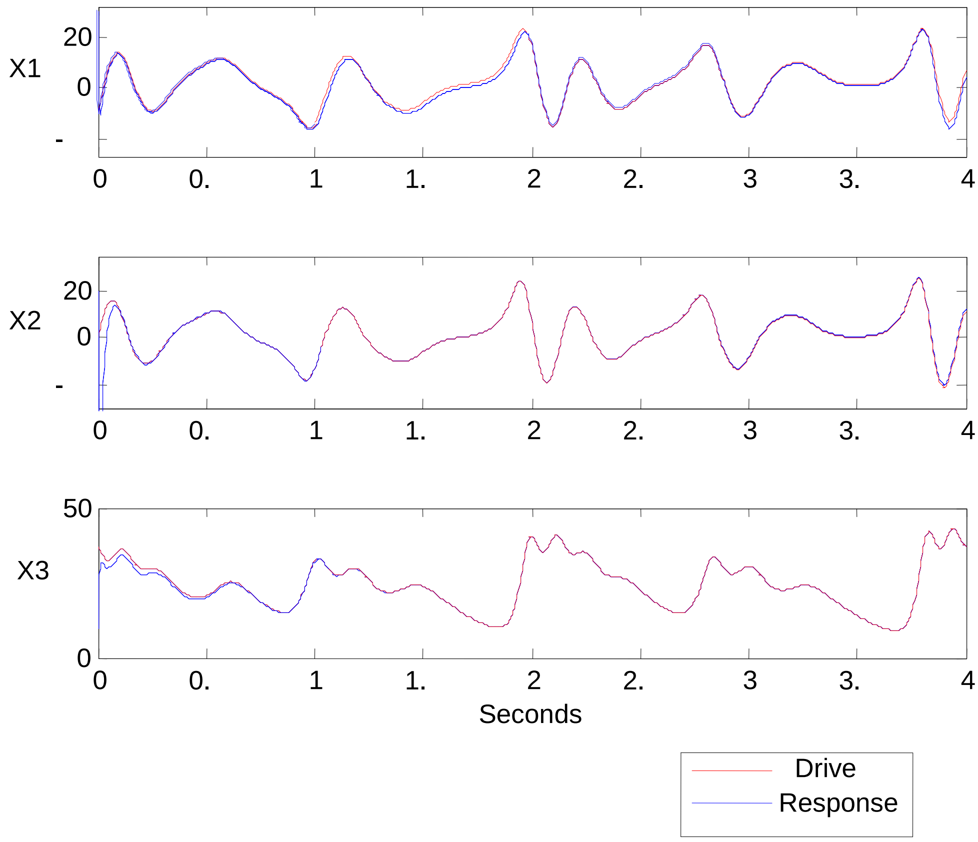


**Figure 4.** Nominal Chen circuit synchronization

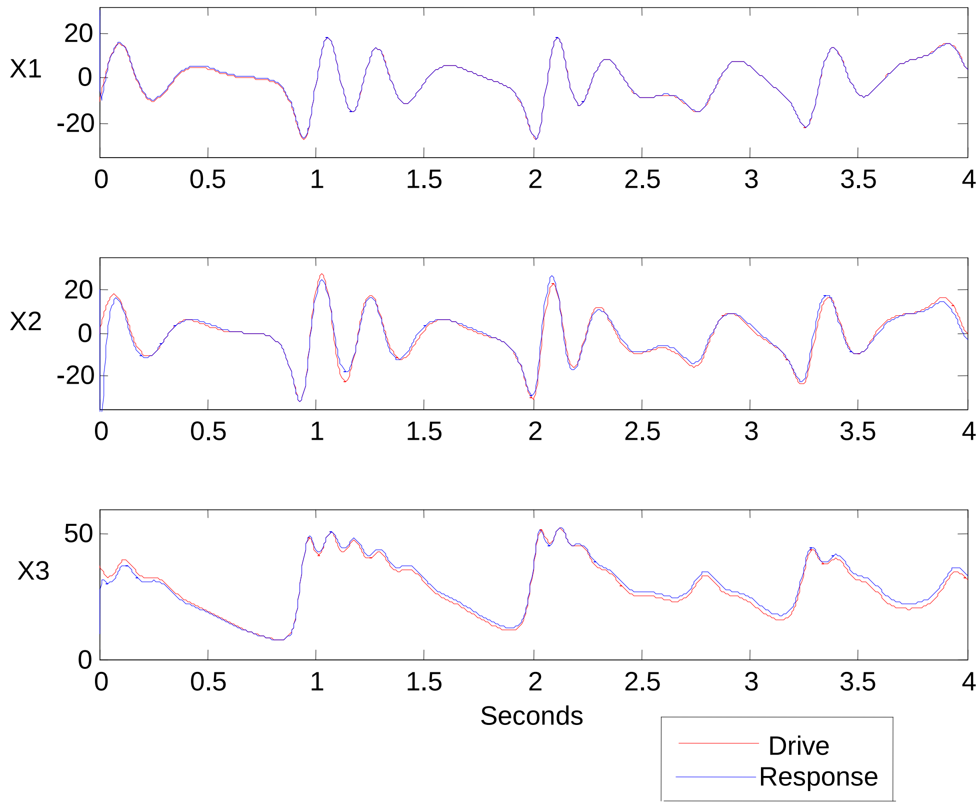


**Figure 5.** Chen system synchronization with $\zeta = 30\%$

**Table 3.** Chen system synchronization subjected to increasing parameter uncertainty

| Type | Nominal | 10% | 20% | 30% | 40% | 50% | 60% |
|---|---|---|---|---|---|---|---|
| Measure | 0.2759 | 0.4717 | 0.7152 | 1.0069 | 1.3231 | 1.5804 | 1.7853 |
| Normalized Measure | 0.0044 | 0.0075 | 0.0113 | 0.0159 | 0.0209 | 0.0250 | 0.0282 |
| Type | 70% | 80% | 90% | 100% | 120% | 120% | 170% |
| Measure | 2.2912 | 2.8243 | 3.1203 | 3.8673 | 6.9852 | 12.5255 | unstable |
| Normalized Measure | 0.0362 | 0.0447 | 0.0494 | 0.0612 | 0.1105 | 0.1982 | unstable |

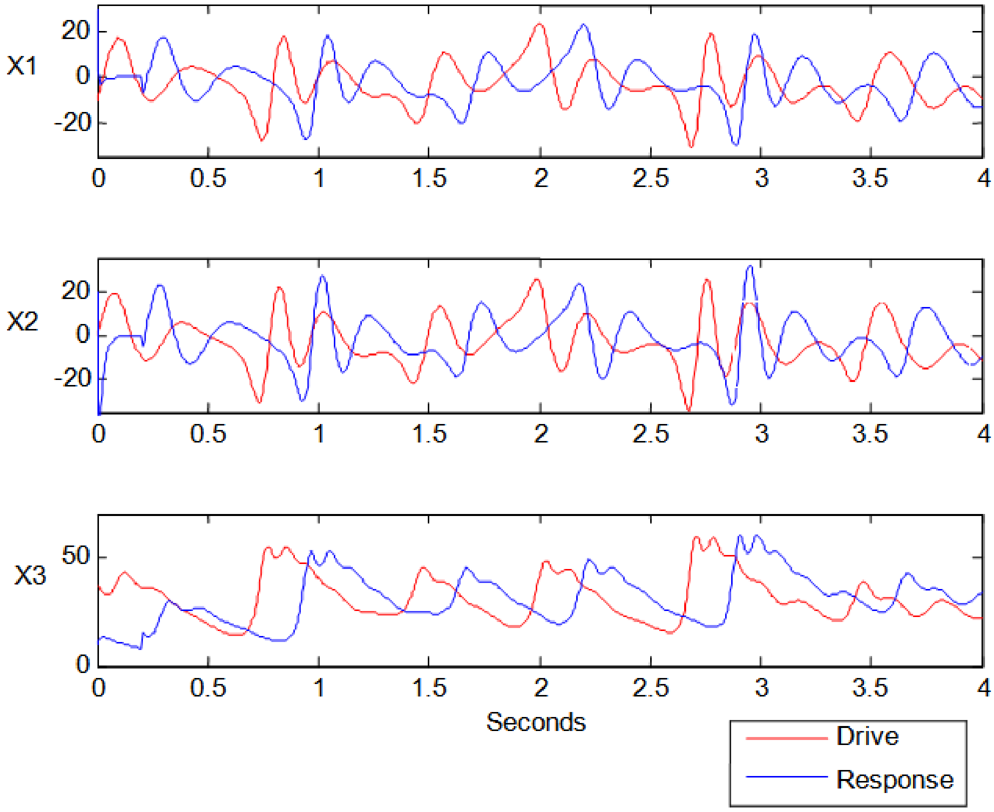


**Figure 6.** Chen system synchronization subjected to a 0.2 second state-delay

**Table 4.** Chen system synchronization subjected to increasing time delay

| Delay | Nominal | 0.025 sec | 0.050 sec | 0.075 sec | 0.1 sec | 0.2 sec | 0.3 sec |
|---|---|---|---|---|---|---|---|
| Measure | 0.2759 | 4.5415 | 7.5047 | 9.8771 | 11.6318 | 13.2562 | 13.8022 |
| Normalized Measure | 0.0044 | 0.0718 | 0.1187 | 0.1563 | 0.1840 | 0.2097 | 0.2184 |
| Delay | 0.4 sec | 0.5 sec | 0.6 sec | 0.7 sec | 0.8 sec | 0.9 sec | 1.0 sec |
| Measure | 14.0187 | 12.7388 | 11.9915 | 11.1585 | 12.6575 | 14.3675 | 14.1958 |
| Normalized Measure | 0.2218 | 0.2015 | 0.1897 | 0.1765 | 0.2003 | 0.2273 | 0.2246 |

## 6. Conclusions

A design of observer-based synchronization of chaotic system was developed in the present paper. It is based on state feedback LQR and duality property to solve the observer design. This synchronization is simple to design and proved to withstand significant parameter uncertainties and a state delay. A performance measure was introduced to demonstrate system performance under increasing parameter uncertainties and state delays. The effectiveness and feasibility of such a design were simulated in Matlab ® and discussed for two benchmark systems, the Chua circuit and the Chen system. A large number of cases for both increasing parameter uncertainties cases and increasing time-delayed cases was conducted, then the performance of these cases is recorded in the tables above to demonstrate the performance trends for such systems.

## References

[1] Y. J. Sun, "A novel chaos synchronization of uncertain mechanical systems with parameter mismatchings, external excitations, and chaotic vibrations". Communications in Nonlinear Science and Numerical Simulation, Vol. 17 (2012), Issue 2, 496-504.

[2] M.R. Faieghi, S.K. Mashhadi, D. Baleanu, "Sampled-data nonlinear observer design for chaos synchronization: A Lyapunov-based approach". Communications in Nonlinear Science and Numerical Simulation, Vol. 19 (2014), Issue 7, 2444-2453.

[3] Y. Chen, X. Wu, Z. Liu, "Global chaos synchronization of electro-mechanical gyrostat systems via variable substitution control". Chaos, Solitons & Fractals, Vol. 42 (2009), Issue 2, 1197-1205.

[4] M.P. Aghababa, H.P. Aghababa, “Synchronization of mechanical horizontal platform systems in finite time”. Applied Mathematical Modelling, Vol. 36 (2012), Issue 10, 4579-4591.

[5] S.S. Kim, H.H. Choi, "Adaptive synchronization method for chaotic permanent magnet synchronous motor". Mathematics and Computers in Simulation, Vol. 101 (2014), 31-42.

[6] A. Göksu, U. Kocamaz,Y. Uyaroğlu, "Synchronization and control of chaos in supply chain management". Computers & Industrial Engineering, In Press, Corrected Proof, Available online (2014).

[7] C. Zhan, J. Li, “Hybrid Function Projective Synchronization of Chaotic Systems with Uncertain Time-varying Parameters Fourier Series Expansion”. International Journal of Automation and Computing , Vol. 9 (2012), Issue 4, 388-394.

[8] X. Xiao, L. Zhou, Z. Zhang, “Synchronization of chaotic Lur’e systems with quantized sampled-data controller”. Communications in Nonlinear Science and Numerical Simulation, Vol. 19 (2014), Issue 6, 2039-2047.

[9] M. Ababneh, I. Etier, M. Smadi and J. Ghaeb, " Synchronization of Chaos Systems Using Fuzzy Logic," Journal of Computer Science, vol. 7 (2011), pp. 197-205.

[10] L. Chrif, Z. Kadda, "Aircraft Control System Using LQG and LQR Controller with Optimal Estimation-Kalman Filter Design", Procedia Engineering, Vol. 80 (2014), 245-257.

[11] S. Schulz, H. Gomes, A. Awruch, "Optimal discrete piezoelectric patch allocation on composite structures for vibration control based on GA and modal LQR". Computers & Structures, Vol. 128 (2013), 101-115.

[12] A. Senouci, A. Boukabou, “Predictive control and synchronization of chaotic and hyperchaotic systems based on a T–S fuzzy model” Mathematics and Computers in Simulation, Vol. 105 (2014), 62-78.

[13] M. Ababneh, M. Salah, K. Al-Widyan, " Linearization of nonlinear dynamical system: A comparative study ". Jordan Journal of Mechanical and Industrial Engineering, Vol. 5 (2011), 567 - 571.

[14] Z. Ulukök, R. Türkmen, "Improved upper bounds for the solution of the continuous algebraic Riccati matrix equation". Applied Mathematics and Computation, Vol. 225, (2013), 306-317.

[15] Ostertag E, Mono and Multivariable Control and Estimation: Linear, Quadratic and LMI Methods. 2011 edition. Berlin: Springer; 2011.

[16] E. Ponce, J. Ros, E. Vela, "Unfolding the fold-Hopf bifurcation in piecewise linear continuous differential systems with symmetry". Physica D: Nonlinear Phenomena, Vol. 250 (2013Y, 34-46.

[17] S. Das, A. Acharya, I. Pan, "Simulation studies on the design of optimum PID controllers to suppress chaotic oscillations in a family of Lorenz-like multi-wing attractors". Mathematics and Computers in Simulation, Vol. 100 (2014), 72-87.

JJMIE

Volume 9 Number 2, April.2015
ISSN 1995-6665
Pages 85 - 102

Jordan Journal of Mechanical and Industrial Engineering

# Hybrid DEBBO Algorithm for Tuning the Parameters of PID Controller Applied to Vehicle Active Suspension System

Kalaivani Rajagopal * [a], Lakshmi Ponnusamy[b]

[a]Research Scholar, DEEE, CEG, Anna University, Chennai, India
[b] Professor, DEEE, CEG, Anna University, Chennai, India

Received 6 Nov 2014 Accepted 9 May 2015

**Abstract**

This paper highlights the use of hybridizing Biogeography-Based Optimization (BBO) with Differential Evolution (DE) algorithm for parameter tuning of Proportional Integral Derivative (PID) controller applied to Vehicle Active Suspension System (VASS). Initially BBO, an escalating nature enthused global optimization procedure based on the study of the ecological distribution of biological organisms, and the hybridized DEBBO algorithm which inherits the behaviours of BBO and DE, were used to find the tuning parameters of the PID controller to improve the performance of VASS. Simulations of passive system, active system, having PID controller with and without optimizations, were performed by considering trapezoidal, step and a random kind of road disturbances in MATLAB/SIMULINK environment. The simulation results point out an improvement in the results with the DEBBO algorithm which converges faster than BBO..



**Keywords:** *Vehicle Active Suspension, Biogeography-Based Optimization (BBO), Differential Evolution (DE), DEBBO, Simulation*.

## 1. Introduction

The vibration of the vehicle body can cause an unwanted noise in the vehicle, a damage to the fittings attached to the car and severe health problems, such as an increase in the heart rate, spinal problems, etc. to the passengers. Research and the development sections of automobile industries hence promote research on vibration control. For vehicle handling and ride comfort, the suspension system of an automobile plays an essential role. Vehicle handling depends on the force acting between the road surface and the wheels. The ride comfort is related to vehicle motion sensed by the passenger. To improve vehicle handling and the ride comfort performance, in preference to conventional passive system, semi-active and active systems are being developed. The passive system uses a static spring and a damper where as a semi-active suspension involves the use of dampers with variable gain. On the other hand, an active suspension involves the passive components augmented by actuators that supply additional forces and possesses the ability to reduce the acceleration of sprung mass continuously as well as to minimize the suspension deflection which results in the improvement of the tyre grip with the road surface [1; 2].

Research on the control strategies of Vehicle Active Suspension System (*VASS*) has been concentrated on by academicians as well since this problem is open to all. In the past, many researchers explored several control approaches hypothetically, simulated them with simulation software, confirmed practically and proposed for the control of active suspension system. The survey of optimal control technique applications to the design of active suspensions are listed in [3] and the emphasis is on Linear-Quadratic (*LQ*) optimal control. A method for designing a controller with a model which includes the passenger dynamics is presented in [4]. The comparison of Linear Matrix Inequality (*LMI*) based controller and optimal Proportional Integral Derivative (*PID*) controller by Abdalla *et al.* [5] proved the sprung mass displacement response improvement by *LMI* controller with only the suspension stroke as the feedback.

*PID* controller design is discussed in [5-7]. The design of robust *PI* controller which is used to obtain an optimal control is discussed in [8]. The conclusion, made by Dan Simon [9], stimulated the idea of using Biogeography-Based Optimization (*BBO*) for the optimization of *PID* parameters.

In [10] the classification of the satellite image of a particular land cover using the theory of *BBO* is highlighted, concluding that with this, highly accurate land cover features can be extracted effectively. To optimize the element length and spacing for Yagi-Uda antenna, *BBO* is used and the performance is evaluated with a method of moment's code NEC2 [11]. *BBO* algorithm, to solve both convex and non-convex Economic Load Dispatch (*ELD*) problems of thermal plants, is proposed and suggested as a

* Corresponding author. e-mail: kalaivanisudhagar@gmail.com.

 

promising alternative approach for solving the *ELD* problems in practical power system [12]. Markov theory for partial immigration based *BBO* [13] is used to derive a dynamic system model. A better insight into the dynamics of migration in actual biogeography systems is given [14]; it also helped in understanding the search mechanism of *BBO* on multimodal fitness landscapes. In [15], a multi-objective *BBO* algorithm is proposed to design optimal placement of phasor measurement units, which makes the power system network completely observable and the simultaneous optimization of the two conflicting objectives, such as minimization and maximization of two different parameters, are performed. The effectiveness of *BBO* over Genetic Algorithm (*GA*) and Particle Swam Optimization (*PSO*) is highlighted [16] for an *ELD* problem. The performance of *BBO* is tested for real-world optimization problems with some benchmark functions [17]. An improved accuracy yielding algorithm is presented [18], in which the performance of *BBO* is accelerated with the help of a modified mutation and clear duplicate operators; the suitability of *BBO* for real time applications is also discussed. A combination of Differential Evolution (*DE*) and *BBO* is designed to accelerate the convergence speed of the algorithm and of improving the solution for the economic emission load dispatch problem [19].

In the present paper, the preference is to optimize the *PID* controller tuning parameters with hybridized *DEBBO* to improve the rapidity of convergence. The likelihood of the proposed method was verified in terms of the computational efficiency and the outputs of the linear *VASS* models which are considered for the simulation study in comparison with *BBO*.

The present study is organized as follows: Quarter Car (*QC*) model and Half Car (*HC*) model dynamics of an active suspension system are briefly explained in section 2. Discussion of the control scheme is presented in section 3. In section 4, the simulation results are presented and discussed. The final section presents the conclusion of the study.

## 2. Active Suspension System

The passive suspension system has the ability to only store and dissipate energy. Its parameters, such as spring stiffness and damping coefficients, are fixed in order to achieve a certain level of compromise between road holding, load carrying and comfort. The semi active suspension system involves a variable damper, while the active suspension system has the ability to store, dissipate and introduce energy to the system; it may vary its parameters depending on the working conditions.

### *2.1. Quarter Car Model*

A two-Degree of Freedom (*DOF*) *QC* model of *VASS* is shown in Figure 1. It represents the automotive system at each wheel, i.e., the motion of the axle and the vehicle body at any one of the four wheels of the vehicle. The *QC* model, used in [20], is considered because it is simple and one can observe the basic features of the *VASS* such as sprung mass displacement, body acceleration, suspension deflection and tyre deflection. The suspension model consists of a spring $k_s$, a damper $c_s$ and an actuator of active force $F_a$. For a passive suspension, $F_a$ can be set to zero. The sprung mass $m_s$ represents the *QC* equivalent of the vehicle body mass. An unsprung mass $m_u$ represents the equivalent mass due to axle and tyre. The vertical stiffness of the tyre is represented by the spring $k_t$. The variables $y_s$, $y_u$ and $y_t$ represents the vertical displacements from static equilibrium of sprung mass, unsprung mass and the road, respectively. Equations of motion of the two *DOF* *QC* model of *VASS* are given in (1). It is assumed that the suspension spring stiffness and tyre stiffness are linear in their operating ranges and that the tyre does not leave the ground. The state space representation (2) of *QC* model is given below:

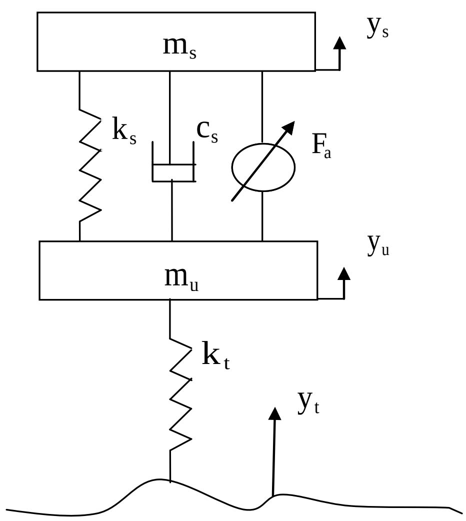


**Figure 1.** Quarter Car model

$$m_s \ddot{y}_s + c_s(\dot{y}_s - \dot{y}_u) + k_s(y_s - y_u) = F_a \quad (1)$$

### *2.2. Half Car Model*

An *HC* active suspension model with 4 *DOF* [21], which represents the combination of two *QC* models, i.e., one front wheel, one rear wheel and the associated axle parts of a car (Figure 2), was taken. It includes sprung mass $m_s$, front unsprung mass $m_{uf}$, rear unsprung mass $m_{ur}$, front suspension damping coefficient $c_{sf}$, rear suspension damping coefficient $c_{sr}$, front suspension stiffness $k_{sf}$, rear suspension stiffness $k_{sr}$, front tyre damping coefficient $c_{tf}$, rear tyre damping coefficient $c_{tr}$, front tyre stiffness $k_{tf}$, rear tyre stiffness $k_{tr}$, pitch moment of inertia $I_p$, distance of front axle to sprung mass Center of Gravity (*CG*) $L_f$, distance of rear axle to sprung mass *CG* $L_r$, front actuator force $F_{af}$ and the rear actuator force $F_{ar}$. $y_s, \theta$ are the vertical displacement and the pitch angle of the sprung mass at the *CG*, $y_{sf}, y_{sr}$ are the vertical displacement of front and rear suspensions, $y_{uf}, y_{ur}$ are the unsprung mass displacements and $y_{tf}, y_{tr}$ are the tyre displacements at the front and rear. It is assumed that the *HC* model system is linear, the tires always have contact with the road and the forces due to moment and backlash in various joints, linkages and gear are neglected.

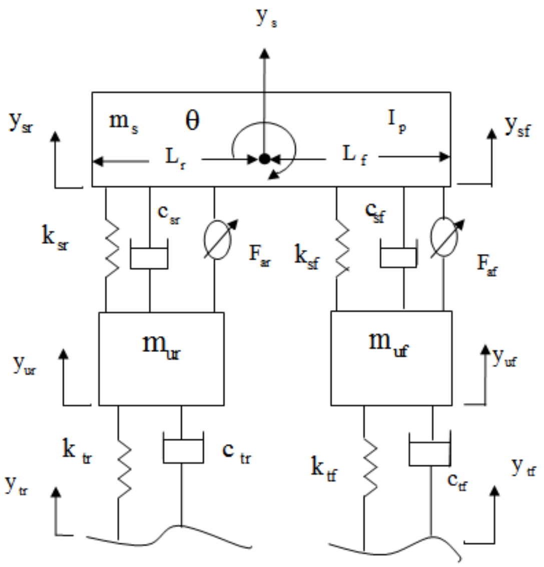


**Figure 2.** Half Car model

$$m_u\ddot{y}_u - c_s(\dot{y}_s - \dot{y}_u) - k_s(y_s - y_u) - k_t(y_t - y_u) = -F_a \tag{2}$$

$$\ddot{y}_{ur} = \frac{[-k_{tr}(y_{ur} - y_{tr}) - c_{sr}(\dot{y}_{ur} - \dot{y}_{sr}) - k_{sr}(y_{ur} - y_{sr}) - c_{tr}(\dot{y}_{ur} - \dot{y}_{tr}) - F_{ar}]}{m_{ur}} \tag{3}$$

$$\ddot{y}_{uf} = \frac{[-k_{tf}(y_{uf} - y_{tf}) - c_{sf}(\dot{y}_{uf} - \dot{y}_{sf}) - k_{sf}(y_{uf} - y_{sf}) - c_{tf}(\dot{y}_{uf} - \dot{y}_{tf}) - F_{af}]}{m_{uf}} \tag{4}$$

$$\ddot{y}_s = \frac{-[k_{sr}(y_{sr} - y_{ur}) + k_{sf}(y_{sf} - y_{uf}) + c_{sr}(\dot{y}_{sr} - \dot{y}_{ur}) + c_{sf}(\dot{y}_{sf} - \dot{y}_{uf}) - F_{ar} - F_{af}]}{m_s} \tag{5}$$

$$\ddot{\theta} = \frac{-L_r[(c_{sr}(\dot{y}_{sr} - \dot{y}_{ur}) + k_{sr}(y_{sr} - y_{ur})] + L_f[k_{sf}(y_{sf} - y_{uf}) + c_{sf}(\dot{y}_{sf} - \dot{y}_{uf})] - L_fF_{af} + L_rF_{ar}}{I_s} \tag{6}$$

$$y_{sr} = y_s - L_r\theta \tag{7}$$

$$y_{sf} = y_s + L_f\theta \tag{8}$$

For the passive suspension system, the control forces in the front and rear $F_{af}$ and $F_{ar}$ are equal to 0.

## 3. Controller Design

### *3.1. PID Controller*

Most of the automated industrial processes include a *PID* controller which is a combination of proportional, integral and derivative controller that can improve both the transient and the steady state performance of the system. The mathematical representation of the simple *PID* control scheme is given by:

$$G_C = k_p e(t) + k_i \int e(t)dt + k_d \frac{de}{dt} \tag{9}$$

where $G_C$ is the controller output

$k_p$ proportional gain

$k_i$ integral gain

$k_d$ differential gain

$e(t)$ input to the controller

$\int e(t)dt$ time integral of the input signal

$\frac{de}{dt}$ time derivative of the input signal

To reduce the effect of the road disturbance input (Figure 3), two suspension parameters, suspension deflection ( $y_s - y_u$ ) and velocity, are feedback to the controllers [20]. The feedback gains are $G_e$ and $G_V$, respectively. The output control signals are amplified by a gain $G_U$ and, then, given as the input to the actuator. In the present work, the nonlinear dynamics of actuator are not considered and the gain of the linear actuator is taken as $G_a$. The actuator force $F_a$, which is the additional input to the system, is proportional to the controller output to have better comfort. An autotuning for both $PID_1$ and $PID_2$ was carried out using a robust response tuning metod with the MATLAB simulation software.

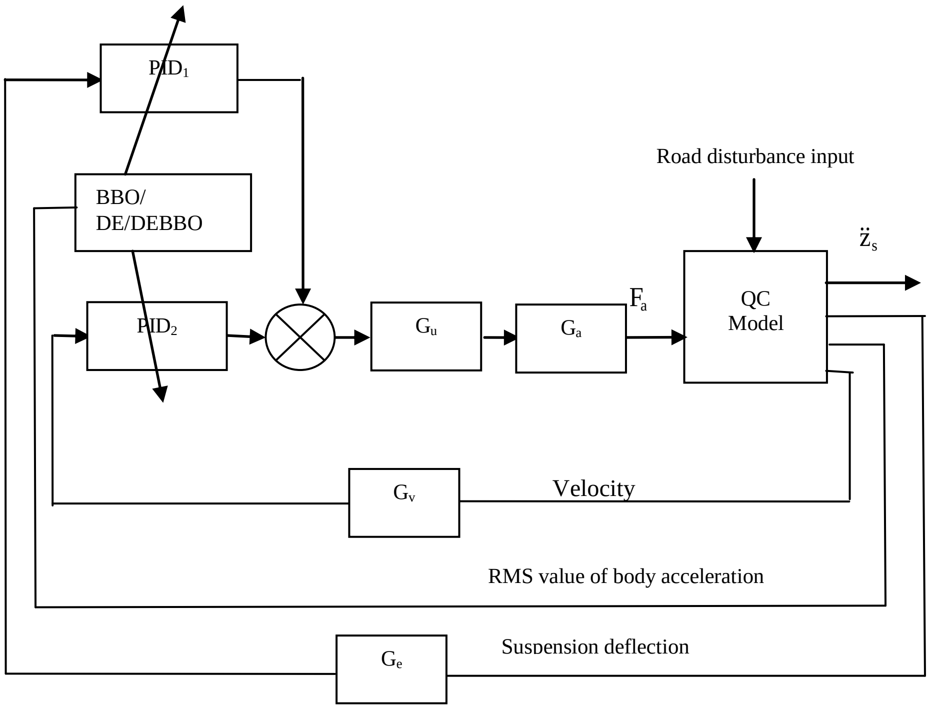


**Figure 3.** The block diagram representation of control scheme of VASS using PID controller

*3.2. Optimization of PID Controller*

In the present work, *BBO*, *DE* and *DEBBO* techniques are used to find the *PID* tuning parameters, such as $k_p$, $k_i$ and $k_d$, of both the controllers $PID_1$ and $PID_2$ (Figure 3) to give an optimum [22] *RMS* value of body acceleration. To optimize the continuous time body acceleration signal (*f(t)*) energy, the cumulative *RMS* value is taken; it is given as follows:

$$J = \sqrt{\frac{1}{T}\int_0^T \|f(t)\|^2 \, dt} \quad (10)$$

where *T* is the vibration period in seconds.

*3.2.1. Biogeography Based Optimization Based PID Controller*

A population based *BBO* technique was developed based on the theory of Biogeography [9] which describes how species voyage from one habitat to another, how new species come up and species become vanished. A habitat is a geographically isolated island from other habitats. Each habitat has its individual features which are specified by the Habitat Suitability Index (*HSI*) variables. A habitat with high *HSI* is well suited for species living. The migration of a species among habitats takes place when the high *HSI* habitats have more species or when a habitat has low *HSI*. This process is known as emigration. Another process called immigration and takes place when the species move towards the habitat with high *HSI* having few species. The emigration and immigration of species from a habitat are called migration. The emigration rate ($\mu$) and immigration rate ($\lambda$) vary with the number of species available in the habitat. With no species, the immigration rate touches the upper limit and with the maximum number of species, it is zero, whereas the emigration rate increases with the increase in the number of species. The change in *HSI* due to a natural disaster is taken into account with the mutation operation.

The optimization steps of *BBO* algorithm [15] are described as follows:

1. Initialize the optimization problem, the *BBO* parameters and the habitats.
2. Perform *BBO* operations such as migration and mutation.
3. Modify the habitats.
4. Check the stopping criteria; if not achieved, repeat from step 2.

*BBO* does not involve the reproduction of a solution as in *GA*. In each generation, the fitness of every solution (habitat) is used to find the migration rates.

For the *BBO* based *PID* (*BBOPID*) controller [23], the following parameters are initialized: population size, the maximum species count ($S_{max}$), maximum emigration rate ($E$), maximum immigration rate ($I$), maximum mutation rate ($m_{max}$), habitat modification probability ($P_{mod}$), number of decision variables, the number of habitats, maximum number of generations, mutation probability, and migration probability.

1. The individual habitat variables are random initialized.
2. Mapping of *HSI* to the number of species S, calculation of the emigration rate and immigration rate using equations 11 and 12 are performed.

$$\lambda = I(1 - \frac{d}{S_{max}}) \tag{11}$$

$$\mu = \frac{E \times d}{S_{max}} \tag{12}$$

where $d$ is the number of species at the instant of time.

3. The BBO operation migration is performed based on the definition 7 in [9] and the HSI is recomputed.
4. Then the mutation operation is performed as in definition 8 in [9] and the HSI is recomputed. The emigration and immigration rates of each solution are useful in probabilistically sharing the information between the habitats. Each solution can be modified with the habitat modification probability Pmod to yield good solution.
5. From step 2 the computation is repeated for the next iteration. The loop is terminated after predefined number of generations or after achievement of acceptable solution.

Parameter Initialization for *BBO*

| | | |
|---|---|---|
| Modification probability | | = 1 |
| Mutation probability | | = 0.05 |
| Selectiveness parameter | δ | = 2 |
| Max immigration rate | | = 1 |
| Max emigration rate | | = 1 |
| Step size used for numerical integration | | = 1 |
| Lower bound and Upper bound for immigration probability per gene | | = [0.01, 1] |

*3.2.2. Differential Evolution Based PID Controller*

Technically, a simple population-based Differential Evolution (*DE*) algorithm [24, 25] having a self-organizing ability, is suitable even for non-linear systems and can be used for a continuous function optimization for tuning of *PID* controller parameters. Basic steps involved in *DE* algorithm are:

1. Initialization
2. Evaluation
3. Repeat

{ Mutation
Recombination
Evaluation
Selection }
Until fitness function is minimized.

Generate the mutant vector $v_{i,G+1}$ (13) for each target vector $x_{i,G}$, $i=1,2,3\ldots\ldots N$ where $N$ is the number of parameter vectors in the population.

$$v_{i,G+1} = x_{r1,G} + F.(x_{r2,G} - x_{r3,G}) \qquad r_1, r_2, r_3 \in \{1,2,\ldots\ldots N\} \tag{13}$$

The real and constant scaling factor for differential variation $F \in [0,2]$

The trial vector for crossover operation is $u_{i,G+1} = (u_{1i,G+1}, u_{2i,G+1} \ldots\ldots u_{Di,G+1})$ (14)

where

$$u_{ji,G+1} = v_{ji,G+1} \quad if(randb(j) \le CR) or j = rnbr(i)$$
$$x_{ji,G} \quad if(randb(j) > CR) and j \ne rnbr(i) \tag{15}$$
$$j = 1,2,\ldots\ldots D$$

where

$CR \in [0,1]$ is the crossover constant

$randb(j) \in [0,1]$ is the j[th] evaluation of uniform random number

$rnbr(i) \in 1,2,\ldots\ldots D$ randomly chosen index which ensures that $u_{i,G+1}$ gets at least one parameter from $v_{i,G+1}$.

The fitness criterion is used to decide whether the trial vector is a member of next generation. If the fitness value of the trial vector $u_{i,G+1}$ is better than that of target vector $x_{i,G}$, then, in next generation, the target vector $x_{i,G+1}$ is assigned to be $u_{i,G+1}$. Otherwise first generation value $x_{i,G}$ is retained.

Parameter Initialization for *DE*

| | |
|---|---|
| Scaling factor | $F$ = 0.5 |
| Crossover constant | $CR$ = 0.5 |

*3.2.3. Hybridization*

The *BBO* algorithm, without hybridizing with any evolutionary algorithms, does not have much diversity in local or sub optimal solutions. In *DEBBO*, a hybrid migration operator of *BBO* is applied along with mutation, crossover and selection operators of *DE* which combines the searching of *DE* with the operation of *BBO* effectively to speed up the convergence property [26, 27] and to find better quality results.

Parameters for *DEBBO* are initialized as in *BBO* and *DE*.

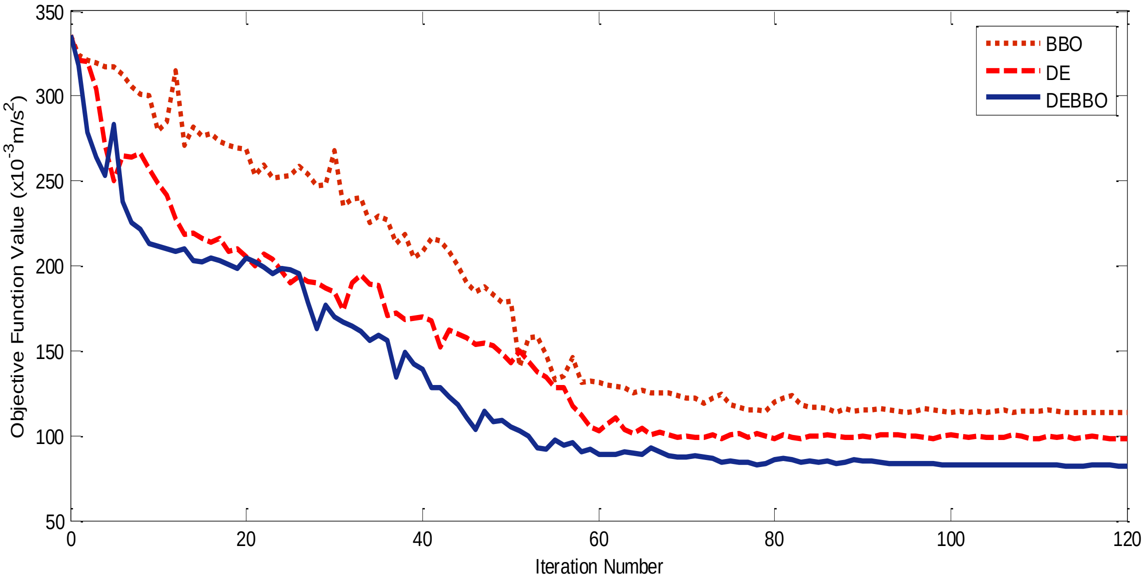


**Figure 4.** Statistics of search process

The optimization results were computed by averaging 20 minimization runs and the convergence characteristics of each technique are shown in Figure 4. As the convergence rate is fast in the case of *DEBBO*, the corrective actions can be taken quickly compared to the *BBO* without hybridization for a *VASS*. *DEBBO* yields sub linear convergence. Each run yielded the global minimum results. From the convergence plot, *DEBBO* is found to be superior to the *BBO* algorithm.

## 4. Simulation

The parameters of the *QC* model, taken from [20], are listed below:

| | | |
|---|---|---|
| Sprung mass | ( $m_s$ ) | : 290 kg |
| Unsprung mass | ( $m_u$ ) | : 59 kg |
| Damper coefficient | ( $c_s$ ) | : 1,000 Ns/m |
| Suspension stiffness | ( $k_s$ ) | : 16,812 N/m |
| Tyre stiffness | ( $k_t$ ) | : 190,000 N/m |

The parameters of the *HC* model, taken from [21], are listed below:

| | | |
|---|---|---|
| Sprung mass | ($m_s$) | : 430 kg |
| Pitch moment of inertia | ($I_p$) | : 600 kgm$^2$ |
| Front unsprung mass | ($m_{uf}$) | : 30 kg |
| Rear unsprung mass | ($m_{ur}$) | : 25 kg |
| Front suspension damping coefficient | ($c_{sf}$) | : 500Ns/m |
| Rear suspension damping coefficient | ($c_{sr}$) | : 400Ns/m |
| Front tyre damping coefficient | ($c_{tf}$) | : 24Ns/m |
| Rear tyre damping coefficient | ($c_{tr}$) | : 24Ns/m |
| Front suspension stiffness | ($k_{sf}$) | : 6666.67N/m |
| Rear suspension stiffness | ($k_{sr}$) | : 10000N/m |
| Front tyre stiffness | ($k_{tf}$) | : 152N/m |
| Rear tyre stiffness | ($k_{tr}$) | : 152N/m |
| Distance of front axle to sprung mass *CG* | ($L_f$) | : 0.871m |
| Distance of rear axle to sprung mass *CG* | ($L_r$) | : 1.469m |

International Organization for Standardization gives the classification of road roughness using Power Spectral Density (*PSD*) values. The present study considered, initially, a trapezoidal road disturbance which represents the reflector paved on the road, secondly, a step input which represents a vehicle coming out of a pothole and, thirdly, a random input. For the *HC* model, front road input $y_{tf}$ and a 0.84 sec time delayed rear road input $y_{tr}$ are considered and are shown in Figure 5.

The mathematical model of the vehicle suspension systems *QC* and *HC* is detailed in section 2 with the controllers discussed in sections 3, in which all are simulated with three road input profiles discussed.

The *PID* tuning parameters obtained with a robust response tuning, *BBO*, *DE* and *DEBBO* with trapezoidal input are listed in Table 1. For the suitability of the designed controller for other kinds of road disturbances, the simulation is carried out with step and random type of road inputs.

Table 1. The Optimized PID tuning parameters with BBO, DE and DEBBO

| **PID Para-meter** | **Controller** | | | |
|---|---|---|---|---|
| | **PID** | **BBOPID** | **DEPID** | **DEBBOPID** |
| $kp_1$ | 0.0106 | 0.0432 | 0.3810 | 0.0350 |
| $ki_1$ | 0.4159 | 0.1934 | 0.2863 | 0.4076 |
| $kd_1$ | 0.0022 | 0.0050 | 0.1182 | 0.0122 |
| $kp_2$ | 0.3801 | 0.8739 | 2.3007 | 1.7680 |
| $ki_2$ | 0.5632 | 0.2846 | 0.5685 | 0.2289 |
| $kd_2$ | 0.0044 | 0.0383 | 0.0242 | 0.0326 |

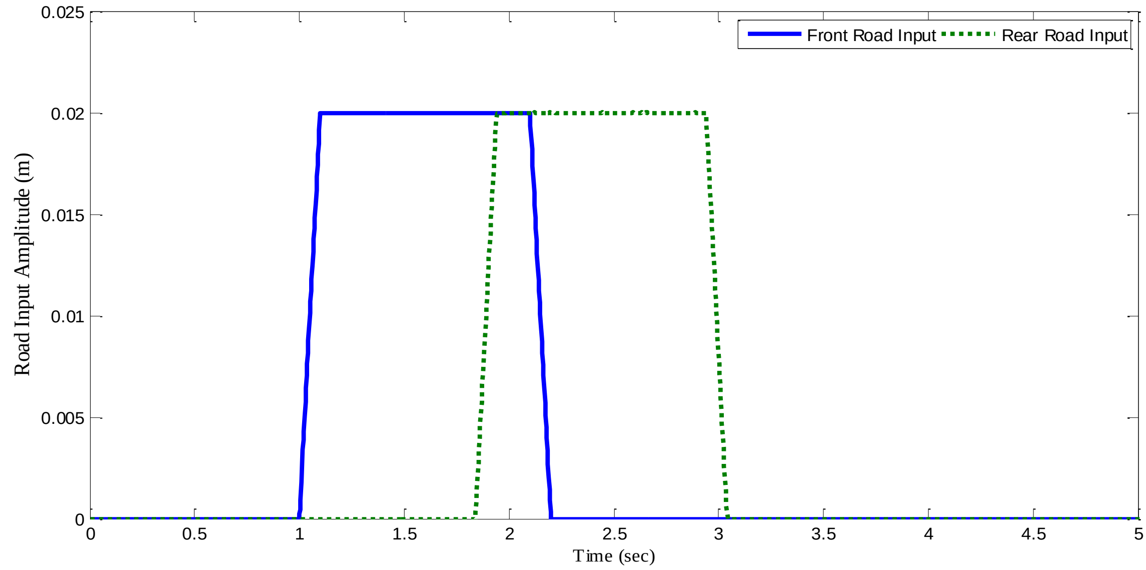


(a)

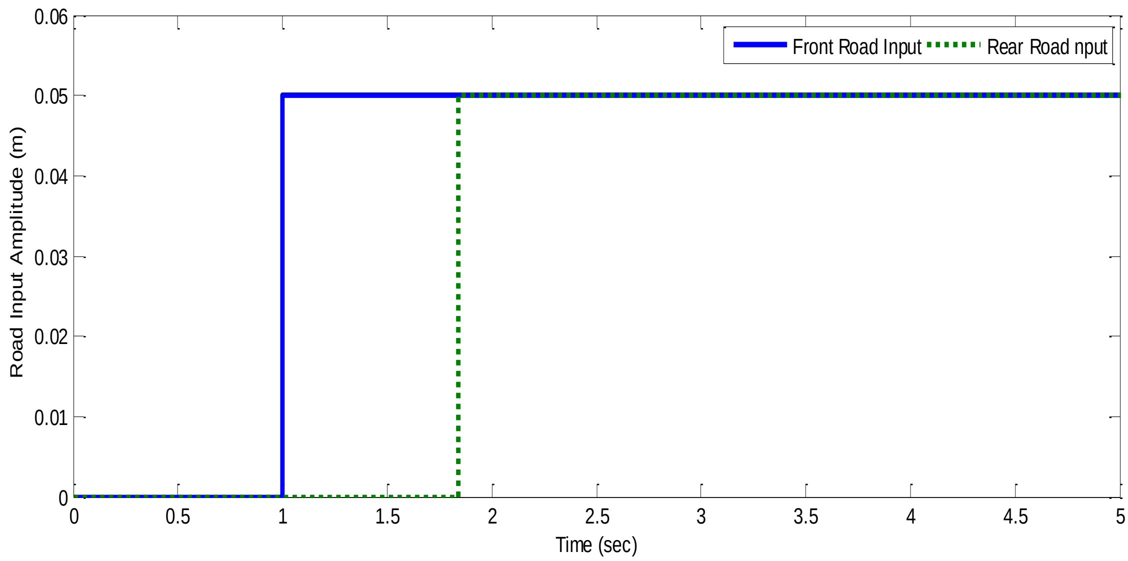


(b)

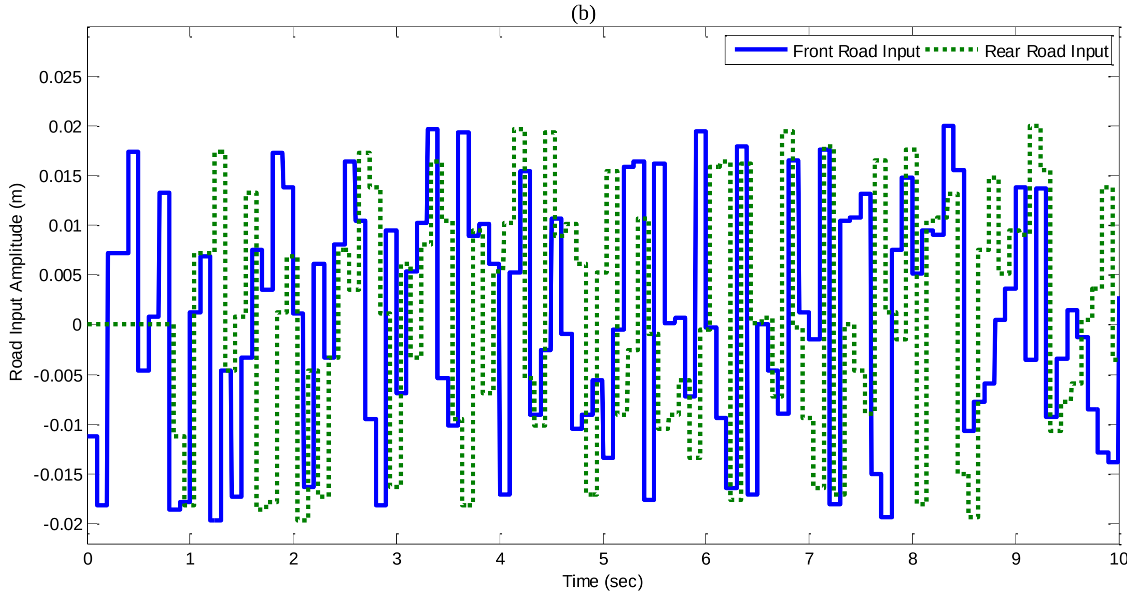


(c )

**Figure 5.** Road Input profile : (a) Trapezoidal Input (b) Step Input (c ) Random Input

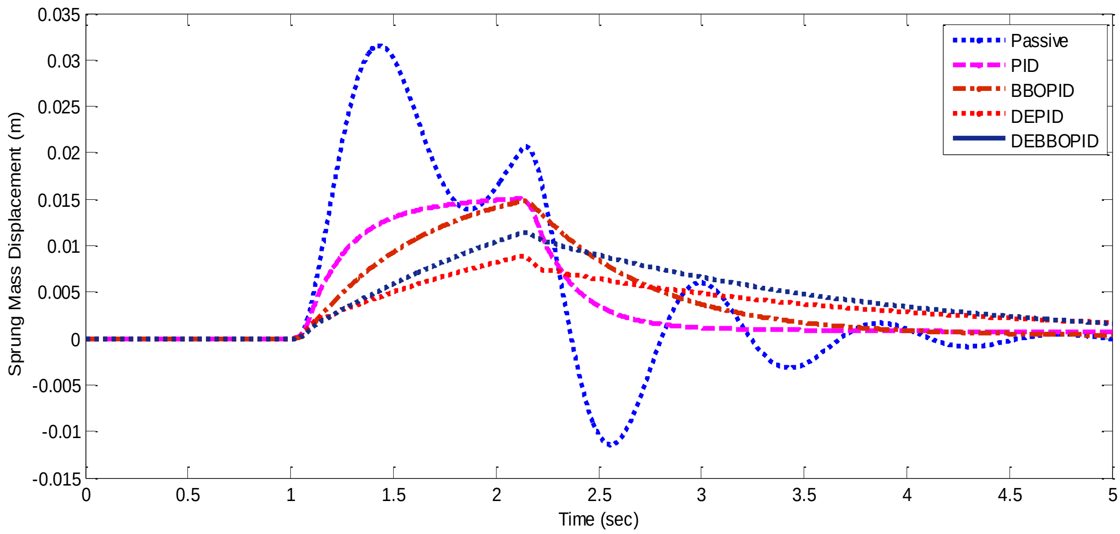
Sprung Mass Displacement (m)
Time (sec)
Passive
PID
BBOPID
DEPID
DEBBOPID
(a)

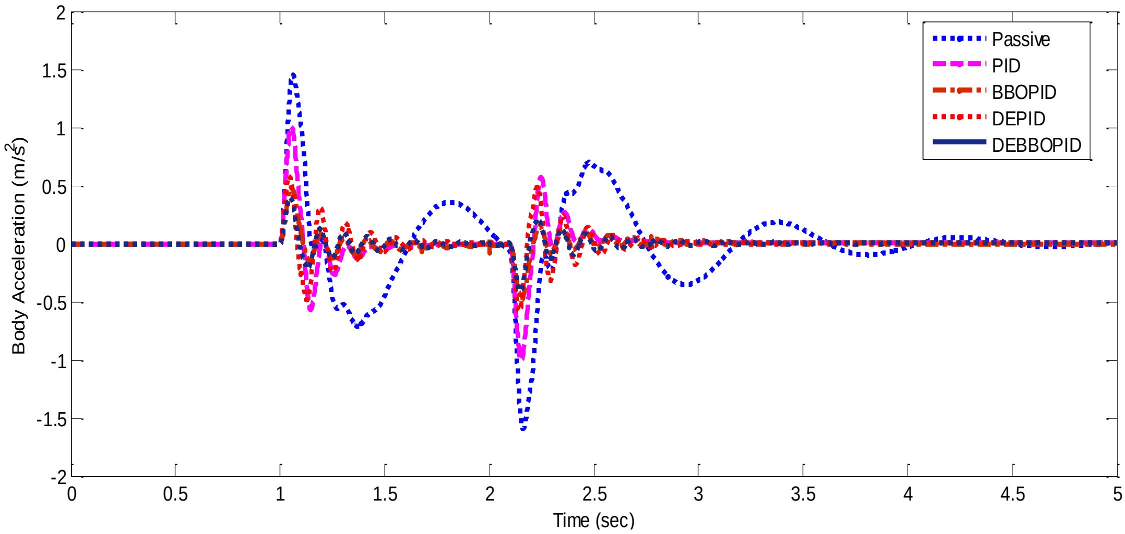
Body Acceleration (m/s2)
Time (sec)
Passive
PID
BBOPID
DEPID
DEBBOPID
(b)

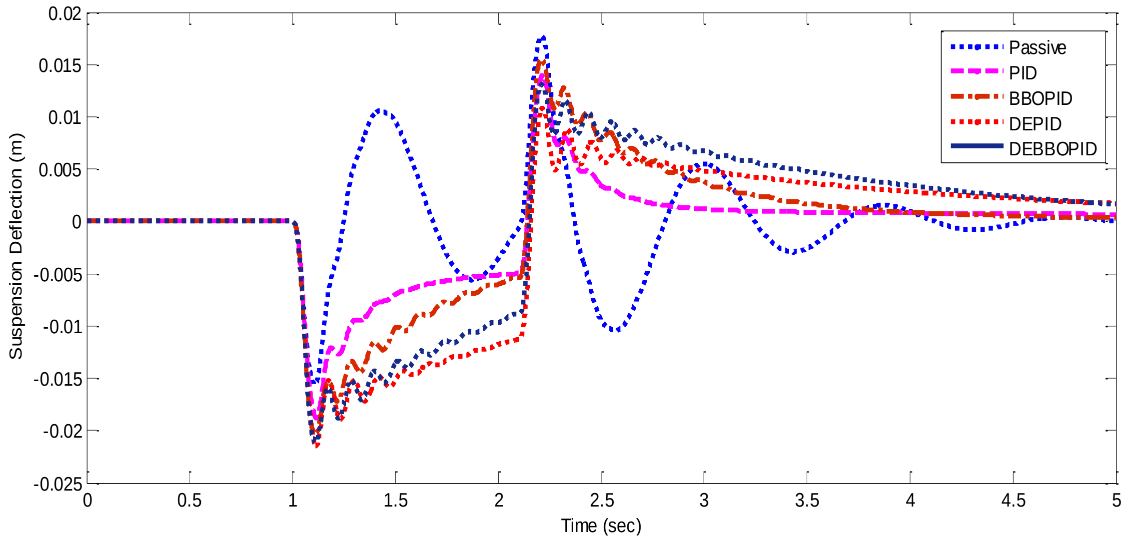
Suspension Deflection (m)
Time (sec)
Passive
PID
BBOPID
DEPID
DEBBOPID
(c)

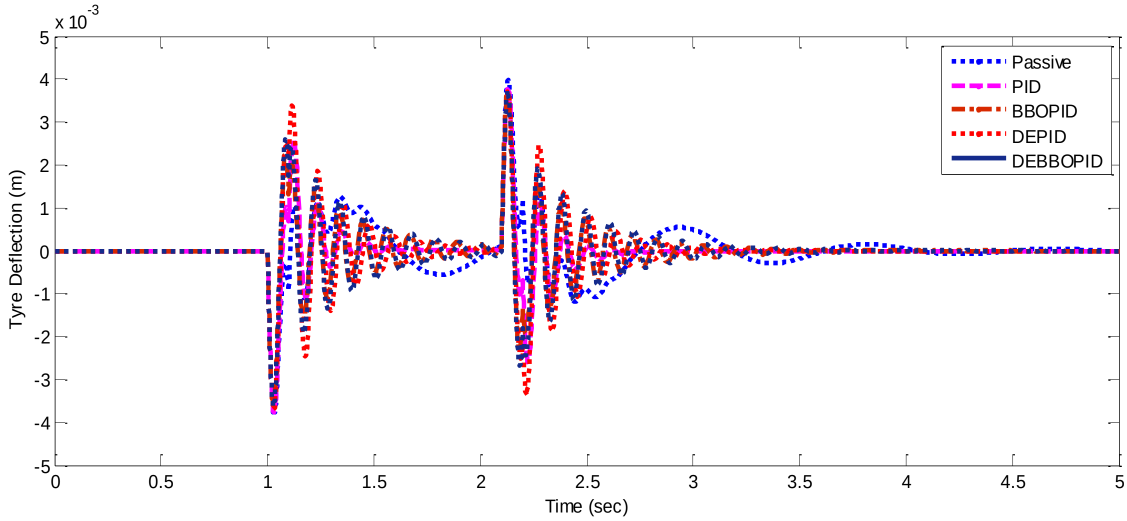


(d)

**Figure 6.** Time responses of quarter car model with trapezoidal input : (a) Sprung Mass Displacement (b) Body Acceleration (c)Suspension Deflection (d) Tyre Deflection

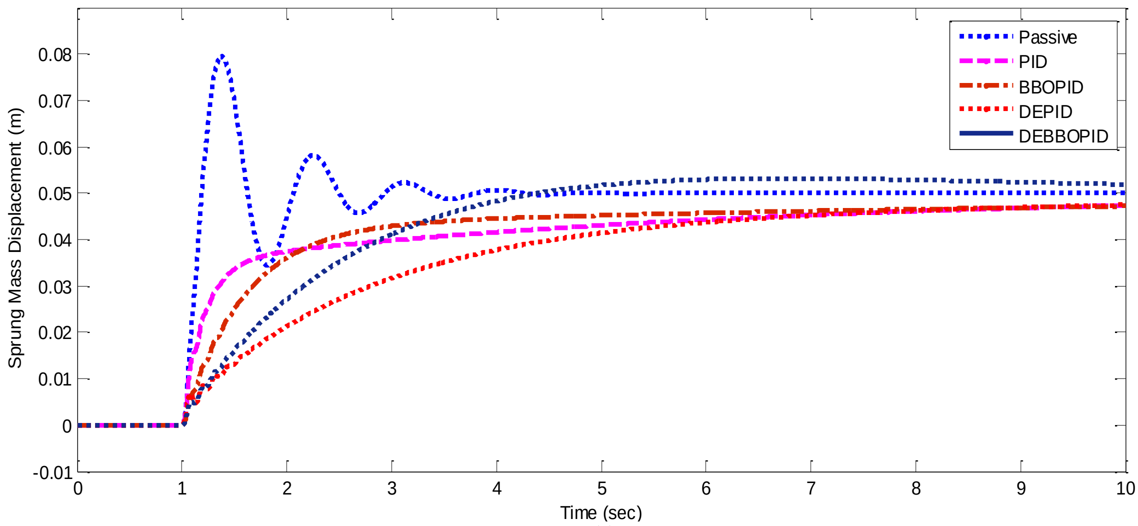


(a)

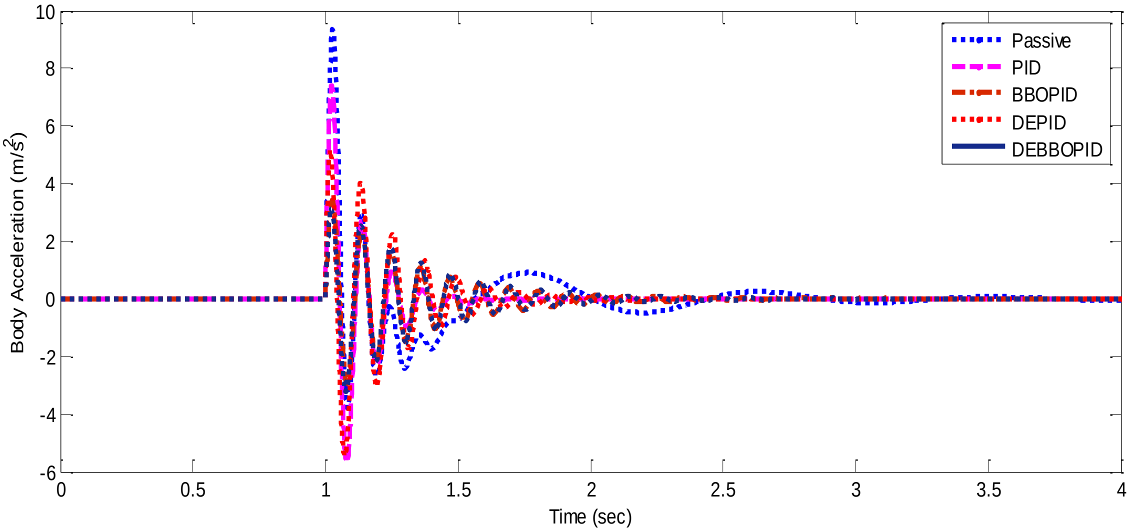


(b)

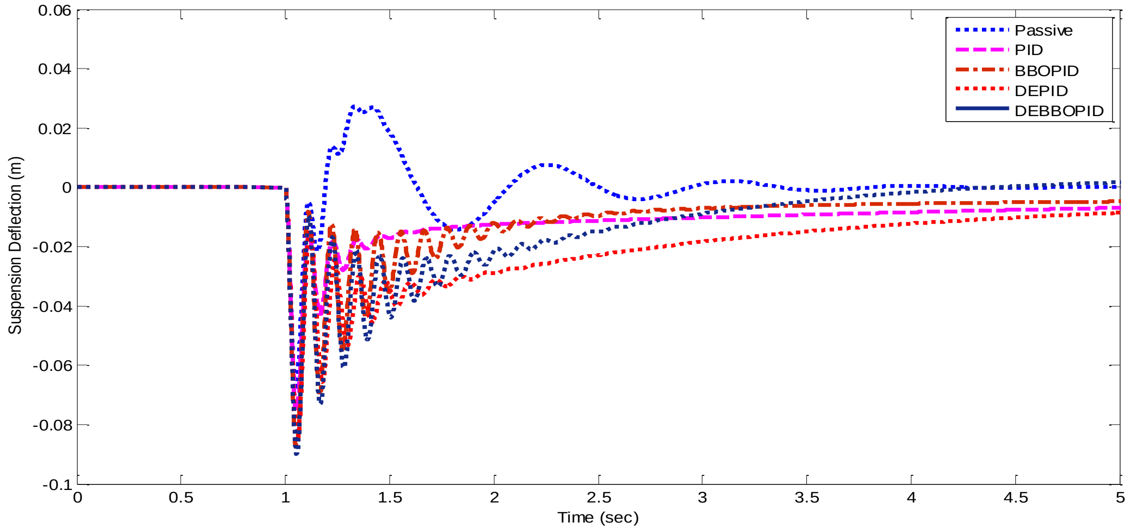


(c)

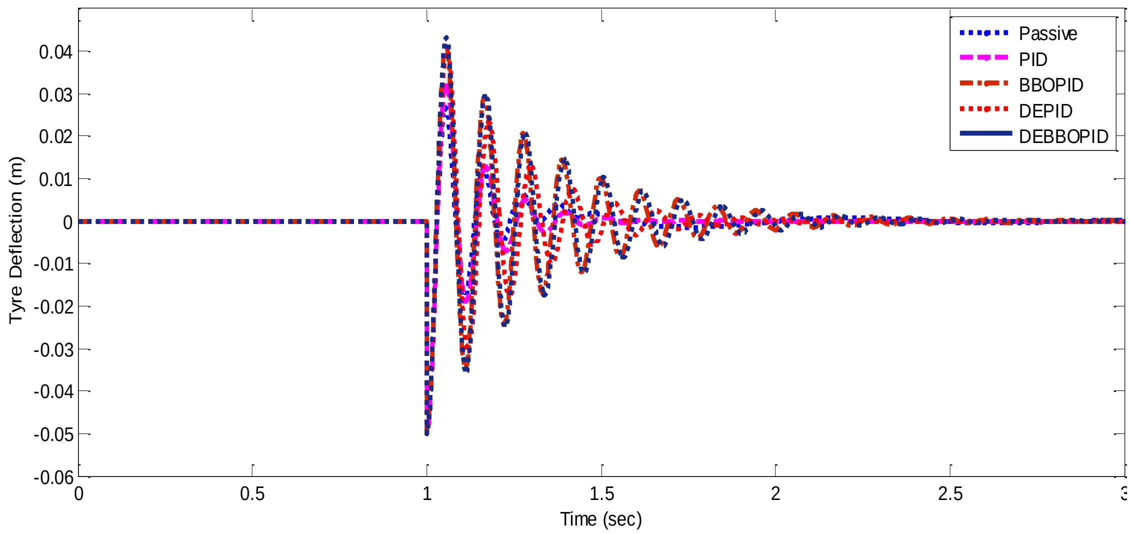


(d)

**Figure 7.** Time responses of quarter car model with step input : (a) Sprung Mass Displacement (b) Body Acceleration (c) Suspension Deflection (d) Tyre Deflection

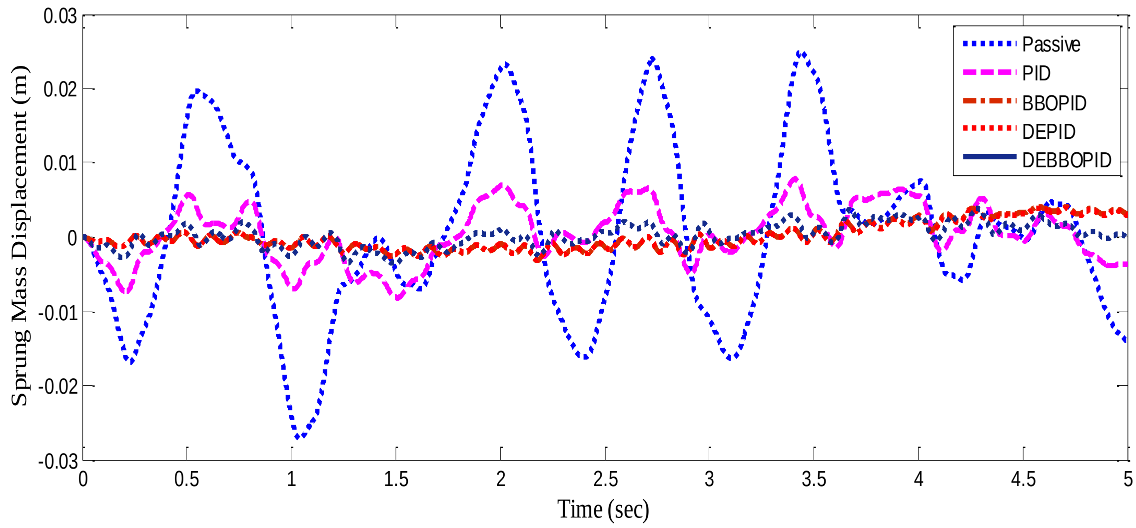


(a)

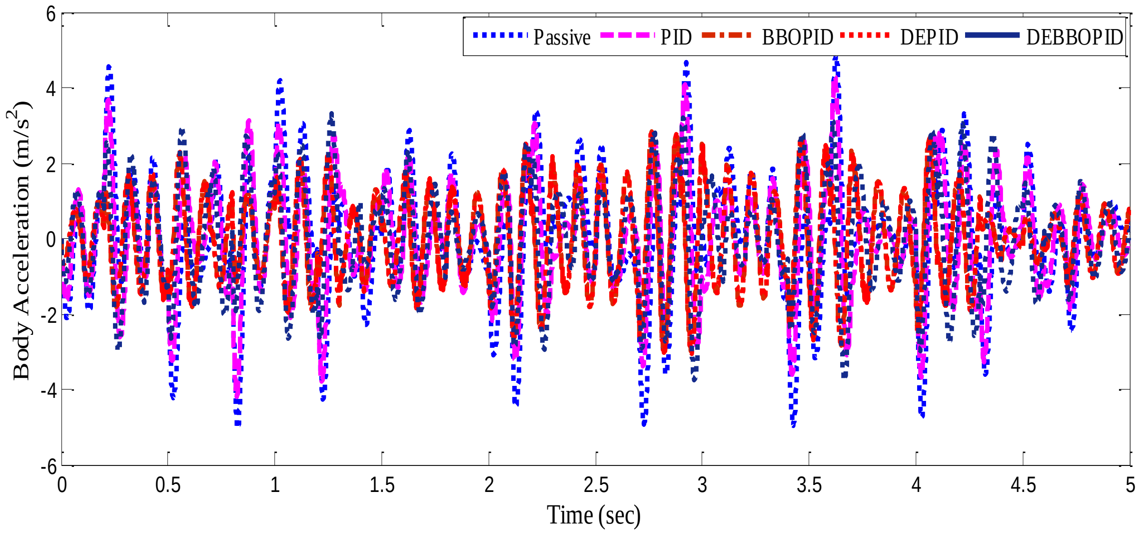


(b)

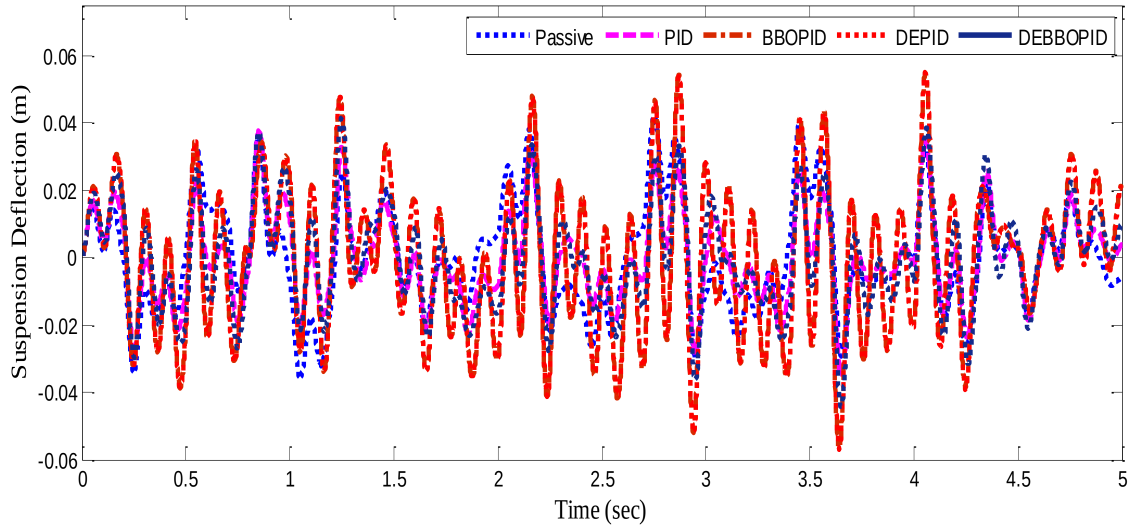


(c )

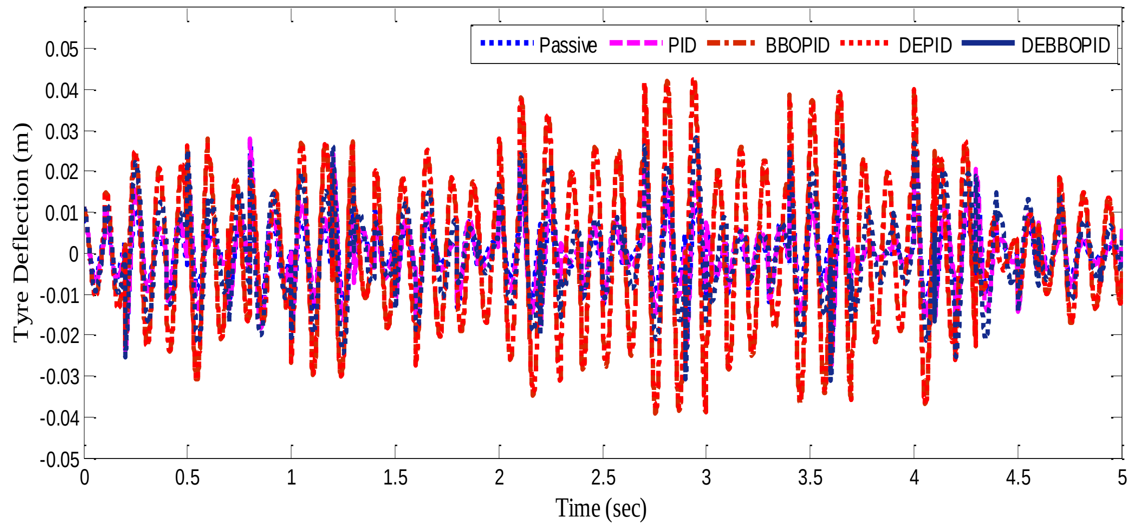


(d)

**Figure 8.** Time responses of quarter car model with random input : (a) Sprung Mass Displacement (b) Body Acceleration (c ) Suspension Deflection (d) Tyre Deflection

The simulation results of *QC* passive system, system with *PID*, *BBOPID*, *DEPID* and *DEBBOPID* controllers are shown in Figures 6, 7 and 8. (a) - (d).

It is clear from Figures 6, 7, 8. (a) and Figures 6, 7, 8. (b) that the sprung mass displacement and vehicle body acceleration is considerably reduced by the proposed *DEBBOPID* controller. It guarantees the travelling comfort to the passengers. Also Figure 6, 7, 8. (c) shows that the suspension deflection with all the controllers are almost the same. Figures 6, 7, 8. (d) illustrate the road holding ability maintained by all the controllers. The tyre displacement of active systems is higher than that of the passive suspension system.

The *RMS* values of the time responses of the four outputs with the three inputs are listed in Tables 2 to 4. It is clear that the *VASS* using *DEBBOPID* controller is useful for the betterment of the ride and travelling comfort with a reduced body acceleration over *PID* controller, with and without *BBO* or *DE* and the passive system.

In the evaluation of the vehicle ride quality, the *PSD* for the body acceleration as a function of frequency is of a prime interest and is plotted for the passive system and that with *PID*, *BBOPID*, *DEPID* and *DEBBOPID* controller for the three different types of road inputs (Figure 9). It is clear from the *PSD* plot that in the human sensitive frequency range 4-8 Hz, compared to *PID*, *BBOPID* and *DEPID*, *DEBBOPID*, reduces the vertical vibrations to a great extent and improves the comfort of travelling when subjected to trapezoidal road input.

**Table 2.** RMS values of the time responses of quarter car model with trapezoidal input

| System | Sprung Mass Displacement ($x10^{-3}$m) | Body Acceleration ($x10^{-3}m/s^2$) | Suspension Deflection ($x10^{-3}$m) | Tyre Deflection ($x10^{-4}$m) |
|---|---|---|---|---|
| **Passive** | 10.61 | 336.6 | 4.81 | 6.168 |
| **PID** | 6.375 | 157.2 | 4.654 | 5.551 |
| **BBOPID** | 6.147 | 113.6 | 6.369 | 5.899 |
| **DEPID** | 4.294 | 98.0 | 7.574 | 7.278 |
| **DEBBOPID** | 5.575 | 82.3 | 7.741 | 6.563 |

**Table 3.** RMS values of the time responses of quarter car model with step input

| System | Sprung Mass Displacement ($x10^{-3}$m) | Body Acceleration ($x10^{-3}m/s^2$) | Suspension Deflection ($x10^{-3}$m) | Tyre Deflection ($x10^{-3}$m) |
|---|---|---|---|---|
| **Passive** | 47.91 | 655 | 6.605 | 2.693 |
| **PID** | 40.36 | 531.9 | 9.842 | 2.903 |
| **BBOPID** | 41.11 | 526.8 | 11.32 | 4.432 |
| **DEPID** | 37.45 | 501.9 | 15.95 | 3.902 |
| **DEBBOPID** | 44.68 | 260.4 | 13.31 | 4.56 |

**Table 4.** RMS values of the time responses of quarter car model with random input

| System | Sprung Mass Displacement ($x10^{-3}$m) | Body Acceleration ($x10^{-3}m/s^2$) | Suspension Deflection ($x10^{-3}$m) | Tyre Deflection ($x10^{-3}$m) |
|---|---|---|---|---|
| **Passive** | 28.43 | 2338.12 | 194.4 | 138.89 |
| **PID** | 21.94 | 1947.34 | 199.22 | 179.32 |
| **BBOPID** | 20.13 | 1802.53 | 201.5 | 193.04 |
| **DEPID** | 22.24 | 1732.521 | 203.45 | 200.13 |
| **DEBBOPID** | 21.35 | 1581.09 | 205.39 | 208.96 |

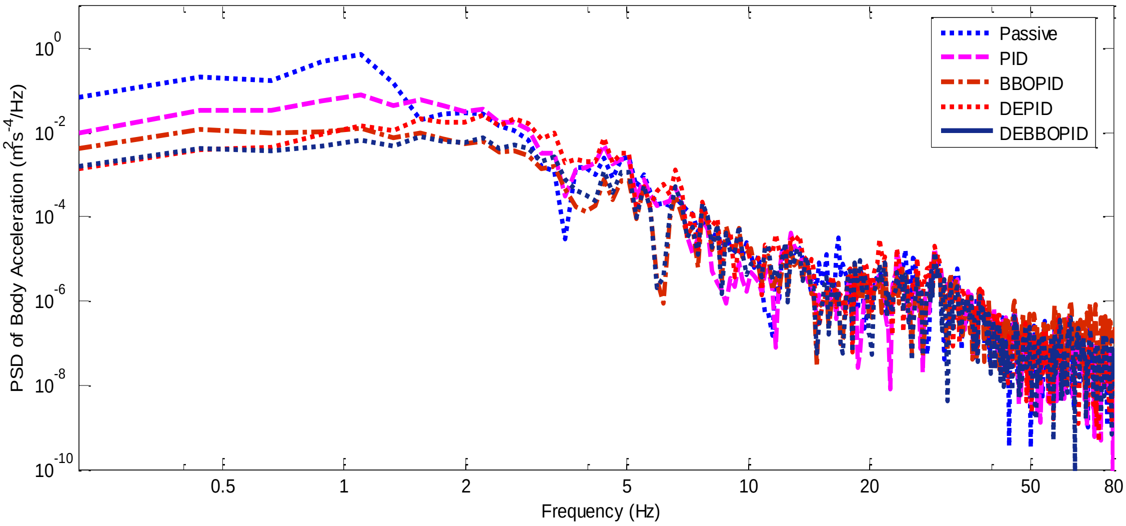


(a)

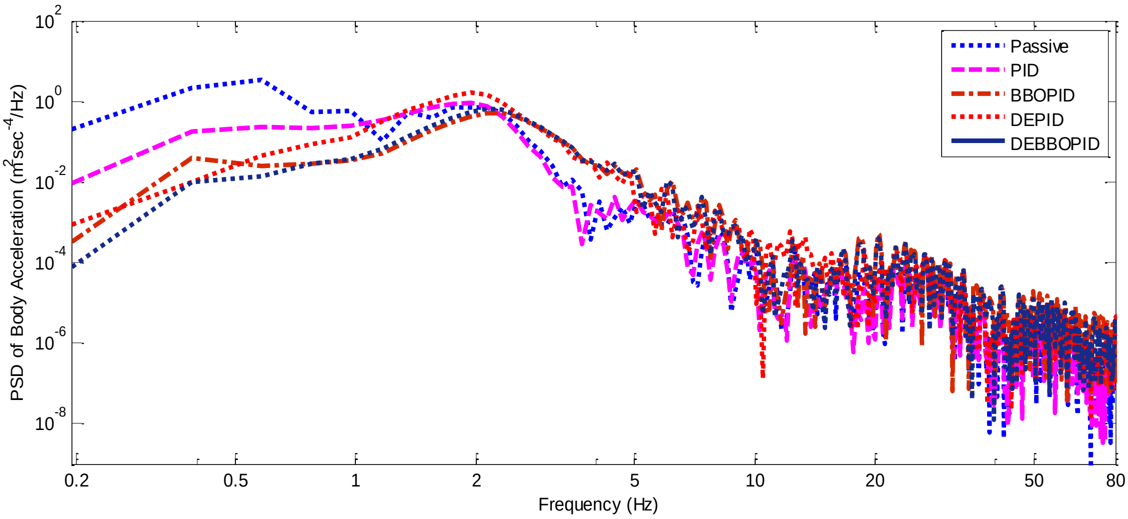


(b)

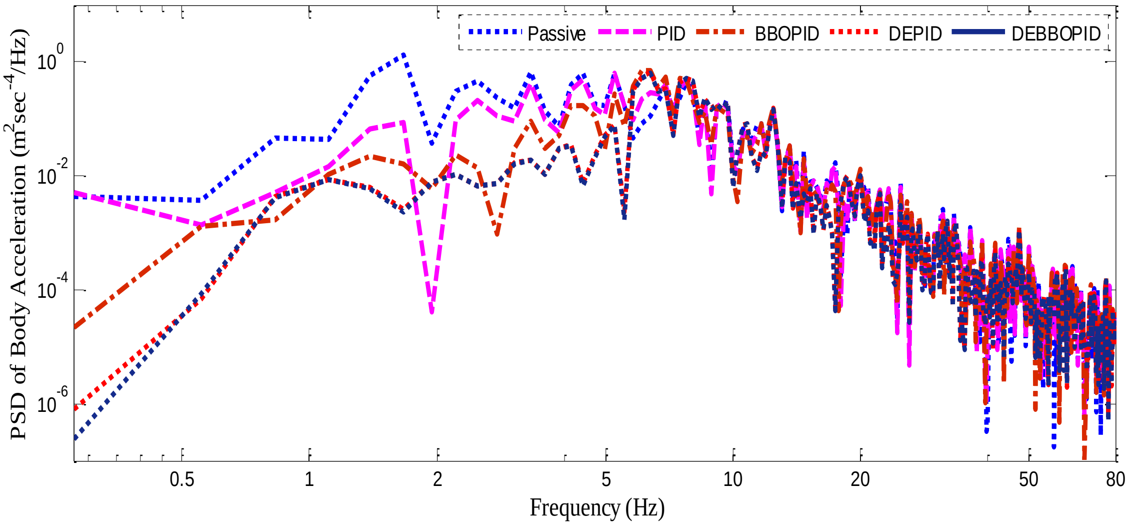


(c)

**Figure 9.** *PSD* of Body acceleration comparison of Passive, *PID*, *BBOPID*, *DEPID* and *DEBBOPID* with (a) Trapezoidal (b) Step and( c) Random type road inputs in quarter car model

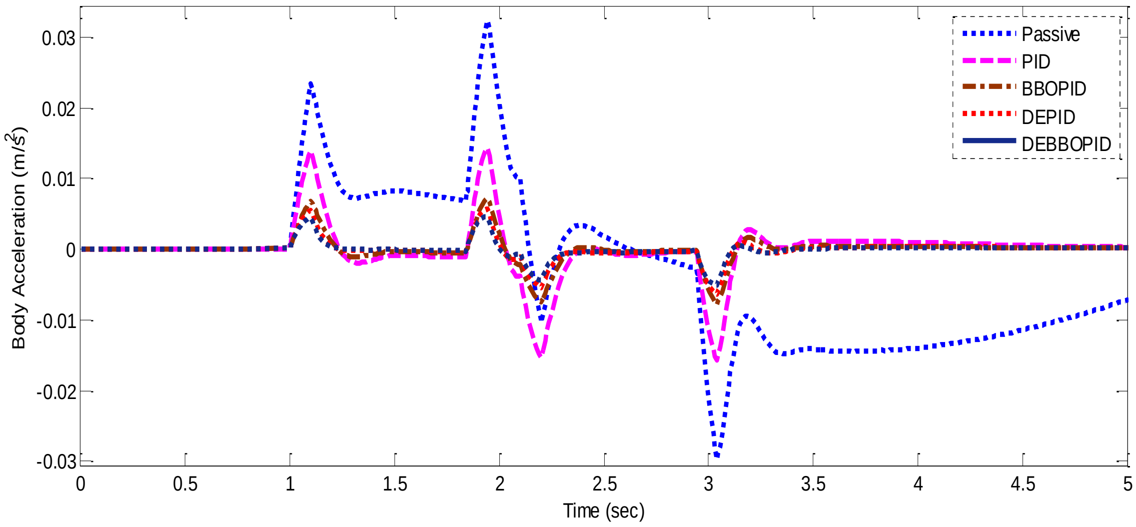


(a)

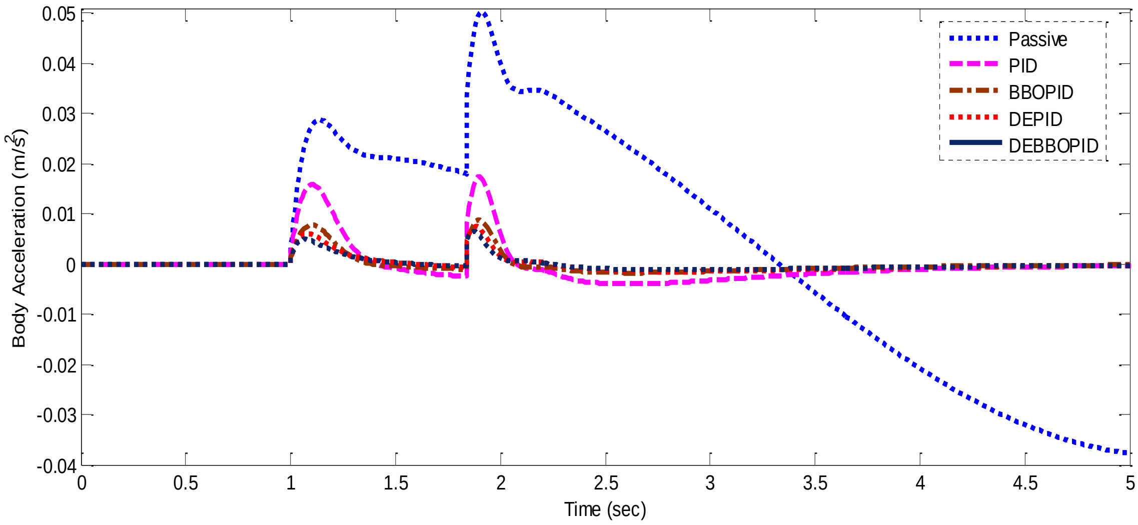


(b)

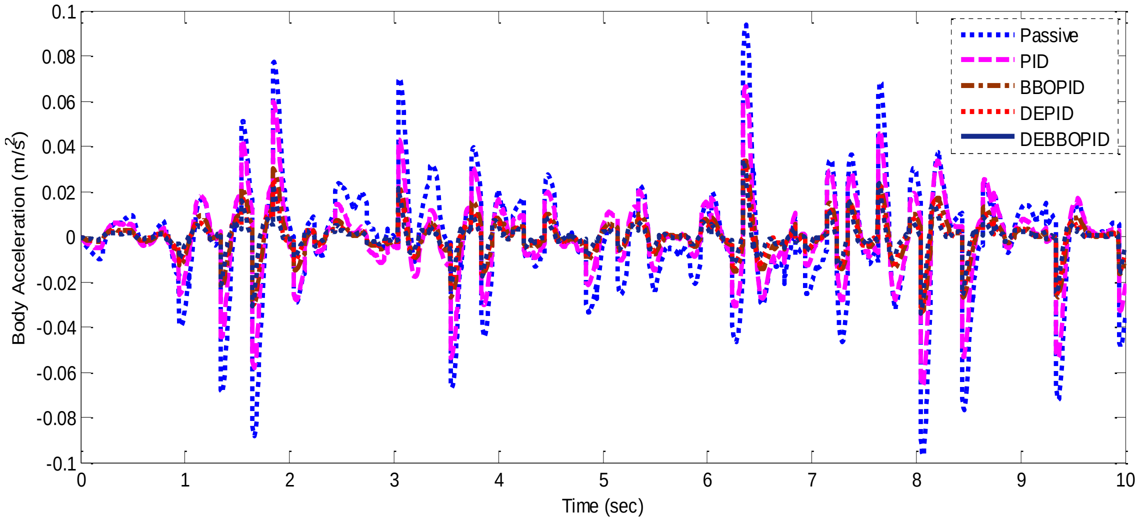


(c)

**Figure 10.** Body acceleration of half car model with (a) Trapezoidal input (b) Step input and (c ) Random input

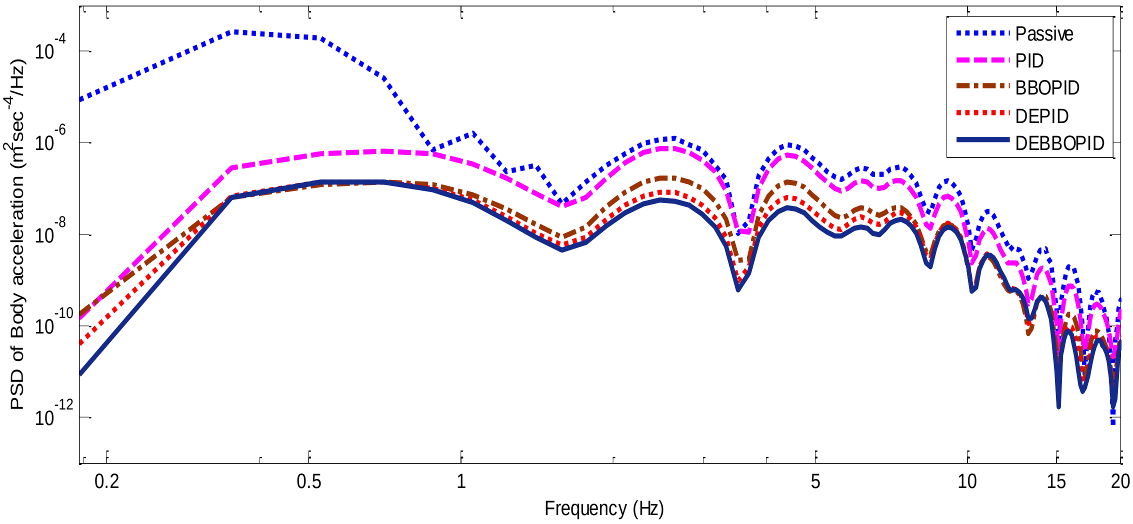


(a)

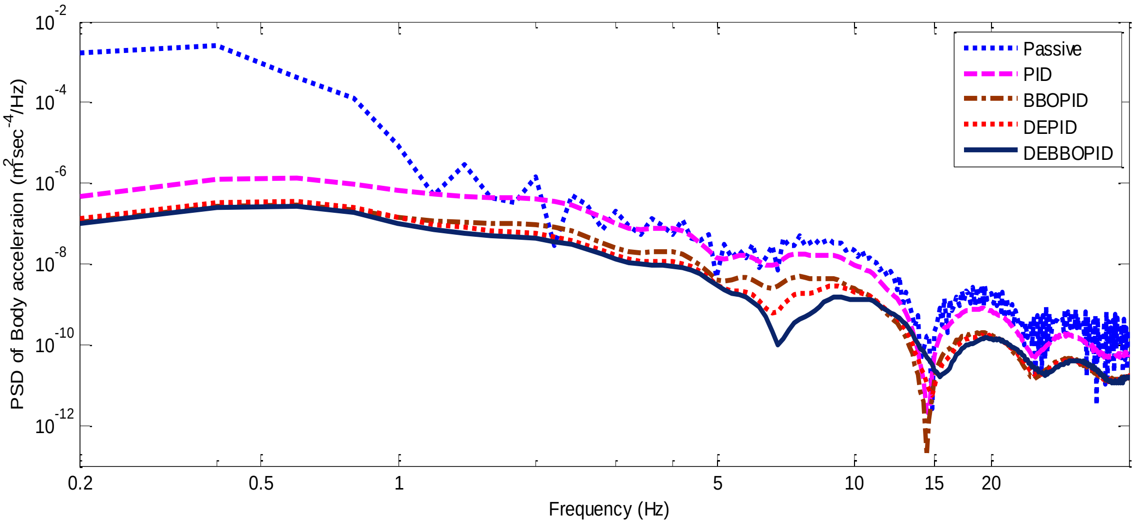


(b)

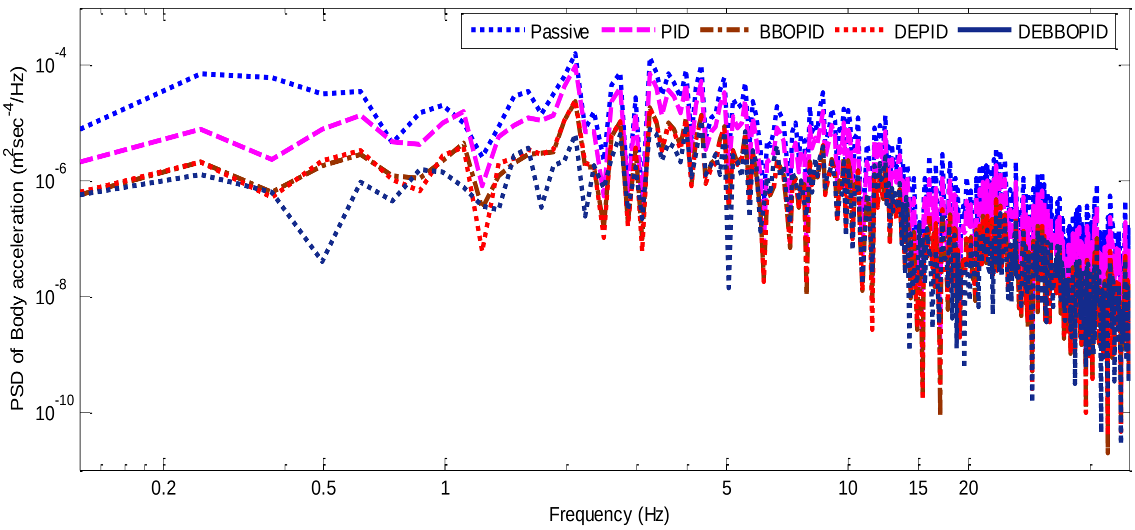


(c)

**Figure 11.** PSD of Body acceleration comparison of Passive, *PID*, *BBOPID*, *DEPID* and *DEBBOPID* with (a) Trapezoidal( b) Step and (c) Random type road inputs in half car model

**Table 5.** RMS values of the body acceleration of half car model

| System | Body Acceleration ($x10^{-6}m/s^2$) | | |
|---|---|---|---|
| | Trapezoidal Input | Step input | Random input |
| **Passive** | 732.92 | 1289.31 | 2935.34 |
| **PID** | 366.67 | 842.25 | 2423.57 |
| **BBOPID** | 178.41 | 524.69 | 2192.04 |
| **DEPID** | 167.49 | 492.18 | 1839.65 |
| **DEBBOPID** | 142.03 | 448.83 | 1643.97 |

The results of the HC passive system, system with PID, BBOPID, DEPID and DEBBOPID controllers simulation are shown in Figures 10 and 11. (a) - (c). Also, the RMS values of the body acceleration of the system for different inputs are tabulated in Table 5, which highlights the effectiveness with the DEBBOPID.

## 5. Conclusions

The optimization of *PID* tuning parameters for the application in *VASS* with linear actuator are discussed in the present paper. Among the three optimization techniques discussed, the *DEBBO* gives a better convergence performance. The *DEBBOPID* results are good compared to the passive system, conventional *PID* controller and *BBOPID* based *VASS*. The *DEBBOPID* reduces the body acceleration considerably and ensures a travelling comfort to the passengers. The controllers, discussed in section 3, are easy to implement and with reference to the *PSD* of body acceleration, it is clear that all the controllers provide a better vibration control compared to the passive system. The *DEBBOPID* gives a better *PSD* and is the best as it converges quickly among the discussed controllers for the control of the vibration in the vehicle.

## References


[1] Seok_il Son. Fuzzy logic controller for an automotive active suspension system. Master's Thesis. Syracuse University; 1996.

[2] D. Hrovat, "Survey of advanced suspension developments and related optimal control applications". Automatica, Vol. 33 (1997), 171-181.

[3] D. Hrovart, "Applications of optimal control to dynamic advanced automotive suspension design". ASME Journal of Dynamic Systems, Measurement and Control, (Special issue commemorating 50 years of the DSC division), Vol. 115 (1993), 328-342.

[4] E. Esmailzadeh, H.D. Taghirad, "Active vehicle suspensions with optimal state feedback control". J. Mech. Sci., Vol. 200 (1996), 1-18.

[5] MO. Abdalla, N. Al Shabatat, M. Al Qaisi, "Linear matrix inequality based control of vehicle active suspension system". Vehicle System Dynamics, Vol. 47 (2007), 121-134.

[6] K. Rajeswari, P. Lakshmi, "Vibration control of mechanical suspension system". Int. J. Instrumentation Technology, Vol. 1 (2011), 60-71.

[7] O. Demir, Keskin, S. Cetlin, "Modelling and control of a nonlinear half vehicle suspension system; A hybrid fuzzy logic approach". Nonlinear Dynamics, Vol. 67 (2012), 2139-2151.

[8] C. Yeroglu, N. Tan, "Design of robust PI controller for vehicle suspension system". Journal of Electrical Engineering & Technology, Vol. 3 (2008), 135-142.

[9] Dan Simon, "Biogeography based optimization". IEEE Transactions on Evolutionary Computation, Vol. 12 (2008), 702-713.

[10] V.K. Panchal, Parminder Singh, Navdeep Kaur, Harish Kundra, "Biogeography based satellite image classification". International Journal of Computer Science and Information Security, Vol. 6 (2009), 269-274.

[11] Urvinder Singh, Harish Kumar, Tara Singh Kamal, "Design of Yagi-Uda antenna using biogeography based optimization". IEEE Transactions on Antennas and Propagation, Vol. 58 (2010), 3375- 3379.

[12] Aniruddha Bhattacharya, Pranab Kumar Chattopadhyay, "Biogeography-based optimization for different economic load dispatch problems". IEEE Transactions on Power Systems, Vol. 25 (2010), 1064-1077.

[13] Dan Simon, "A dynamic system model of biogeography-based optimization". Applied Soft Computing, Vol. 11 (2011), 5652–5661.

[14] Abhishek Sinha, Swagatam Das, B. K. Panigrahi, "A linear state-space analysis of the migration model in an island biogeography system". IEEE Transactions on Systems, Man, and Cybernetics—Part A: Systems and Humans, Vol. 41 (2011), 331-337.

[15] K. Jamuna, K.S. Swarup, "Multi-objective biogeography based optimization for optimal PMU placement". Applied Soft Computing, Vol. 12 (2012), 1503-1510.

[16] Aniruddha Bhattacharya, Pranab Kumar Chattopadhyay, "Closure to discussion of "hybrid differential evolution with biogeography-based optimization for solution of economic load dispatch"". IEEE Transactions on Power Systems, Vol. 27 (2012), 575.

[17] Haiping Maa, Dan Simon, Minrui Fei, Zhikun Xie, "Variations of biogeography-based optimization and Markov analysis". Information Sciences, Vol. 220 (2013), 492–506.

[18] M. R. Lohokare, S. S. Pattnaik, B. K. Panigrahi, Sanjoy Das, "Accelerated biogeography based optimization with neighborhood search for optimization". Applied Soft Computing, In press, Unpublished, available on line (2013).

[19] Ilhem Boussaïd, Amitava Chatterjee, Patrick Siarry, Mohamed Ahmed-Nacer, "Hybridizing biogeography-based optimization with differential evolution for optimal power allocation in wireless sensor networks", IEEE Transactions on Vehicular Technology, Vol. 60 (2011), 2347-2353.

[20] K. Rajeswari, P. Lakshmi, "Simulation of suspension system with intelligent active force control". International Conference on Advances in Recent Technologies in Communication and Computing, Chennai, India, 2010.

[21] Yahaya Md. Sam, Johari Halim Shah Bin Osman, "Modeling and control of the active suspension system using proportional integral sliding mode approach". Asian Journal of Control, Vol. 7 (2005), 91-98.

[22] L.C. Saikia, S.K. Das, P. Dash, M. Raju, "Multi — Area AGC with AC/DC link and BES and Cuckoo Search optimized PID controller". 3rd International Conference on Computer, Communication, Control and Information Technology, Hooghly, India, 2015.

[23] T. A. Boghdady, M. M. Sayed, A. M. Emam, E. E. Abu El-Zahab, "A Novel Technique for PID Tuning by Linearized Biogeography-Based Optimization". IEEE 17th International Conference on Computational Science and Engineering, Chengdu, China, 2014.

[24] R. Storn, K. Price, "Differential evolution - a simple and efficient heuristic for global optimization over continuous

spaces". Journal of Global Optimization, Vol. 11 (1997), 341-359.

[25] Rukmini V Kasarapu, Vijaya B. Vommi, "Economic design of joint $X$ and R control charts using differential evolution". Jordan Journal of Mechanical and Industrial Engineering, Vol. 5, (2011) No. 2, 149-160.

[26] Aniruddha Bhattacharya, P.K. Chattopadhyay, "Hybrid differential evolution with biogeography-based optimization algorithm for solution of economic emission load dispatch problems". Expert Systems with Applications, Vol. 38 (2011), 14001–14010.

[27] R. Kalaivani, P. Lakshmi, K. Sudhagar, "Hybrid (DEBBO) Fuzzy Logic Controller for quarter car model: DEBBOFLC for Quarter Car model". UKACC International Conference on Control (CONTROL), Loughborough, U.K., 2014.

JJMIE

Volume 9 Number 2, April.2015
ISSN 1995-6665
Pages 103 - 111

Jordan Journal of Mechanical and Industrial Engineering

# Simplified Mathematical Modeling of Temperature Rise in Turning Operation Using MATLAB

Ajay Goyal* [a], Rajesh Kumar Sharma [b]

[a]Department of Mechanical Engineeringt, GLA University, Mathura (U.P.) India
[b]Department of Mechanical Engineering, National Institute of Technology, Hamirpur (H.P.) India

Received 7 Sep 2014 Accepted 1 April 2015

**Abstract**

The problem of temperature rise at work piece and chip can be overcome to an extent by using already developed analytical models. But it is believed that these models comprise a very complicated equation and could not be evaluated easily in a very short (in seconds) time using any of the available mathematical softwares. For this, an attempt has been made to simplify an analytical model (capable of determining temperature rise distribution at chip side due to combined effect of deformation zones) by relating it to cutting parameters (basic machining parameters) followed by a step-by-step evaluation of the analytical equation using MATLAB® programming. It is seen that the developed coding can also be used to determine the temperature rise distribution at work piece due to deformation zones with small changes. Both codings are separately validated using previously obtained results by scientists.

The developed coding may be used for selecting optimum cutting parameters during machining. Moreover, developed coding may help industries to estimate the temperature rise at various points of chip and work piece for any set of machining parameters during the start of the operation itself and, thus, reducing planning and idle time.



**Keywords:** *Machining, Temperature Rise, Work Piece, Chip, Analytical Model, MATLAB*.

## 1. Introduction

Machining is a process for removal of material in the form of chips to give work piece desired dimensions and shape by using cutting tools. A lot of energy is consumed while machining and most of it gets converted into heat energy due to the generation of deformation zones (primary, secondary & tertiary), which directly affects the cost and quality of the product. Generated heat results in the rise of temperature at tool, chip and work piece, which if goes beyond the limit, directly affects the productivity by affecting tool (rapid wear, plastic deformation, thermal flaking, thermal fracture, formation of built up edge, and dimensional inaccuracy) and work piece (oxidation, rapid corrosion, internal cracks, dimensional inaccuracy, burning and poor surface finish) along with the induction of thermal stresses at their surfaces. Temperature rise generation also leads to the formation of undesirable quality of chip [1]; it was also seen that the temperature rise at chip is same as the temperature rise at tool [2]. So it is worth to have an estimation of temperature rise distribution at work piece, chip and tool for various cutting parameters so that the machinability can be improved by obtaining optimum cutting parameters.

There are basically three methods to determine the temperature rise distribution at tool, chip and work piece namely, experimental [3], numerical and analytical [4, 5], each of which has its respective merits and demerits. Numerical methods take a long time to develop the results for a particular set of cutting parameters and it gives accurate results. On the other hand, analytical models (developed by researchers since 1951) claimed to make close approximation of temperature rise distribution at tool, work piece and chip due to deformation zone(s)for any set of machining parameters in very small time[2, 4, 5].

R. Komanduri, Z. B. Hou [2,6,7] and Y. Hunag, S. Y. Liang [8] reported recent analytical models but used FEM to validate the work. A. G. Atkins [9], P. Mottaghizadeh, M. Bagheri [10], B. R. Ramji [11], T. M. El Hossainy, M. H. El-Shazly, M. Abd-Rabou [12] also used FEM for a similar study which is a time consuming method. To the best of the author's knowledge, a method to determine the temperature rise distribution in few seconds, which is usually required during machining, has not been developed so far. In the present paper, an analytical model (with a complex equation), developed by a researcher in the past to determine temperature rise distribution at chip side due to combined effect of primary and secondary deformation zone for turning process, is simplified and is related to

* Corresponding author. e-mail: ajay.goyal2411@gmail.com.

cutting parameters with the help of MATLAB® software so that worker can have an idea about temperature rise generation at chip side in a few seconds during machining just by feeding basic machining parameters. It was further seen that developed coding can also be applied to simplify the modelling equation with small changes, which can determine the temperature rise distribution at work piece due to deformation zones. Both the coding is validated separately with previously obtained results of scientists. The developed coding acts as a generalized model which is applicable to any set of machining parameters (cutting parameters, tool material and geometry, work piece and geometry). These models are applicable for dry turning operations and are applicable for any set of parameters including any other environmental conditions.

Section 2 catalogues the analytical models used in the present work followed by the assumptions taken to solve the modelling equations in section 3. A step-by-step procedure to generate and feed input data, to be used to evaluate both modelling equations, is described in section 4. This procedure is performed by MATLAB® coding and presented in a flowchart. Section 5 deals with the systematic and easy coding developed in MATLAB® software to evaluate modelling equation of chip side followed by its validation with already developed results of scientists. Section 6 deals with changes in previously developed modelling equation for determining the temperature distribution at work piece side followed by its validation with previously obtained results. Sections 7 and 8 present the conclusion and the future scope of the present work.

## 2. Analytical Equations

Komanduri and Hou [6] scored the latest success at developing an accurate analytical model that is capable of determining temperature rise distribution at chip side due to combined effect of deformation zones. Pertaining equation developed from the model is given as equation (1).

To the best of the author's knowledge, they also scored the latest success at developing an analytical model that is capable of determining the temperature rise distribution at work piece due to primary deformation zone very close to accuracy [7]. These modelling equations are applicable to any set of machining parameters for dry turning operations. The pertaining equation developed from the model is given as equation (2). Abbreviations and required basic formulae used to generate input parameters of equation (1 and 2) are given in the appendix.

Now it can be seen that both equations are very complicated and could not be evaluated at any available mathematical software to obtain results easily and with lesser time. Moreover, it needs many input parameters; and an approach to obtain them is not predictive in the equations. Further sections deal with the generation of input parameters with the help of cutting parameters, and the simplification of both equations followed by the assumptions needed to evaluate them.

$$\theta_c = \frac{q_{se}}{\pi k}\left\{(B_c-\Delta B)\int_{l_i=0}^{l} e^{-V_c(X-l_i)/2a}\left[K_0\left(R_iV_c/2a\right)+K_0\left(R_i'V_c/2a\right)\right]dl_i \right.$$
$$+\,2\Delta B\int_{l_i=0}^{l}\left(\frac{l_i}{l}\right)^m e^{-V_c(X-l_i)/2a}\left[K_0\left(R_iV_c/2a\right)+K_0\left(R_i'V_c/2a\right)\right]dl_i$$
$$\left.+\,C\Delta B\int_{l_i=0}^{l}\left(\frac{l_i}{l}\right)^n e^{-V_c(X-l_i)/2a}\left[K_0\left(R_iV_c/2a\right)+K_0\left(R_i'V_c/2a\right)\right]dl_i\right\} \tag{1}$$
$$+\,\frac{q_s}{2\pi k}\int_{w_i=0}^{t_c/\cos(\emptyset-\alpha)} e^{-(X-X_i)^{V_c}/2a}\left\{K_0\left[\frac{V_c}{2a}\sqrt{(X-X_i)^2+(Z-z_i)^2}\right]\right.$$
$$\left.+\;K_0\left[\frac{V_c}{2a}\sqrt{(X-X_i)^2+(2t_c-Z-z_i)^2}\right]\right\}dw_i$$

where,

$X_i = L_{ab}$ - $w_i\sin(\emptyset-\alpha)$, $z_i = w_i\cos(\emptyset-\alpha)$, $R_i=\sqrt{(X-l_i)^2+Z^2}$ and $R_i'=\sqrt{(X-l_i)^2+(2t_c-Z)^2}$

$$\theta_w = \frac{q_s}{2\pi k}\int_{l_i=0}^{L_{ab}} e^{-(X+l_i\cos\emptyset)\frac{V}{2a}}\left\{K_0\left[\frac{V}{2a}\sqrt{((X+l_i cos\emptyset)^2+(z-l_i sin\emptyset)^2)}\right]+\right.$$
$$\left.K_0\left[\frac{V}{2a}\sqrt{((X+l_i cos\emptyset)^2+(z+l_i sin\emptyset)^2)}\right]\right\}dl_i \tag{2}$$

## 3. Assumptions for Computing Modeling Equation

In order to solve the modeling equations, the following assumptions are to be considered:

a) Cutting process is orthogonal.
b) There is no heat loss to surrounding along the primary / secondary heat zones.
c) Preheating effect of the tool and work piece is negligible.
d) Model is applicable for turning process only.
e) Thermal conductivity of work piece and chip is the same and does not change with the change in the temperature.
f) Deformation zones are considered as plane heat source. But in reality, it is basically a zone.
g) Surface of the tool does not worn out during machining and machining is considered to be dry.
h) Heat generated due to tertiary deformation zone can be neglected. Hence, tool insert tip is considered to be sharp.
i) Lower limit of integral (given in equation 1) is taken as 0.000001 instead of zero in MATLAB® coding.

## 4. Theoretical Formulation of Analytical Solutions

The analytical equations to be computed are complex and are not related to cutting parameters. The layman can encounter problems to apply these modeling equations directly on shop floor. If these modeling equations can be simplified and related to cutting parameters then just by feeding the basic input variables, the operator can obtain results in seconds. To accomplish this objective, analytical models, developed by Komanduri and Hou [6, 7], are considered as a basis for study. Then various parameters of the modeling equations are related and evaluated through formulae given in Appendix which helped in relating equations with basic machining parameters. In order to solve the complex integrals in the equations, multiple Simpson's 1/3 rule is applied in coding. The systematic layout of the work is explained with the help of flow diagrams in the subsequent topics.

## 5. Generation of Input Parameters for Model

As mentioned earlier, many input parameters are required to solve the modeling equation. For this, cutting parameters are taken as first input to generate other required input parameters. This is done because the cutting parameters are the most initial input to machining. Moreover, by doing so, the temperature rise at chip and work piece can be controlled by controlling cutting parameters. A step-by-step approach, to generate required parameters, is done by MATLAB® programming and presented in Figure 1, in a flowchart. A brief discussion of Figure 1 is given below.

To solve the analytical equations, the input parameters to be considered are divided into three types namely 1st type, 2nd type and 3rd type. 1st kind of inputs is the obtained values from machining or measurement or they are direct data decided before machining, while 2nd and 3rd types of input are calculated data. 1st kind of input parameters serves as inputs to obtain 2nd type of parameters. Both types together are used to generate 3rd type of input data. Generated input parameters are used to solve modeling equations (1 & 2). In order to evaluate equation (1), MATLAB® coding is prepared as discussed in section 5.

## 6. Mathematical Computation and Validation of Thermal Modelling of Chip Side

This section discusses the coding used to evaluate equation (1) followed by its validation with the obtained results of Komanduri & Hou [6].

### *6.1. Computing Modelling Equation of Chip Side*

This section deals with studying a step wise step procedure to evaluate the model in the form of flow diagrams based on MATLAB® coding.

The entire coding is divided into three parts. 1st part is used to feed 1st kind of input data followed by calculations of 2nd and 3rd kinds of input parameters. A step-by-step feeding and a calculation of data are shown in Figure 1. Formulae used for calculating the data is given in the appendix.

The 2nd division deals with the calculation of definite integrals of the complex functions involved in equation (1). Though MATLAB® software can directly integrate functions using "quad" command, it takes time (sometimes processing hangs the computer) to integrate complicated functions like the ones given in equation (1). To reduce time of calculation, Multiple Segment Simpson's 1/3rd rule is applied and its coding is presented here in the form of a flowchart (Figure 2). The value of the integration of each function is stored in software in "integral" variable.

The 3rd part emphasizes on coding used to evaluate the modelling equation (1) by using Multiple Segment Simpson's 1/3rd rule from part 2 and inputs from part 1 and display temperature rise distribution contour graphs with respect to co-ordinates. A step-by-step procedure for solving the modelling equation is shown in Figure 3.

The coding can be used to calculate the temperature rise distribution at various points of chip for any tool-work combination for turning operation and for any combination of cutting parameters, tool geometry and other cutting conditions in few seconds.

Five functions to be evaluated to solve equation (1) by Multiple Segment Simpson's 1/3rd rule are given by equation (3), (4), (5), (6) and (7), respectively. Values of constants used in modeling equation (1) i.e. *Bchip*, *ΔB*, C, m, & n are approximate values and estimated from Komanduri and Hou's [2, 4, 5, 6] functional analysis. Value of lower and upper limit for 1st and 2nd functions to be integrated are 0.000001 (≈ 0) & shear plane length respectively. Also, the lower and upper limits of 3rd, 4th and 5th functions to be integrated are 0.000001(≈ 0) & tool-chip contact length.

$$f(w_i) = \left(e^{-(X-X_i)^{V_c}/2a}\right) * K_0\left[\frac{V_c}{2a}\sqrt{(X-X_i)^2+(Z-z_i)^2}\right] \quad (3)$$

$$g(w_i) = \left(e^{-(X-X_i)^{V_c}/2a}\right) * K_0\left[\frac{V_c}{2a}\sqrt{(X-X_i)^2+(2t_c-Z-z_i)^2}\right] \quad (4)$$

 

$$h(l_i) = (e^{-V_c(X-l_i)/2a}) * [K_0({R_i V_c}/{2a}) + K_0({R_i' V_c}/{2a})] \quad (5)$$

$$j(l_i) = \left(\frac{l_i}{l}\right)^m e^{-V_c(X-l_i)/2a} * [K_0({R_i V_c}/{2a}) + K_0({R_i' V_c}/{2a})] \quad (6)$$

$$s(l_i) = \left(\frac{l_i}{l}\right)^n e^{-V_c(X-l_i)/2a} * [K_0({R_i V_c}/{2a}) + K_0({R_i' V_c}/{2a})] \quad (7)$$

$$X_i \& z_i = function\ of\ (w_i),$$
$$R_i \& R_i' = function\ of\ l_i$$

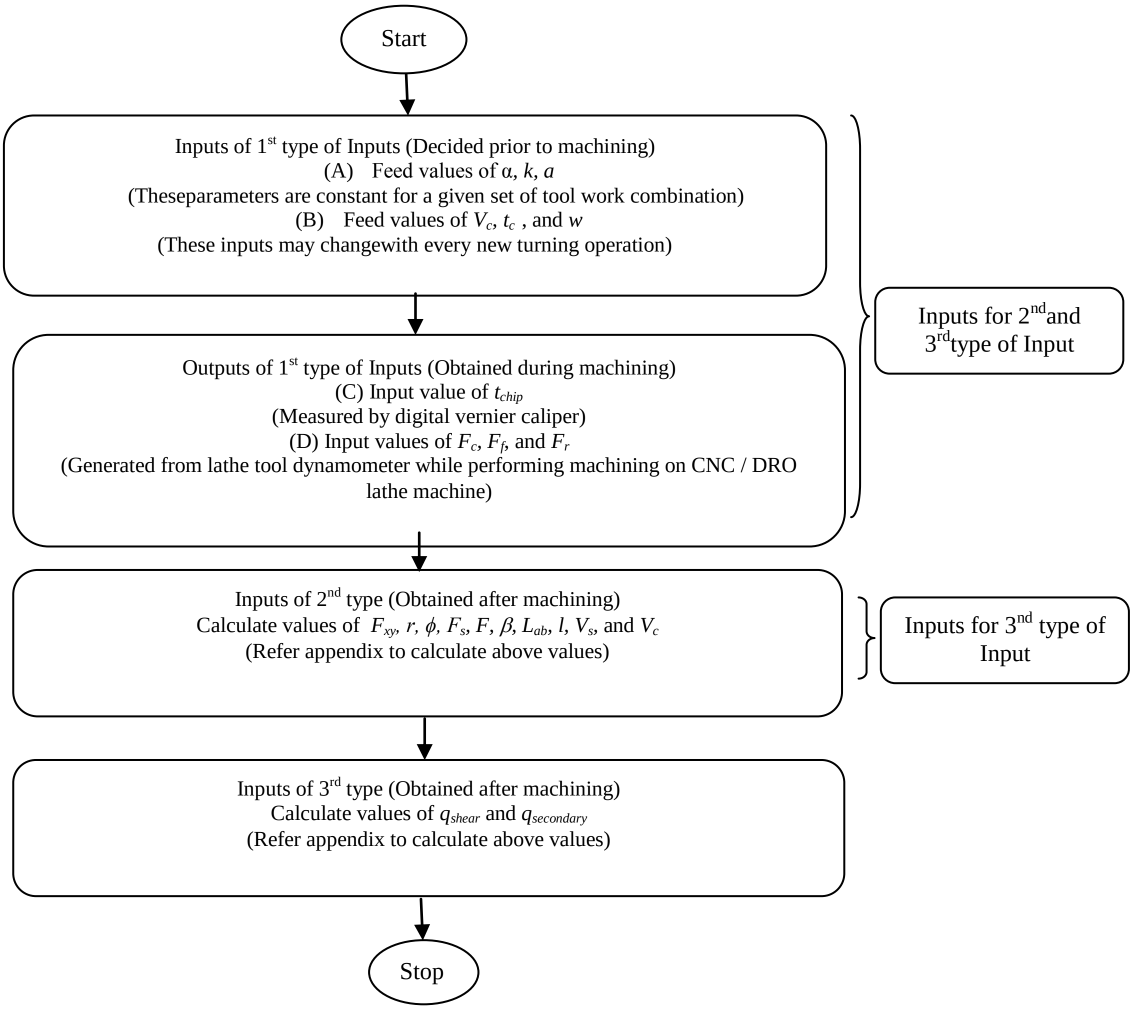


**Figure 1**. Flowchart showing step by step procedure to feed and calculate input data of all kinds needed to evaluate equation (1)

*6.2. Validation of Program*

Komanduri and Hou used Chao and Trigger's input parameters [12] (Table 1) for evaluating equation (1) and obtaining temperature rise distribution on chip side due to combined effect of primary and secondary heat source. MATLAB® coding is tested using same input parameters and temperature rise contours obtained from the program are depicted in Figure 4.

Comparing Figure 4 and results obtained in [6], it is observed that output results of both approaches match with a close proximity (maximum temperature value difference is 2°C). Therefore, the program can be considered for validation.

**7. Mathematical Computation and Validation of Thermal Modelling of Work Piece Side:**

This section emphasises the discussion of coding used to evaluate equation (2) followed by its validation with the results obtained by Komanduri & Hou [6].

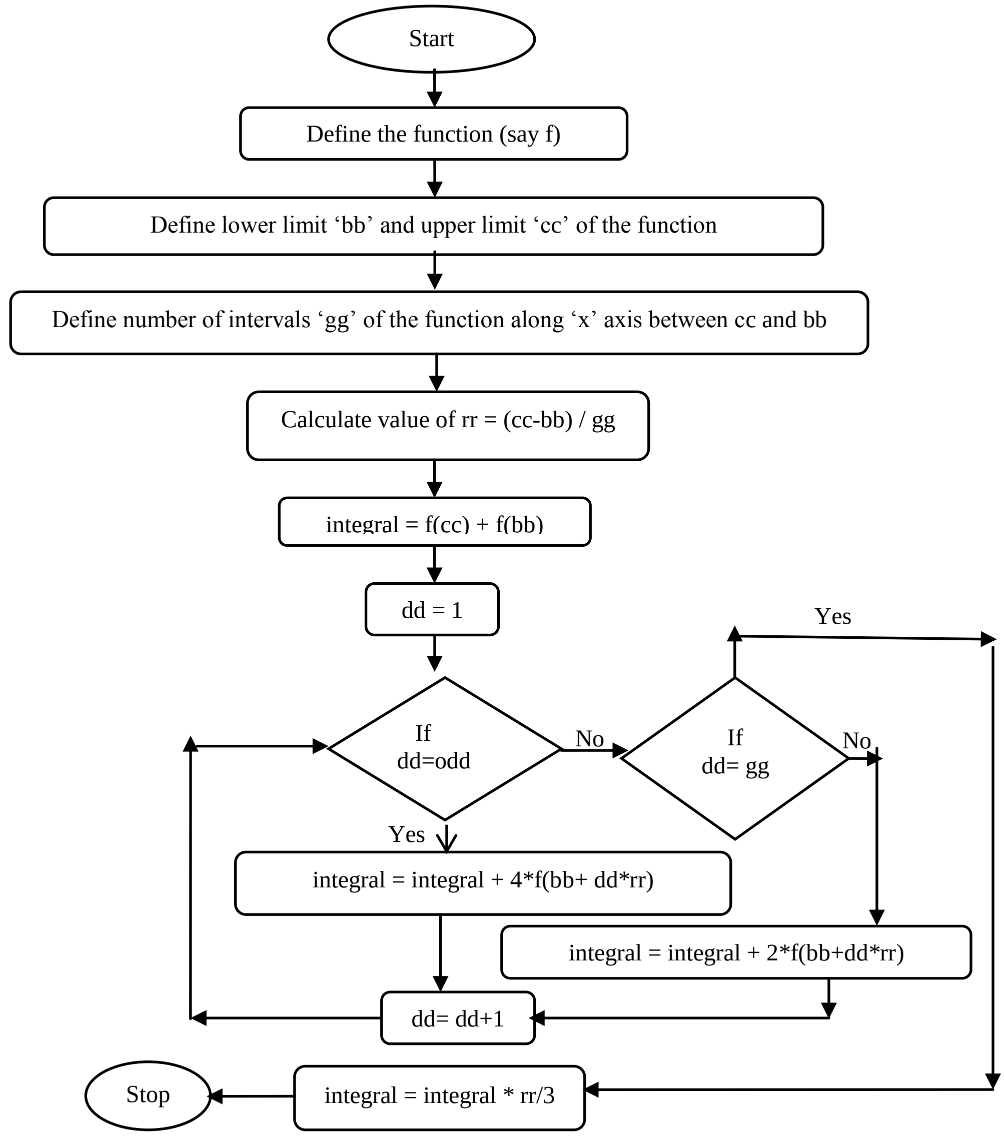


**Figure 2**. Flowchart showing step by step procedure to calculate definite integrals in MATLAB® by using Multiple Segment Simpson’s 1/3rd rule

*7.1. Computing Modelling Equation of Work Piece Side*

It was noticed that the coding developed in section 5.1 can be used to evaluate equation (2) by changing functions (f, g, h, j, & s) used in equations (3,4,5,6,7), respectively. This can be done by replacing function f by $f_1$, g by $g_1$, h by $h_1$ and so on. These changed functions are given in equations (8,9,10).

$$f_1(l_i) = e^{-(X+l_i cos\phi)\frac{V}{2a}} K_0 * \left[\frac{V_c}{2a}\sqrt{((X+l_i cos\phi)^2 + (Z-l_i sin\phi)^2)}\right] \quad (8)$$

$$g_1(l_i) = e^{-(X+l_i\ cos\phi)\frac{V}{2a}} K_0 * \left[\frac{V_c}{2a}\sqrt{((X+l_i cos\phi)^2 + (Z+l_i sin\phi)^2)}\right] \quad (9)$$

$$h_1(l_i) = 0 = j_1(l_i) = s_1(l_i) \quad (10)$$

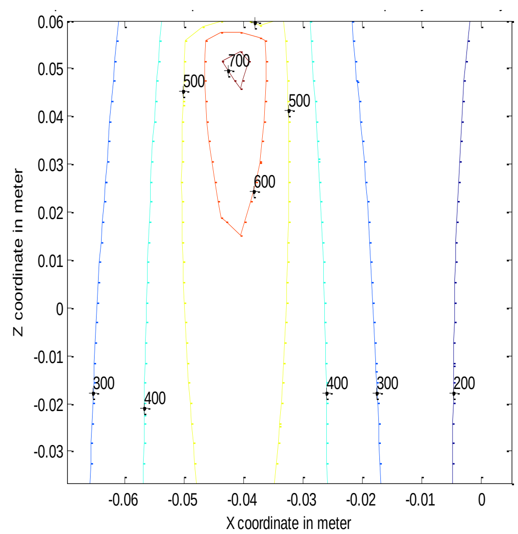


**Figure 4.** Temperature rise contours at various points of chip due to combined effect of two deformation zones using input parameters of Table 1 and developed MATLAB®coding

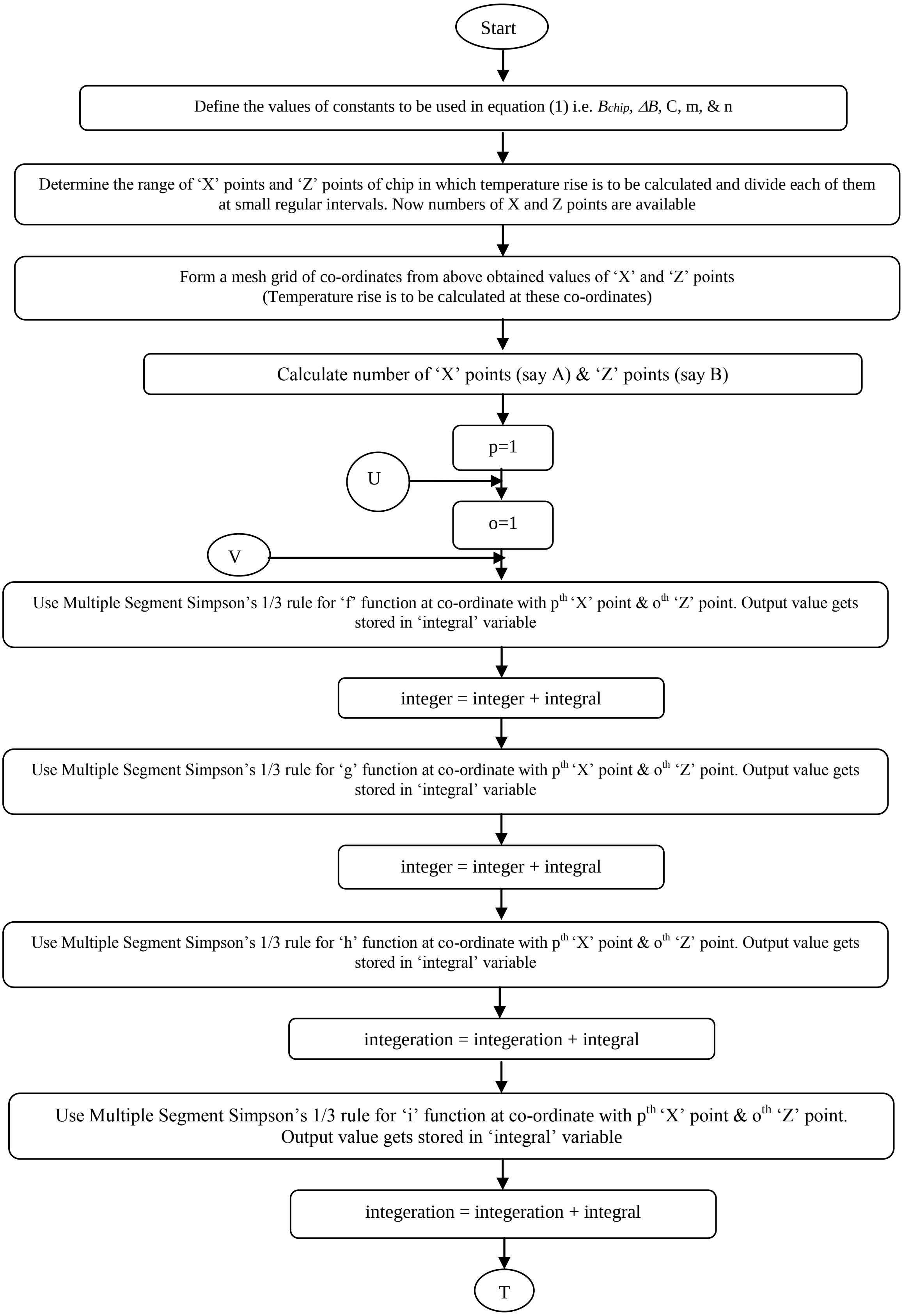
Start
Define the values of constants to be used in equation (1) i.e. $B_{chip}$, $\Delta B$, C, m, & n
Determine the range of ‘X’ points and ‘Z’ points of chip in which temperature rise is to be calculated and divide each of them at small regular intervals. Now numbers of X and Z points are available
Form a mesh grid of co-ordinates from above obtained values of ‘X’ and ‘Z’ points
(Temperature rise is to be calculated at these co-ordinates)
Calculate number of ‘X’ points (say A) & ‘Z’ points (say B)
p=1
U
o=1
V
Use Multiple Segment Simpson’s 1/3 rule for ‘f’ function at co-ordinate with p$^{th}$ ‘X’ point & o$^{th}$ ‘Z’ point. Output value gets stored in ‘integral’ variable
integer = integer + integral
Use Multiple Segment Simpson’s 1/3 rule for ‘g’ function at co-ordinate with p$^{th}$ ‘X’ point & o$^{th}$ ‘Z’ point. Output value gets stored in ‘integral’ variable
integer = integer + integral
Use Multiple Segment Simpson’s 1/3 rule for ‘h’ function at co-ordinate with p$^{th}$ ‘X’ point & o$^{th}$ ‘Z’ point. Output value gets stored in ‘integral’ variable
integeration = integeration + integral
Use Multiple Segment Simpson’s 1/3 rule for ‘i’ function at co-ordinate with p$^{th}$ ‘X’ point & o$^{th}$ ‘Z’ point. Output value gets stored in ‘integral’ variable
integeration = integeration + integral
T

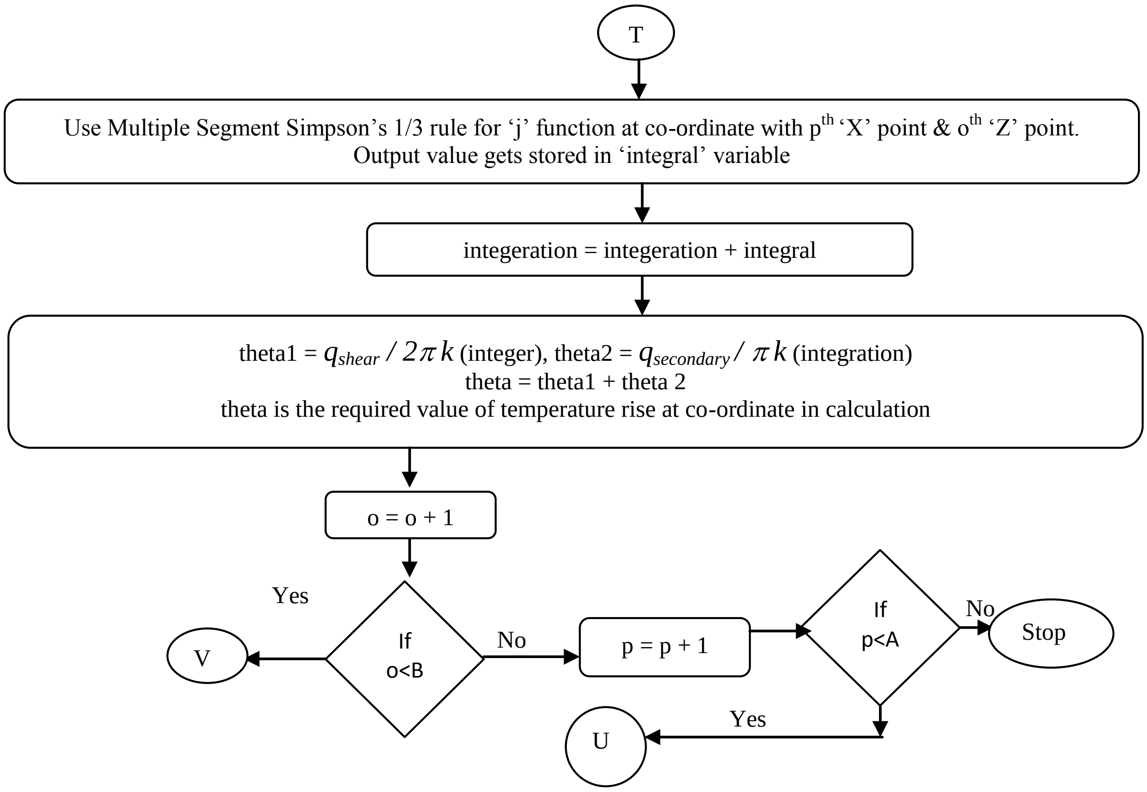


**Figure 3**. Step by step procedure to evaluate modeling equation (1) using Multiple Simpsons 1/3rd Rule (refer section 5) and input parameters to be used (refer section 4).

**Table 1.** Chao and Trigger's machining input parameters [12]

| | |
|---|---|
| Work material | Steel NE 9445 |
| Range of X co-ordinate | -700 µm to 50 µm |
| Range of Z co-ordinate | - 400µm to 600 µm |
| Tool | Triple carbide 4° rake |
| Cutting Velocity | 152.4 cm/sec. |
| Depth of Cut | 0.02489 cm |
| Width of Cut | 0.2591 cm |
| Chip Contact Length | 0.023 cm |
| Main Cutting Force | 1681.3 N |
| Feed Force | 854 N |
| Passive Force | Zero N |
| Chip Thickness | 0.06637 |
| Thermal Diffusivity | 0.3777 cm$^2$/sec. |
| Thermal Conductivity | 0.08234 Watt/cm °C |
| $B_c$= 0.652, $\Delta B$ = 0.312, C= 2.2, m= 0.26, & n= 16 | |

### *7.2. Validation of Coding for work piece Side*

Komanduri and Hou used Lowen and Shaw's input parameters [9] (refer to Table 2) for validating equation (2) by obtaining temperature rise distribution on work piece due to primary heat source. Changed MATLAB® coding is tested using the same input parameters and temperature rise contours obtained from the program are depicted in Figure 5.

Comparing both the figures 5 and results obtained in [7], it can be noted that both results give almost the same output with a very little variation of temperature rise (maximum temperature rise value variation is 10°). Therefore, the program can be considered for validation. In the model, moving a co-ordinate system has been considered. Komanduri and Hou calculated the temperature rise distribution at an instantaneous co-ordinate system which is different from the author's consideration. Hence, the temperature rise distribution, in our result, is shifted from Komanduri and Hou's results.

## 8. Conclusion and Future Scope

By using the coding, industries can estimate the temperature rise distribution at various points of chip and work piece due to deformation zones for any machining parameters during the turning operation itself and, thus, reducing planning and the idle time. Moreover, by generating temperature rise distribution at chip side for particular machining parameters, one can also predict distribution of temperature at tool side since the temperature rise distribution is almost the same at both chip & tool for a particular tool-work combination. Coding shows how the basic machining parameters are connected with complex modeling equations so that by feeding them one can get the output results. Also, MATLAB® software is cheap and readily available. Moreover, the flowchart developed for the coding can act as a study material for other programmers to develop a similar coding on other software and, thus, increasing the compatibility of the work.

Apart from the work conveyed in the present article, further work can be done in this area in the future:

- The MATLAB® coding developed in the work can be used to calculate thermal stresses developed during machining at various points of chip and work piece.
- The coding can be modified for other simple operations (like facing) and complicated processes (like milling, grinding, drilling, etc.)
- The coding can be used to determine optimum cutting parameters for a particular tool-work combination. For this, various combinations of cutting parameters (using full factorial) can be tested to generate temperature rise distribution from a range of cutting parameters.

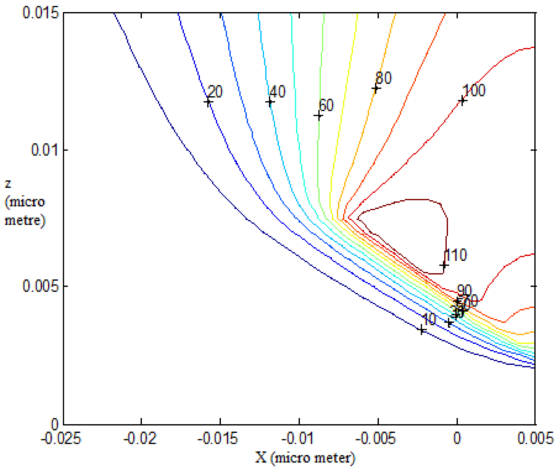


**Figure 5**. Temperature rise contours at various points of work piece due to primary deformation zone developed from MATLAB coding

**Table 2.** Cutting data for machining steel from Loewen & Shaw [13]

| Work material | SAE B1113 steel |
|---|---|
| Tool | K2S carbide 20°rake, 5° clearance |
| Cutting Velocity | 232cm/sec. |
| Depth of cut | 0.006 |
| Width of Cut | 0.384cm |
| Chip Contact Length | 0.023cm |
| Main Cutting Force | 356 N |
| Feed Force | 125N |
| Passive Force | Zero N |
| Chip Thickness Ratio | 0.51 |
| Thermal Diffusivity | 0.1484 sq.cm/sec. |
| Thermal Conductivity | 0.567Watt/cm deg. cel. |
| Range of X co-ordinate | -250 to 50 µm |
| Range of Z co-ordinate | -150 to 0 µm |

## Acknowledgement

We would like to thank Late Shri Suresh Dhiman who helped us during the tenure work. We would also like to thank the National Institute of Technology, Hamirpur (H.P.) India, for providing us with the required environment and resources needed during the work.

## References

[1] A.B. Chattopadhyay. Cutting temperature causes, effects, assessment and control. In: IIT Kharagpur MHRD NEPTEL Manufacturing Science II, lecture 11, Version 2.

[2] R. Komanduri, Z.B. Hou, “Thermal modeling of the metal cutting process * Part II: temperature rise distribution due to frictional heat source at the tool-chip interface”. International Journal of Mechanical Sciences, Vol. 43 (2001), 57-88.

[3] A. Goyal, S. Dhiman, R.K. Sharma, S.K. Tyagi, “A Study of Experimental Temperature Measuring Techniques used in Metal Cutting”. Jordan Journal of Mechanical and Industrial Engineering, Vol. 8 (2014) No. 2, 82-93.

[4] A. Goyal, S. Dhiman, R.K. Sharma, S.K. Tyagi, “Studying Analytical Models of Heat Generation at Three Different Zones in Metal Cutting”. 3rd International Conference on Production and Industrial Engineering, National Institute of Technology, Jalandhar, India 2013.

[5] A. Goyal, S. Dhiman, R.K. Sharma, S.K. Tyagi, “Studying Methods of Estimating Heat Generation at Three Different Zones in Metal Cutting: A Review of Analytical models”. International Journal of Engineering Trends and Technology, Vol. 8 (2014) No.10, 532-545.

[6] R. Komanduri, Z.B. Hou, “Thermal modeling of the metal cutting process - Part III: temperature rise distribution due to the combined effects of shear plane heat source and the tool-chip interface frictional heat source”. International Journal of Mechanical Sciences, Vol. 43 (2001), 89-107.

[7] R. Komanduri, Z.B. Hou, “Thermal modeling of the metal cutting process Part I * Temperature rise distribution due to shear plane heat source”. International Journal of Mechanical Sciences, Vol. 42 (2000), 1715-1752.

[8] Y. Huang, S.Y. Liang, “Cutting forces modeling considering the effect of tool thermal property—application to CBN hard turning”. International Journal of Machine Tools and Manufacture, Vol. 3(2003), 307-315.

[9] A.G. Atkins, “Modelling metal cutting using modern ductile fracture mechanics:quantitative explanations for some longstanding problems”. International Journal of Mechanical Sciences, Vol. 45 (2003), 373–396.

[10] P. Mottaghizadeh, M. Bagheri, “3D Modeling of Temperature by Finite Element in Machining with Experimental Authorization”. World Academy of Science, Engineering and Technology, Vol. 68 (2012), 1728-1734.

[11] B.R. Ramji, H. N. N. Murthy, M. Krishna, “Analysis of forces, roughness, wear and temperature in turning cast iron using cryotreated carbide inserts”. International Journal of Engineering Science and Technology, Vol. 2(7), 2010, 2521-2529.

[12] B.T. Chao, K.J. Trigger,“Temperature distribution at the tool-chip interface in metal cutting”. Transactions of ASME, Vol. 75 (1995), 1107-21.

[13] E.G. Loewen, M.C. Shaw,“On the analysis of cutting tool temperatures”. Transactions of ASME, Vol. 71 (1954),217-31.

## Appendix

| Abbreviations | Details | Source | Unit |
|---|---|---|---|
| $\theta_c$ | Temperature rise at chip due to primary and secondary deformation zone | Refer equation (1) | $^{\circ}$C |
| $\theta_w$ | Temperature rise at work piece due to primary deformation zone | Refer equation (2) | $^{\circ}$C |
| $\alpha$ | Rake angle | Tool specifications | $^{\circ}$ |
| $t_d$ | Undeformed chip thickness | = depth of cut | cm |
| $t_c$ | Deformed chip thickness | Digital Vernier Calliper | cm |
| $r$ | Chip thickness ratio | $t_c/t_{chip}$ | -- |
| $\phi$ | Shear angle | $tan^{-}\frac{r\ cos \propto}{1 - r\ sin \propto}$ | $^{\circ}$ |
| $w$ | Width of chip | = feed rate | cm |
| $X$, $Z$ | X and Z co-ordinate at which temperature rise is to be calculated | --- | µm |
| $F_c$ | Cutting force | Experimental (dynamometer) | N |
| $F_f$ | Feed force | Experimental (dynamometer) | N |
| $F_r$ | Radial force | Experimental (dynamometer) | N |
| $F_{xy}$ | Resultant of feed force and radial force | $\sqrt{(F_f^2 + F_r^2}$ | N |
| $F_t$ | Shear force | $F_c cos\emptyset - F_{xy} sin\emptyset$ | N |
| $F$ | Friction force | $F_c sin \propto + F_{xy} cos \propto$ | N |
| $N$ | Normal to Friction force | $F_c cos \propto - F_{xy} sin \propto$ | N |
| $V$ | Cutting velocity | Input Cutting Parameter | cm/s |
| $V_c$ | Chip velocity | $\frac{V_c\ sin\emptyset}{\cos(\emptyset - \propto)}$ | cm/s |
| $V_s$ | Shear velocity | $\frac{V_c\ cos \propto}{\cos(\emptyset - \propto)}$ | cm/s |
| $L$ | Length of shear plane | $t_c/sin\emptyset$ or ${}^{t_{chip}}\!/_{cos(\emptyset - \alpha)}$ | cm |
| $\beta$ | Friction angle | $\tan^{-1} {}^{F}\!/_{N}$ | $^{\circ}$ |
| $l$ | Tool chip contact length | $\frac{t_c \sin(\emptyset + \beta - \alpha)}{sin\emptyset\ cos\beta}$ | cm |
| $k$ | Thermal conductivity of chip | Data book | J/cms$^{\circ}$C |
| $a$ | Thermal diffusivity of chip | Data book | cm$^2$/s |
| $q_s$ | Heat intensity of the primary heat source | $\frac{F_s V_s}{L_{AB} w}$ | J/cm$^2$s |
| $q_{se}$ | Heat intensity of the secondary heat | $\frac{F V_{chip}}{lw}$ | J/cm$^2$s |
| $B_c$, $\Delta B$, $C$, $m$, & $n$ | Constants | Komanduri & Hou [3] functional analysis | -- |

JJMIE

Volume 9 Number 2, April.2015
ISSN 1995-6665
Pages 113 - 120

Jordan Journal of Mechanical and Industrial Engineering

# Estimation of Defect Severity in Rolling Element Bearings using Vibration Signals with Artificial Neural Network

Vana Vital Rao[*] [a], Chanamala Ratnam[b]

[a] Sr. Manager, Engineering Shops Department, Visakhapatnam Steel Plant, A.P., INDIA,
[b] Professor, Department of Mechanical Engineering, AU College of Engg., Andhra University,Andhra Pradesh. INDIA

Received 4 April 2014 Accepted 2 April 2015

**Abstract**

In condition monitoring of rotating machinery, vibration analysis is a popularly used diagnostic tool for checking the health of rolling element bearings. The vibration signal caused by bearing defects will always be contaminated and distorted by other faults and mechanical noise particularly in hostile environment. Vibration based methods are effective when the defect in the bearings has already become severe. A bearing test rig was designed and setup in a workshop to study the vibration analysis of various faults in rolling element bearings. In the literature, it was observed that researchers studied different types of seeded defects, but these defects are random in size and shape; hence the correlation between defect size and its vibration parameter is not established. In this investigation, test runs conducted with seeded defects of same type with a gradual increase of its size on outer race of radially loaded cylindrical roller bearings at different speeds and loads. Vibration data were acquired by accelerometer and processed through Fast Fouier Transform (FFT). From the data, it was found that the vibration root mean square (rms) velocity increases significantly with the increase of defect size and speed, but not with the load. Artificial Neural Networks (ANN) multilayer perception model with back-propagation algorithm was used, with input parameters of Load, Revolutions Per Minute (RPM) and vibration rms velocity and output is seeded defect size. The ANN was trained with data sets of number of test runs conducted and predicted the defect size. The predicted values were compared with the actual seeded defect size and found the error was approximately 3.90%. In this investigation, an attempt was made to predict the defect size of a specific bearing with respect to its vibration rms velocity for given conditions. This study may be useful for the monitoring of critical bearings in the industry.



**Keywords:** *Roller Bearings, Fault Detection, Defect Size , Vibrations and ANN.*

## 1. Introduction

Since structural failures in engineering field can lead to severe economic loss, structural health monitoring is essential particularly in aerospace, civil and other structures. Precise incipient structural damage identification and its location are of great interest to many researchers [1-5]. In rotating machinery, early fault detection of the rolling elements, i.e., bearing and gear faults has also been gaining importance in recent years because of its detrimental influence on the reliability of equipment. Different techniques have been developed for monitoring and diagnosis of rolling element bearings [6]. Most of the developed methods are based on vibration signals and its analysis. Vibration based methods are effective when the defect in the bearings becomes severe. Detection of the fault and its severity are two important steps or features of a condition monitoring system. The lifetime of a machine component is determined by the severity of the fault. It is crucial, especially in critical systems, where continual operation is generally indispensable. The bearing defects three types, distributed, localized and the combination of both. The distributed defects can be the surface roughness, waviness, misaligned races, and off-size rolling elements. Localized defects are developed in the raceways, rollers and cage of a bearing. The periodic impacts occur at ball-passing frequency (characteristic defect frequencies), which can be calculated from the bearing geometry and the rotational speed [7]. In vibration analysis of bearings, these defect frequencies are not observable in some cases with the help of the Fast Fourier Transform (FFT) frequency spectra, because the impulses generated by the defects are masked by mechanical noise and distorted by other faults. The vibration signal is not sensitive to the incipient defect. To overcome this problem, signal processing techniques are implemented by many researchers to detect incipient bearing local faults [8]. In this investigation, experiments are planned in a systematic way with different speed, load

[*] Corresponding author. e-mail: vvrao_vana@yahoo.co.in.

and gradual increase of defect size. The vibration signal is captured by accelerometer and processed with CSI vibration analysis software. A multi-layer perception neural network is selected and trained with the experimental data and tested to predict the approximate defect size of a damaged bearing.

## 2. Artificial Neural Networks (ANN)

Artificial Neural Networks (ANN) have been developed as generalizations of mathematical models of biological nervous systems. ANN is also kown as parallel distributed processing system. The network is referred to as a directed graph having a set of neurons (nodes) and set of connections (weights) between nodes. Each node contributes some kind of function like simple computation and each connection transfers information or signal between nodes. Each connection between two nodes is labeled with a number called the connection strength or weight. The weight represents the extent the signal is to be amplified or diminished by the connection [9].

The network with a single node or fewer nodes cannot solve all the problems, and the networks, which are constructed with large number of nodes, are used to solve complex problems. Some of the networks are fully connected networks, layered networks, feed forward networks. Different types of learning methods are used in ANN such as supervised learning, unsupervised learning and reinforcement learning [10]. The behavior of the network changes according to the changes in the weights of connections in the network. The changes in the weights of ANN are referred to as learning which effects the synaptic efficiencies in real ANN. Neural networks are well established and prominent in literature [11]. A neural network with back propagation supervised learning process is important and used in various applications like classification, prediction or forecasting and approximation.

Jigar patel *et al.* studied the damage identification of rolling bearings based on improved time and frequency domain features using neural networks and they successfully diagnosed up to 98% of fault cases [12]. Mahmuod Akbari *et al.* used discrete wavelets transforms along with ANN in fault diagnosis of gears and bearings in a gear box and achieved high success rate [13]. Bahaa Ibraheem implemented neural network model to optimize the turning process parameters for controlling the vibration levels in turning [14]. M. Samhouri *et al.* applied an Adaptive Neuro-Fuzzy Inference System (ANFIS) and neural networks system in machine condition monitoring and proved neural networks achieved 99% fault prediction accuracy [15].

## 3. Bearing Kinematics

When the ball or roller comes across the fault while bearing is running, the rotation of roller momentarily stops due to the impact of hitting the edge of the fault. The reaction of the force from the fault edge opposes the rotation of the roller. When a rolling element encounters a fault, a rapid localized change in the elastic deformation of the elements takes place, and a transit force imbalance occurs. A faulty rolling bearing produces certain defect frequencies depending on the rolling element bearing geometry. When the outer race is stationary, the mathematical expressions to evaluate the defect frequencies can be written as follows:

Fundamental Train Frequency,

$$FTF = \frac{1}{2}(f_i)\left[1 - \frac{d\cos\theta}{D_p}\right]$$

Ball Pass Frequency of the Outer race,

$$BPFO = \frac{N}{2}(f_i)\left[1 - \frac{d\cos\theta}{D_p}\right]$$

Ball Pass Frequency of the Inner race,

$$BPFI = \frac{N}{2}(f_i)\left[1 + \frac{d\cos\theta}{D_p}\right]$$

Ball Spin Frequency,

$$BSF = \frac{D_p}{2d}(f_i)\left[1 - \left(\frac{d\cos\theta}{D_p}\right)^2\right]$$

where $D_p$ - Pitch circle diameter, $\theta$ - contact angle, $f_i$ - Rotation frequency of inner race,

$N$ - Number of rolling elements and $d$ - diameter of rolling element.

In machinery which is running with normal speeds, these defect frequencies lie in a low frequency range up to 1000Hz. These calculated frequencies may be slightly varied from the actual values in practice due to slipping or skidding in rolling element bearings [16]. Some researchers [17] mentioned that it is difficult to obtain a significant peak at these defect frequencies in the vibration frequency spectra from a defective bearing. This is due to the noise and vibrations from other sources which mask the vibration signal from the defective bearing unless the defect is sufficiently large.

## 4. Experimental Test Set Up

Figure 1 is the schematic diagram, representing the bearing test facility and is designed to fulfill the requirements of current investigation and future research in this area. The testing involves the mounting and running of the test bearings with various sizes of seeded defects, under specific parameters of speed and load, vibration signal data acquisition through accelerometer.

The test rig (Figures 2 & 3) consists of six major parts, i.e. shaft, support bearings with plumber blocks, bearing block with test bearing, 2.2 KW-3 phase induction motor, 4 KW variable frequency drive for speed control, and a vertical hydraulic ram for applying load radially. The test set up operational speed range is up to 2800 rpm with a maximum load 16 kN via a hydraulic ram. The shaft is made up of En 18 steel; the V-pulley at one end and the test bearing at the other, and in between two support bearings with plumber blocks assembled on the shaft. Deep groove ball bearings (SKF 6212 RS2) are used as support bearings. The motor connected the shaft via a V-belt. The motor is mounted on a separate base frame to avoid transfer of vibrations of motor to test rig. The test bearing block is a square split housing and made up of with EN 24 steel. On the top of housing vibration accelerometer and hydraulic ram placed while conducting test run.

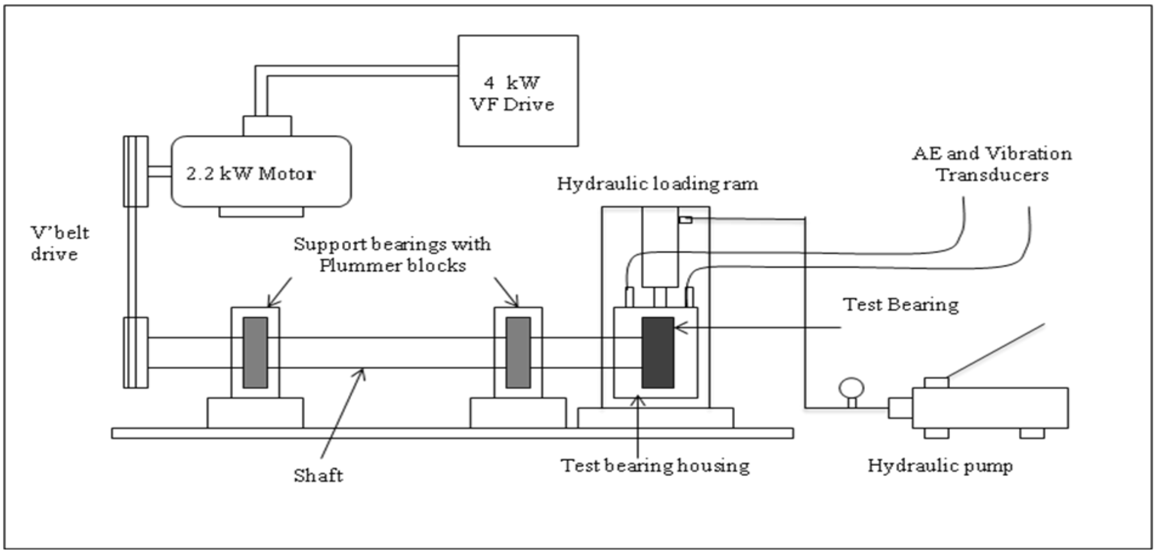


**Figure 1**. Experimental test setup schematic

**Figure 2.** Bearing Test Rig

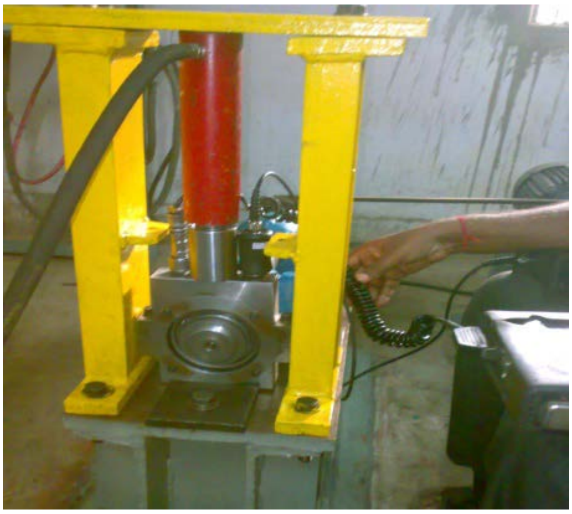

**Figure 3.** Test bearing with Probes

## 5. Test Bearing Specification

In this investigation, N312 type cylindrical roller bearing with normal clearance is considered (Figure 4). The reason behind selecting this bearing is that the defects can be created in the outer race easily as it allows easy dismantling and assembly of the outer race. The geometric details of the test bearing are as follows: Inner diameter- 60mm, Outer diameter- 130mm, Width- 33mm, Number of rollers- 12, Rolling element diameter- 18mm, Pitch circle diameter ($D_p$ )- 96mm, Contact angle ($\theta$)- $0^{\circ}$.

**Figure 4.** N312 cylindrical roller bearing

The bearing characteristic defect frequencies are calculated from the dimensional parameters of N312 cylindrical roller bearing and shown in Table 1.

**Table 1.** Theoretical Characteristic Defect frequencies in CPM (cycles per minute) at different RPM

| | RPM → | 900 | 1100 | 1300 | 1500 |
|---|---|---|---|---|---|
| Defect frequency in CPM | FTF | 365.4 | 447.0 | 528.0 | 603.6 |
| | BSF | 2315.4 | 2829.6 | 3345.6 | 3859.2 |
| | BPFI | 6412.8 | 7836.0 | 9264.0 | 10687.8 |
| | BPFO | 4387.8 | 5361.6 | 6338.4 | 7312.8 |

## 6. Experimental Procedure

A total of five test bearings was used in this investigation. In previous studies, artificial damages were induced in bearings via several ways: scratching/engraving the surface with diamond scriber, introducing debris into the lubricant and electrical spark erosion, etc. In this investigation, defects introduced by wire cut EDM (Electro Discharge Machining) for a better accuracy. The defects were seeded in various sizes of width 0.3, 0.5, 0.7 and 0.9 mm. Depth of defect 0.3mm is maintained in all test bearings. Figure 5 shows 0.5mm width defect on bearing outer race.

**Figure 5.** Outer race seeded defect (0.5mm width)

Numbers of test runs were conducted on test rig for the consistency check of the data captured. On the first instance, a good test bearing without defect assembled to conduct a test run and was left for several hours for stabilizing and for minor adjustments of the test rig. After that, a test bearing with 0.3 mm size defect was seeded on outer race bearing assembled and the defect place(d at the top in the test bearing housing where the load was applied radially through hydraulic ram. The CSI 2120 model vibration analyzer was used for data acquisition. The same procedure was used in test runs on other bearings with different defect sizes on outer races. All the test runs were conducted at two loads in 2kN and 4kN at different speeds varying from 900 to 1500 RPM in four steps. All the speeds were adjusted with the Variable Frequency (VF) drive. The vibration signal is processed through FFT with the CSI vibration analyzer software. Time waves and frequency spectra for all the test runs were analyzed in detail for a comparative study.

A total of 32 different experiments was planned, as per the matrix (4 speeds, 4 defect sizes and 2 load conditions). It was planned to conduct many test runs for each experiment for the consistency of the measurement.

## 7. Results and Discussion

Out of the 32 experiments, in some experiments the consistency of data measurement was observed within two test runs; but for some other experiments three to four test runs were conducted. A total of 71 test runs were conducted.

In Table 2, the vibration rms velocity values were furnished for all the 32 experiments with the same parameters at different defect sizes. In this investigation, the seeded defect sizes were provided in a gradual increasing manner to observe the variation in vibration rms velocity with respective to defect size. The vibration rms velocity increases significantly with the increase of the defect size and speed, but not in the case of load.

**Table 2.** Vibration rms velocity in (mm/sec) at various defect sizes, RPM and Load

| 2kN load | | | | | | 4kN load | | | |
|---|---|---|---|---|---|---|---|---|---|
| RPM | Defect size (width) in mm | | | | | Defect size (width) in mm | | | |
| | 0.30 | 0.5 | 0.7 | 0.9 | | 0.30 | 0.5 | 0.7 | 0.9 |
| 900 | 1.08 | 1.20 | 1.64 | 1.60 | | 1.18 | 1.28 | 1.49 | 1.70 |
| 1100 | 1.38 | 1.53 | 2.01 | 2.27 | | 1.38 | 1.72 | 1.78 | 2.13 |
| 1300 | 1.57 | 1.66 | 2.27 | 2.45 | | 1.84 | 2.11 | 2.40 | 2.66 |
| 1500 | 2.01 | 2.01 | 2.90 | 2.97 | | 2.09 | 2.43 | 2.70 | 3.02 |

Figure 6 shows the vibration time wave and the frequency spectrum of the test run conducted with the outer race defective bearing. A peak observed at 7312.8 CPM, ball pass outer race frequency (BPFO); some other significant peaks were also observed, but they were not related to the bearing characteristic defect frequencies.

Figure 7 shows comparative frequency spectrums of 0.5, 0.7 & 0.9 mm defects, 4kN load, and the test runs conducted at 1500RPM. It was observed that, as the defect size increased and other running conditions were the same, the peak at BPFO had an increasing trend.

Figure 8 shows Vibration root mean square (Vib.rms) velocity versus RPM for different defect sizes at 4kN load. The graph shows that the Vib.rms velocity increases with the increase of defect size and RPM.

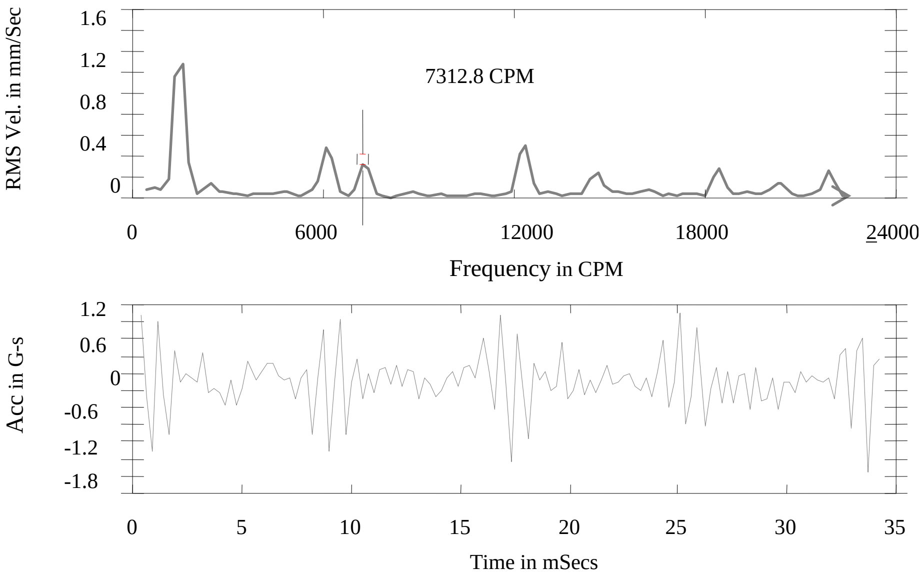


**Figure 6**. Time wave & Frequency spectrum with 0.7mm defect, 4kN load, 1500 RPM

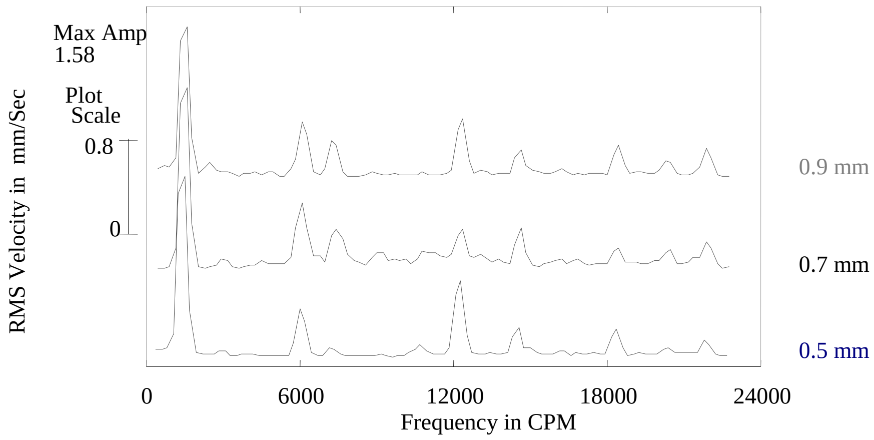


**Figure 7.** Frequency spectrums of 0.5, 0.7 & 0.9 mm defects, 4kN load, 1500 RPM

 

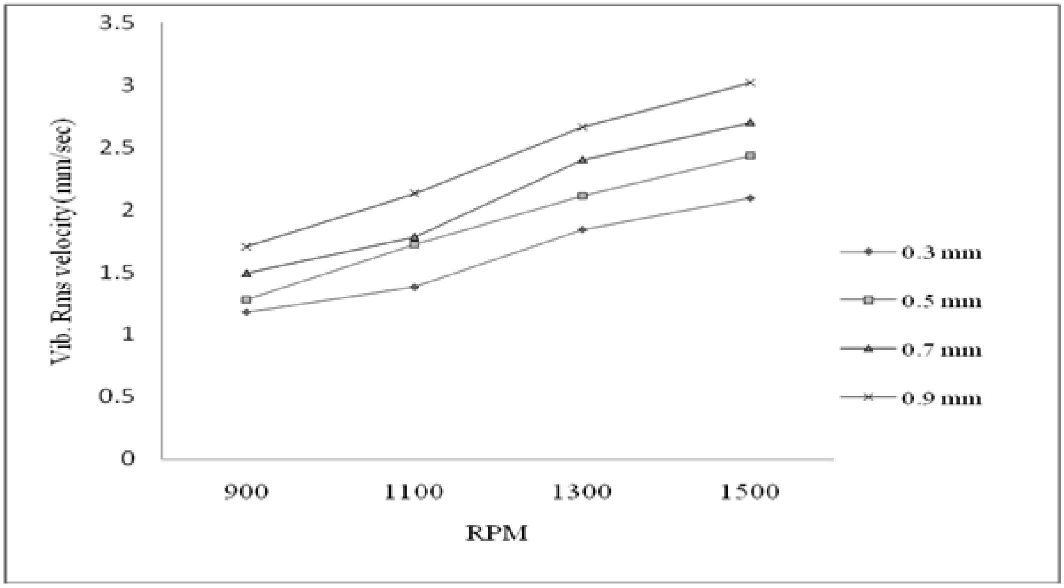


**Figure 8**. Vib.rms velocity (mm/sec) at different defect sizes and RPM at 4kN load

A feed-forward back propagation neural network is constructed with four layers including input, output and two hidden layers (Figure 9). The ANN with one hidden layer gave significantly high errors. Hence, a two-layer network was considered. The input neurons were load, RPM and Vibration rms velocity whereas the output neuron was defect size. Neurons, in the hidden layers, were determined by examining different neural networks. An easy Neural Networks (NN) plus software is used for training this network with back propagation algorithm (Figure 10). Weights of network connections were randomly selected by the software itself.

As per ref. [18], the advantage of the usage of neural networks for prediction is that they are able to learn from examples only, and that after their learning is accomplished, they can recognize hidden and strong non-linear dependencies, even when there is a significant noise in the training set. When input data are adjusted to designate shape, it is divided into three sets; a training set (learning), a validation set and a testing set. The default setting of the ratio, as per statistical program, is: 70% of the input data is a training set, 15% a validation set and 15% a testing set. To sum up, the training set is used for creating a model, the validation set for verifying the model, and the testing set for testing the usability of the model.

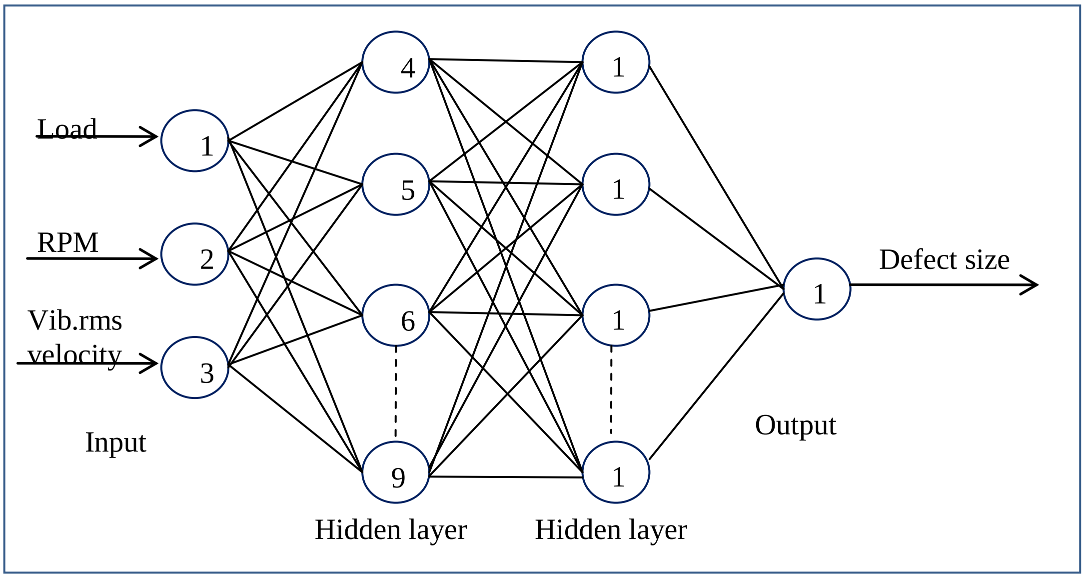


**Figure 9.** Neural network architecture

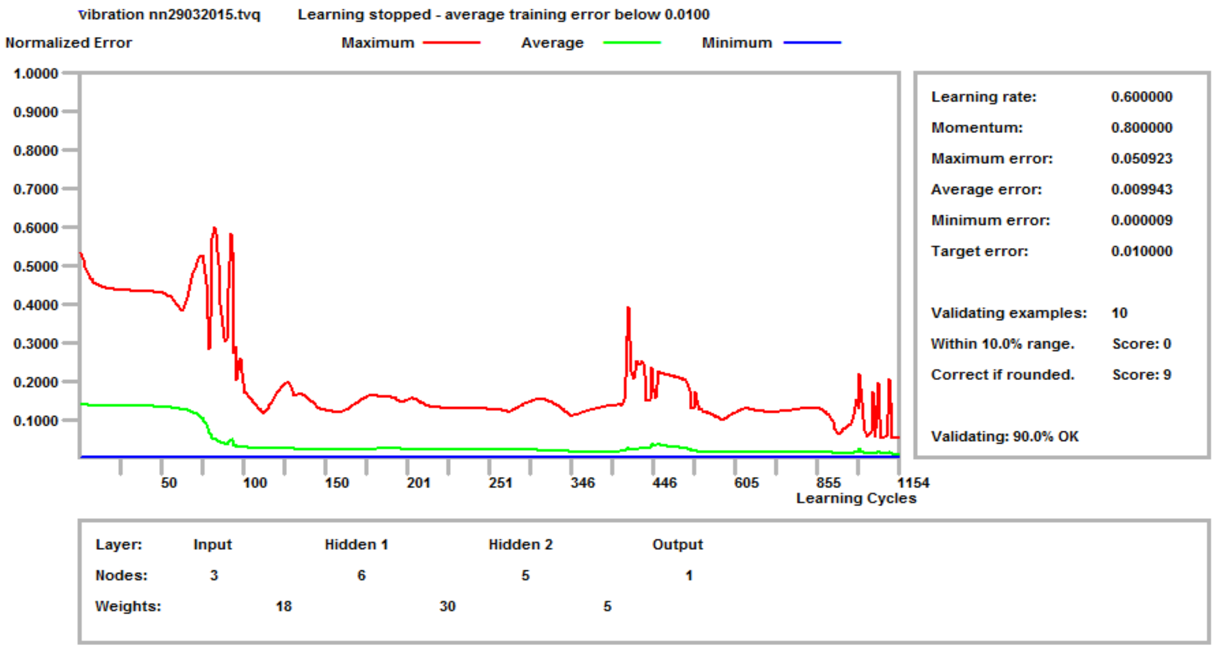


**Figure 10**. Learning progress graph with maximum, average and minimum training error.

Out of the 71 test runs data, the neural network was trained with 51 data sets, validated with 10 data sets and tested for 10 data sets, which were selected in a random manner. Predicted values of the defect size through testing are given in the Table 3. The percentage of the error between the actual defect size and the predicted values are calculated. The mean error percentage was found as 3.75% of defect size.

From the Table 3, it is found that the predicted values are very close to the experimental values. From these results, it can be deemed that the proposed network model is capable of predicting the defect size

The graph, shown in Figure 11, gives a comparison between the actual defect size and the predicted defect size for all the 71 sets of data. According to the values obtained, the overall calculated average error was 4.83%

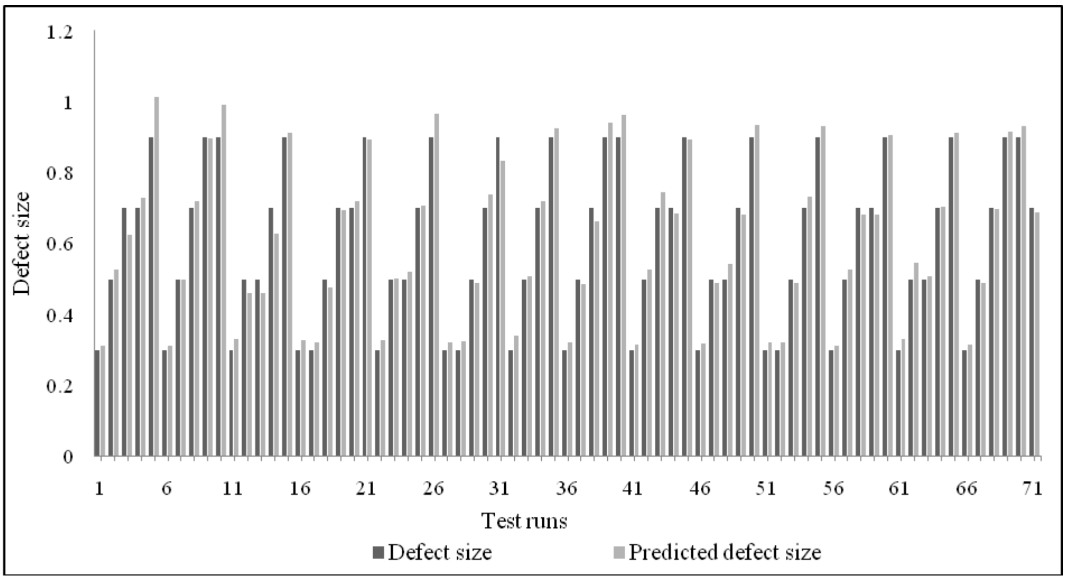


**Figure 11.** Comparision of actual verses predicted defect sizes for all test runs

.

**Table 3**. Experimental results and its predicted values of defect size in testing

| Exp. No | Load (kN) | RPM | Vib. rms velocity (mm/sec) | Defect size in (mm) | Predicted Defect size in (mm) | % error |
|---|---|---|---|---|---|---|
| 1 | 2 | 900 | 1.20 | 0.5 | 0.485 | 2.82 |
| 2 | 2 | 900 | 1.60 | 0.9 | 0.892 | 0.82 |
| 3 | 2 | 1100 | 1.78 | 0.7 | 0.708 | 1.15 |
| 4 | 2 | 1300 | 1.57 | 0.3 | 0.317 | 5.70 |
| 5 | 2 | 1500 | 2.01 | 0.3 | 0.324 | 8.26 |
| 6 | 4 | 900 | 1.70 | 0.9 | 0.932 | 3.57 |
| 7 | 4 | 1100 | 1.72 | 0.5 | 0.526 | 5.26 |
| 8 | 4 | 1300 | 1.84 | 0.3 | 0.291 | 3.00 |
| 9 | 4 | 1300 | 2.40 | 0.7 | 0.734 | 4.98 |
| 10 | 4 | 1500 | 3.02 | 0.9 | 0.917 | 1.84 |
| Average error : 3.75 | | | | | | |

## 8. Conclusions

In the present work, 71 test runs are conducted for planned 32 experiments with four levels of speed, defect size and two levels of load. A feed-forward four layered back propagation neural network (3-6-5-1) was used to train the collected experimental data. The ANN was trained with 51 data sets, validated with 10 data sets and tested for 10 data sets taken from the total test runs. The trained ANN was used to predict the defect size. It is found that there is an agreement between the experimental data and the predicted values for the defect size is (3.75% of error). With this ANN model, it is possible to monitor the condition of the bearings of important equipment in the industry to predict the severity of defect size, which will help in proper maintenance action to avoid the sudden failure of the equipment.

Hence, from these experimental investigations, it is revealed that the vibration data along with ANN model give a better analysis to diagnose the defect size of a particular bearing.

## References

[1] E.P. Carden, P. Fanning, “Vibration based condition monitoring: a review”. Structural Health Monitoring, Vol. 3 (2004) No. 4, 355 - 377.

[2] P. Srinivasa Rao, Ch. Ratnam, “Damage Identification of Welded Structures Using Time Series Models and Exponentially Weighted Moving Average Control Charts”, Jordan Journal of Mechanical and Industrial Engineering, Vol. 4(2010), No.6, 701 – 710.

[3] Ch. Ratnam, B.S. Ben,“Structural damage detection using combined finite element and model lamb wave propagation parameters”, Journal of mechanical science, Vol. 223 (2009), 769 - 777.

[4] P. Srinivasa Rao, Ch. Ratnam, “Vibration based damage identification using Burg’s algorithm and Stewart control charts”, Journal of ASTM International, Vol.8 (2011), No.4.

[5] W.Fan and P. Qiao, “Vibration-based damage Identification Methods: A Review and Comparative Study” Structural Health Monitoring, Vol. 10 (2011), No. 1, 83-111.

[6] Abdullah M and Al-Ghamd and D .Mba “A comparative experimental study on the use of acoustic emission and vibrational analysis for bearing defect identification and estimation of defect size” Mechanical systems and Signal processing, 20(2006), 1537-1571.

[7] P. D. McFadden, J. D. Smith ,”Vibration monitoring of rolling element bearings by the high-frequency resonance technique- a review”, Tribology International, 17(1):3(10), 1984.

[8] Lab VIEW, Advance Digital Signal Processing User Manual, Austin (2007).

[9] S.Rajasekharan and G.A.Vijayalakshmi pai “ Neural networks, Fuzzy logic and Genetic algorithms” New delhi, Prentice Hall of India; 2004.

[10] Colin Fyfe, Artificial Neural Networks and Information Theory”, 2nd Edition Scotland; 2000.

[11] W. Sha W, K. L. Edwards, “The use of artificial neural networks in materials science .based research”. Mater. Des, 28 (2007), No. 6, 1747-1752.

[12] Dr.Jigar Patel, Vaishali Patel and Amit Patel, ‘Fault Diagnostics of Rolling Bearing based on Improve Time and Frequency Domain Features using Artificial Neural Networks” International Journal for Scientific research & development, Vol.1(2013), Issue-4, 781-788.

[13] Mahmuod Akbari, Hadi Homaei and Mohammad Heidari, “An Intelligent Fault Diagnosis approach for Gears and Bearings Based on Wavelet Transform as a Preprocessor and Artificial Neural Networks” International Journal of Mathematical Modeling & Computations Vol. 04(2014), No. 04, 309- 329.

[14] Bahaa Ibraheem Kazem, Nihad F. H. Zangana, “A Neural Network Based Real Time Controller for Turning Process”, Jordan Journal of Mechanical and Industrial Engineering, Vol. 1(2007), No.1, 43-55.

[15] M. Samhouri, A. Al-Ghandoor, S. Alhaj Ali, I. Hinti, W. Massad, “An Intelligent Machine Condition Monitoring System Using Time-Based Analysis: Neuro-Fuzzy Versus Neural Network” Jordan Journal of Mechanical and Industrial Engineering, Vol. 3(2009), No.4, 294-305.

[16] Sharad Jain,”Skidding and Fault Detection in the Bearings of Wind-Turbine Gearboxes” P.hd thesis, Churchill College, Cambridge, UK ,December 2012.

[17] A. B. Johnson, A. F. Stronach, “Bearing fault detection in hostile environment”. I Proceedings of International Conference on Condition Monitoring, Brighton, UK, 21-23 May (1986), 35-44.

[18] Ondrej Krejcar, “Utilization of C# Neural Networks library in Industry applications” E-Technologies and Networks for Development, First international conference proceedings, ICeND ,Dar-es-Salaam, Tanzania, August 3-5,( 2011) ,61-70

JJMIE

Volume 9 Number 2, April.2015
ISSN 1995-6665
Pages 121 - 128

Jordan Journal of Mechanical and Industrial Engineering

# Corrosion Characteristics of Basalt Short Fiber Reinforced with Al-7075 Metal Matrix Composites

Ezhil Vannan * a, Paul Vizhian b

[a] *Professor, Department of Mechanical Engineering, H.K.B.K College of Engineering, Nagawara, Visvesvaraya Technological University, Bangalore, India.*
[b] *Professor, Department of Mechanical Engineering, University Visveswarya College of Engineering,K.R. Circle, Bangalore University, Bangalore, India*

*Received 17 June 2014* *Accepted 22 March 2015*

**Abstract**

This paper reports a study of the corrosion characteristics of Al 7075/ basalt short fiber metal matrix composites in 1 M HCl solution at room temperature as a function of percentage of reinforcement. The percentage of reinforcement was varied from 2.5 to 10 wt.% in steps of 2.5% and the composites were prepared by the liquid metallurgy technique. The weight loss method was used to determine the corrosion rate. The durations of the tests ranged from 24 to 96 hrs in the steps of 24 hrs. Both the unreinforced matrix alloy and the composites were subjected to identical test conditions to study the influence of the reinforcement on Al 7075/ basalt corrosion behavior. The corrosion rates of both the unreinforced matrix alloy and the composites decreased with the exposure time. The corrosion rate of MMCs was lower than that of matrix Al 7075 alloy under the corrosive atmosphere. Scanning Electron Microscopy (SEM) was used to study the corroded surface of the specimens.



**Keywords:** *Metal Matrix Composite; Aluminium Alloy, Basalt Fiber; Corrosion*.

## 1. Introduction

In the recent years, there has been a great interest in searching for new materials, which offers designer many added benefits in designing the components for automobile and aircraft industry through Metal Matrix Composites (MMCs). Aluminium based MMCs offer designers many added benefits, as they are particularly suited for applications requiring good strength at high temperatures, good structural rigidity, dimensional stability, and lightweight [1-4]. The trend is toward safe usage of the MMCs parts in the automobile engine, particularly at high temperature and pressure environments [5, 6]. Fiber reinforced MMCs that have been most popular over the last two decades have attracted considerable attentions [7-10]. Fiber reinforced MMCs find their utilization in the rapidly broadening field of application. They have been widely used in many industries such as aircraft, aerospace, automobiles, ships and civil constructions. These materials maintain good strength at high temperature, good structural rigidity, dimensional stability and light weight [11-13]. Reinforced Al MMCs find Potential applications in several thermal environments, especially in the automobile engine parts, such as drive shafts, cylinders, pistons, and brake rotors. Al-based MMCs which are used in automobile engine parts normally encounter acidic environments containing chloride, sulphiate and nitrate radicals, in addition to exhaust gases like $CO_2$, CO and $NO_2$. MMCs used at high temperatures should have good mechanical properties and resistance to chemical degradation in air and acidic environments [14]. High strength aluminum alloys, such as 7075, are widely used in aircraft structures, aerospace and automobiles due to their high strength-to-weight ratio, machinability, superior wear resistance, improved elevated temperatures tensile and fatigue strengths and low cost. However, due to their compositions, these alloys are susceptible to corrosion. Corrosion is a major concern involving the structural integrity of aircraft structures and automobile components. Considerable attention is focused on aluminum based metal matrix reinforced with high strength and high modulus ceramic reinforcements because of their superior properties [15, 16]. For high temperature applications, it is essential to have a thorough understanding of the corrosion behavior of the aluminium composites. Reported literature [17–19] indicates that the addition of SiC particles do not appear to improve corrosion resistance of some aluminium alloys because pits were found to be more numerous on the composites than on the unreinforced alloys although they were comparatively smaller and shallower than those on the unreinforced alloy.

* Corresponding author. e-mail: ezhilsil@yahoo.co.in.

As far as we know, although many researchers have worked on corrosion characteristics of fiber reinforced metal matrix composites, no concrete investigation has been made on basalt fiber reinforced with aluminum alloy 7075 metal matrix composites. The present paper focuses on the corrosion characteristics of Al 7075/ basalt short fiber metal matrix composites.

## 2. Materials and Methods

### *2.1. Materials*

The Al and basalt short fiber used as the MMCs in the present study are obtained from commercial ingots with correct chemical composition. The presence of these elements have been confirmed by SEM / EDS spectra. The Energy Dispersive Spectroscopy [EDS] spectrum also shows the presence of impurities such as iron and basalt short fiber in traces. The alloy is found to be pollution free in the foundry. Because of its low energy requirements and excellent machinability, it is expected to reduce the production time and lengthen tool life during its fabrication process. The matrix alloy used in the present investigation was Al 7075 alloy, which has basalt short fiber reinforcement; the chemical composition is shown in Tables 1 and 2 [20].

**Table 1.** Chemical composition of Al alloy- Weight percentage

| Element | Si | Fe | Cu | Mn | Mg | Cr | Zn | Ti | Al |
|---|---|---|---|---|---|---|---|---|---|
| % | 0.4 | 0.5 | 1.6 | 0.3 | 2.5 | 0.15 | 5.5 | 0.2 | Bal |

**Table 2.** Properties of matrix alloy

| | |
|---|---|
| Density | 2.7 gm/cc |
| Young's modulus | 75 GPa |
| UTS | 170 MPa |
| Ductility | 13.5 % |
| Melting temperature | 650° C |

### *2.2. Reinforcement*

The basalt fiber was made from naturally occurring basalt rock in the Washington State area, USA. The basalt short fiber, used as reinforcement in the present investigation, has been purchased from a mineralogical research company. The chemical composition of the fibers is determined by the native basalt rock used as a raw material, whose main composition is shown in Table 3 [21].

**Table 3.** Chemical composition of short basalt fiber

| Element | $SiO_2$ | $Al_2O_3$ | $Fe_2O_3$ | MgO | CaO | $Na_2O$ | $K_2O$ | $TiO_2$ | MnO |
|---|---|---|---|---|---|---|---|---|---|
| % | 69.51 | 14.18 | 3.92 | 2.41 | 5.62 | 2.74 | 1.01 | 0.55 | .04 |

The fiber was produced in a prototype device. The basalt rock was melted in a platinum-rhodium crucible at 1250±1350°C. The fiber was drawn from the melt through a fiber in the crucible and wound onto a rotating drum continuously. Fibers in roving form were bundled and cut into short fibers of uniform length about 0.5 to1 mm in size by constant-length cutter. The short Basalt short fiber was cleaned in distilled water and dried at 90°C.

### *2.3. Composite Preparation*

The liquid metallurgy route using vortex techniqueis employed to prepare the composites. The weight percentage of the basalt short fiber added was 2.5, 5, 7.5 and 10% to prepare the MMCs. A muffle furnace was used to preheat the copper coated basalt short fiber to a temperature of 500°C and maintained at that temperature till it was introduced into the Al alloying elements melt. The preheating of the reinforcement is necessary in order to reduce the temperature gradient and to improve wetting between the molten metal and the basal short fiber. Known quantities of these metals ingots were pickled in 10% NaOH solution at room temperature for ten minutes. Pickling was done to remove the surface impurities. The smut formed was removed by immersing the ingots for one minute in a mixture of 1:1 volume/volume of nitric acid and water followed by washing in methanol. These cleaned ingots after drying in the air were loaded into different alumina crucibles. These crucibles kept in composites furnace, which were setting metals respected melting temperature. The melts were super-heated and maintained at that temperature. The temperatures were recorded using a chromel-alumel thermocouple. The molten metals were then degassed using purified nitrogen gas. The purification process with commercially pure nitrogen was carried out by passing the gas through an assembly of chemicals arranged in a row (concentrated sulphuric acid and anhydrous calcium chloride, etc.) at the rate of 1000 cc/ minute for about 8 minutes. A stainless steel impeller or stirrer coated with alumina was used to stir the molten metal and create a vortex. The impeller used for stirring was of centrifugal type with three blades welded at 45° inclination and 120° apart. The stirrer was rotated at a speed of 500 rpm and a vortex was created in the melt. The depth of immersion of the impeller was approximately one third the height of the molten metal above the bottom of the crucible. The reinforcing basalt short fiber, which was preheated in the muffle furnace, was introduced into the vortex at the rate of 120 gm/min. Stirring was continued until interface interactions between the basalt short fiber and the matrix promoted wetting. Then the melt was degassed using pure nitrogen for about 3-4 minutes and after reheating to super heat temperature (540°C), it was poured into the pre heated lower half die of the hydraulic press. The top die was brought down to solidify the composite by applying a pressure of 100 kg/sq.cm. Both the lower die and the upper dies were preheated to 280°C, before the melt was poured into it. The pressure applied enables uniform distribution of the basalt short fiber in the developed composite [22].

### *2.4. Specimen Preparation*

Cylindrical specimens of diameter 15mm and thickness 5mm were machined from castings of the composites and of the unreinforced alloy using an abrasive cutting wheel. Before corrosion testing, the specimen surfaces were ground using 240, 320, 400 and 600 SiC paper, in this order, using distilled water as a lubricant and a coolant in order to obtain a smooth and identical surface finish on all the specimens [23]. The specimen were then washed in distilled water, followed by acetone, and then allowed to dry thoroughly [24]. Before corrosion testing, each test specimen was etched with killer's agent and examined under optimal microscope. They were finally weighed to an accuracy of three decimal places. This same cleaning procedure was used before each weighing at each stage of the corrosion test.

### 2.5. Corrosion Test

The corrosion test was conducted at room temperature (27°C) using conventional corrosion rate measurement according to ASTM G1-03 and ASTM G31-72 [25, 26]. The area of the specimen, subjected to corrosion, was calculated before performing corrosion test using the following equation (according to ASTM G31–72):

$$A = (\pi / 2(D^2 - d^2)) + t\pi D + t\pi d, \quad (1)$$

where $t$ is thickness, $D$ is diameter of the specimen, and $d$ is diameter of the mounting hole. The corrodents used for the tests were 1M hydrochloric acid. Small cylindrical discs of 15mm diameter and 5mm thickness were polished using emery paper in order to obtain a smooth and identical surface finish on all specimens, and then washed in distilled water, followed by acetone, and then allowed to dry thoroughly [27]. They were finally weighed accurately to an accuracy of three decimal digits. The initially weighted specimens were immersed in the corrosive environment and taken out at 24 h intervals for testing up to 96 hr. To avoid crevice corrosion, the specimens were suspended in the solution with a plastic string. The specimens were exposed to the test solution for several hours up to 96 hr. The corroded surface was removed by immersing the specimen on 100 mg ammonium per sulphate for 5 min. The cleaned specimens were dried and weighed to an accuracy of three decimal digits. After drying thoroughly, the specimens was weighed again and then placed in a dessicator to prevent corrosion. Weight loss was calculated and converted into corrosion rate and expressed in mils penetration per year (myp). The corrosion rate was calculated and compared with other reinforcements. The Corrosion Rate (CR), from the mass loss, was calculated (according to ASTM Standard [28, 29] using the following equation:

$$CR = (K \times W) / A \times T \times D) \quad (2)$$

where CR is corrosion rate (mm/year), $K$ is a constant equal to $8.76 \times 10^4$, $T$ is time of exposure in hours to the nearest 0.01 hour, $A$ is area in $cm^2$, $W$is mass loss in grams, and $D$ is density in $g/cm^3$. The microstructure was examined using CETI optical microscope and the corroded surface was studied using SEM Model Quanta FEG 250. Tables 4 and 5 show the average corrosion rates of Al7075 as well as Al7075/basalt fiber MMCs; the average is of 10 samples.

**Table 4.** The average corrosion rates of Al7075

| Exposure duration (hr) | Area of specimen ($mm^2$) | Average corrosion rate (mm/year) |
|---|---|---|
| 24 | 274.89 | 0.08 |
| 48 | 274.89 | 0.045 |
| 72 | 274.89 | 0.032 |
| 96 | 274.89 | 0.024 |

**Table 5.** The average corrosion rates of Al7075/Basalt fiber MMCs

| Basalt fiber (Wt. %) | Exposure duration (hr) | Average corrosion rate (mm/year) |
|---|---|---|
| 2.5 | 24 | 0.096 |
| | 48 | 0.054 |
| | 72 | 0.038 |
| | 96 | 0.025 |
| 5 | 24 | 0.118 |
| | 48 | 0.062 |
| | 72 | 0.042 |
| | 96 | 0.032 |
| 7.5 | 24 | 0.13 |
| | 48 | 0.752 |
| | 72 | 0.573 |
| | 96 | 0.39 |
| 10 | 24 | 0.158 |
| | 48 | 0.089 |
| | 72 | 0.058 |
| | 96 | 0.040 |

## 3. Results and Discussion

### 3.1. Effect of Test Duration of Exposure to Corrodent

Figure 1 shows the plot of corrosion rate (in mpy) of the as cast and the composites in 1M HCl solution against exposure time (in hrs). It can be seen that in every case, there is a decrease in the corrosion rate with an increase in duration of the exposure to the corrodent, implying that the corrosion resistance of the material tested increases as the exposure time is increased. This eliminates the possibility of hydrogen bubbles clinging on to the surface of the specimen and forming a permanent layer affecting the corrosion process. The phenomenon of gradually decreasing corrosion rate indicates the possible passivation of the matrix alloy. Visual inspection of the specimens after the corrosion tests revealed the presence of black-film covering the surface, which might have retarded the corrosion rate. De Salazar [30] explained that the protective black film consists of hydrogen hydroxy chloride, which retards the forward reaction. Castleet.al [31] pointed out that the black film consists of aluminium hydroxide compound. This layer protects further corrosion in acid media. But the exact chemical nature of such protective film is still not determined.

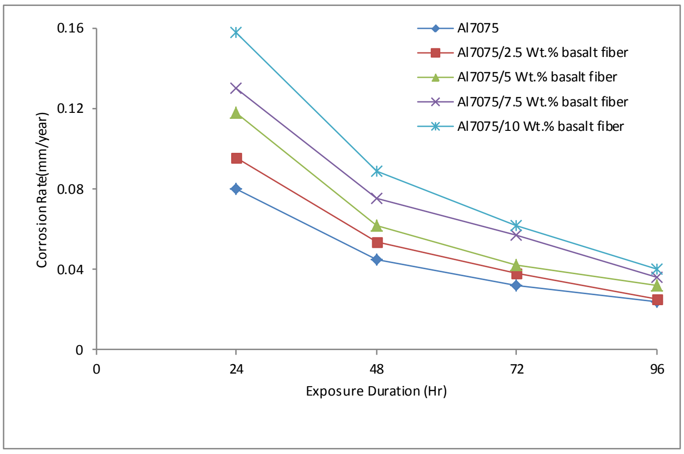


**Figure 1.** Corrosion rate of unreinforced matrix alloy and composites in 1 M HCl solution against exposure time

*3.2. Effect of Basalt Short Fiber Content*

From Figure 1, it is apparent that for both the unreinforced matrix and composite, there is a trend of decreasing corrosion rate with increase in basalt short fiber content, especially for shorter exposure times. For long exposure times, however, this effect is less pronounced. The corrosion rate of the unreinforced matrix alloy is higher than those of the composites because in the former, there is no reinforcement phase and the matrix alloy does not have much corrosion resistance to the acid medium. In the present case, the corrosion rate of the composites as well as the matrix alloy is predominantly due to the formation of pits and cracks on the surface. In the case of base alloy, the strength of the acid used induces crack formation on the surface, which eventually leads to the formation of pits, thereby causing the loss of material. The presence of cracks and pits on the base alloy surface was observed clearly. Since there is no reinforcement provided in any form the base alloy fails to provide any sort of resistance to the acidic medium. Hence, the corrosion rate in the case of unreinforced alloy is higher than that in the case of composites. Basalt fiber, being the ceramic remains inert, is hardly affected by acidic medium during the test and is not expected to affect the corrosion mechanism of the composite.

It was observed that, in basalt short fiber reinforced aluminum composites, pitting depends on the local basalt short fiber distribution. Larger weight percentages of basalt short fiber could result in more opportunities for film disruption and more sites for pit initiation. The composites show the formation of pits on the surfaces, which is more with the increase in the percentage of basalt short fiber. Figure 2 shows the SEM micrograph exposing more pit formation of the matrix alloy and 10 wt% basalt short fiber reinforced composites than the matrix alloy. This is obviously due to the matrix/fiber interface which provides favorable sites for the formation of pits on the surface which lead to the removal of material, thereby leading to a weight loss. The corrosion result indicates a decrease in the corrosion rate as the percentage of basalt short fiber increases in the composite, which shows that the basalt short fiber, directly or indirectly, influences the corrosion property of the composites. Nevertheless, the results show a decrease in the corrosion rate as the basalt fiber content is increased in the composite, indicating that the basalt fiber does influence the corrosion characteristics of the composites. Sharma *et al.* [32] who obtained similar results in glass short fiber reinforced ZA-27 alloy composites reported that the corrosion rate decreases with the increase in the reinforcement. The glass fiber definitely plays a subsidiary role as physical barriers to the initiation and developed of pitting corrosion, modifying the microstructure of the matrix material, hence improving the corrosion. B. M. Sathish *et al.* [33], who obtained similar results in glass short fiber reinforced Al 7075 alloy composites, reported that the corrosion resistance increases with the increase in the reinforcement.

*3.3. Microstructural Studies*

Figure 2 shows the micrographs of the microstructure of the Al 7075 matrix as well as the composites examined by optical microscopy before performing corrosion test. As shown in figures, the basalt short fiber was successfully dispersed into the Al 7075 matrix. The micrographs indicated that the production of bulk MMCs using compocasting technique, used in the current study, is effective. The results of the microstructure analysis are shown in Figure (2a) in both longitudinal and transverse orientations, the Al 7075 alloy shows well defined, elongated grains. Figure (2b) shows a similar visible grain structure, but much of this long grain appears to be sheared into shorter section with a greater texture. The basalt short fiber distribution was observed and some pores were absorbed with 7.5 wt.% Al/basalt short fiber as shown in Figure (2c). The composite with 10 wt.% Al/basalt short fiber did not induce variations in the fiber size; the fiber distribution was fairly uniform in the composites as shown in Figure (2d).

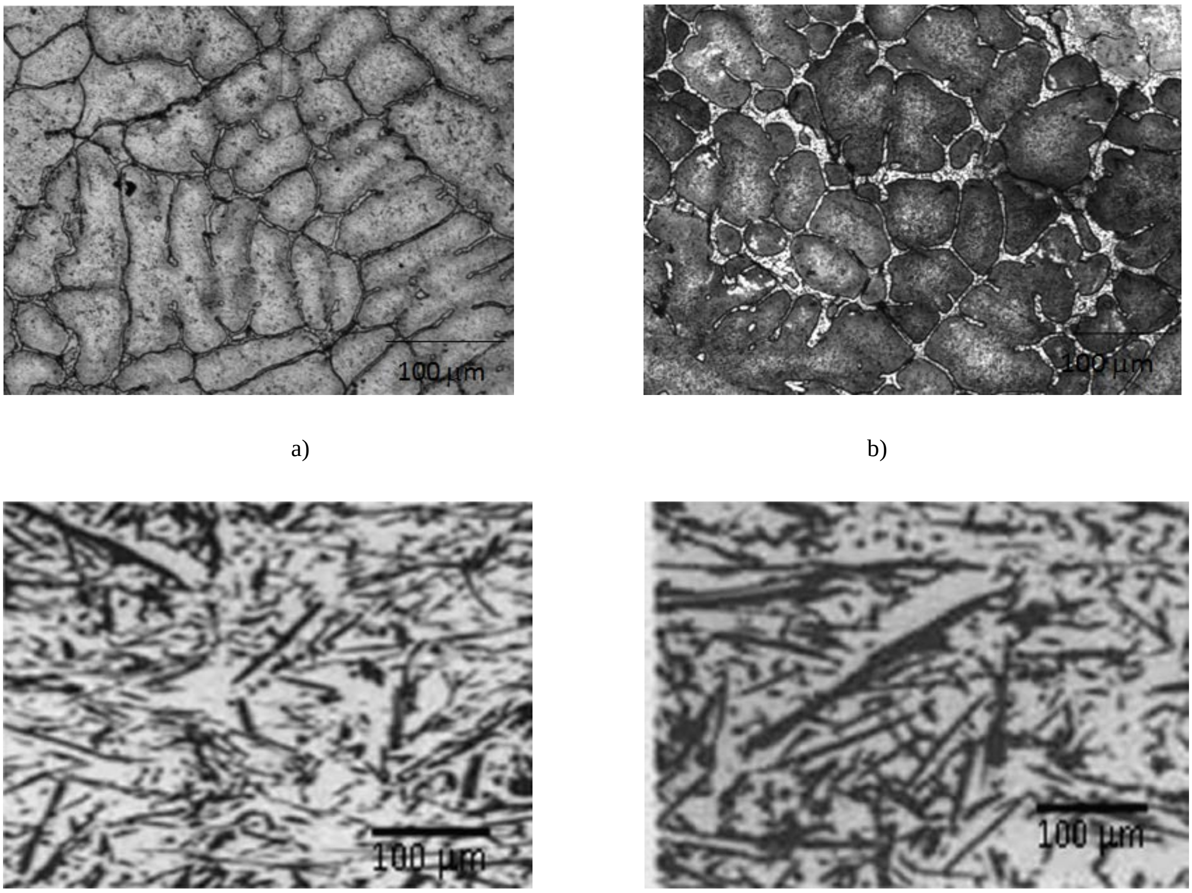


a) b)

c) d)

**Figure 2**. The microstructure of Al/ basalt short fiber composites containing a) 0 wt.%, b) 2.5 wt.%, c) 7.5 wt.%, d) 10 wt.% basalt short fiber.

*3.4. Corrosion Morphology*

Figure 3 shows a typical SEM of the unreinforced matrix alloy, revealing the presence of cracks on the surface. Pitting morphology was observed on the surface of the specimens after the tests. Small pits, not visible to the naked eye, were observed on specimens tested in acidic solutions. Inside these pits, the attack was selective along certain crystallographic directions. In the case of composites, intense localized attacks were seen at the fiber matrix interface. Pitting occurred preferentially in correspondence with basalt short fiber clusters. It gave rise to a few wide pits, which were distributed on the surface of the specimen. This was particularly evident by volcano-shaped pits appeared to be covered with white, thick, flaky corrosion product as it was in the case of 10 wt.% of basalt short fiber composites. These were seen to develop along the grain boundaries, and the crack size and depth increased with the addition of basalt fiber. The surface of the unreinforced matrix underwent a severe degradation, especially along the grain boundaries, providing preferential initiation site because of the discontinuity in the alloying elements due the changed substrate structures. Such a discontinuity would facilitate the passage of hydrogen ions to the metal, which once contacted by ions would suffer localized corrosion.

In the case of the composite containing 10% by weight of basalt short fiber, in addition to grain boundary attack, pitting occurred at the site of fiber dispersed in the matrix. The sizes of pits were seen to increase with the addition of basalt fiber. Pitting at the sites of the fiber dispersed in the matrix was found to be more dominant than the corrosion along grain boundaries. Studies of composites immersed for the prescribed periods clearly showed localized corrosion taking place at the fiber/matrix interface. Various researchers [34-36] found that MMCs show increased susceptibility to pitting attack when compared to non-reinforced alloys voids at the matrix/reinforcement interface. Surface and inter porosity of the composites tends to increase the interior exposing area of the specimens, which may increase the corrosion rate.

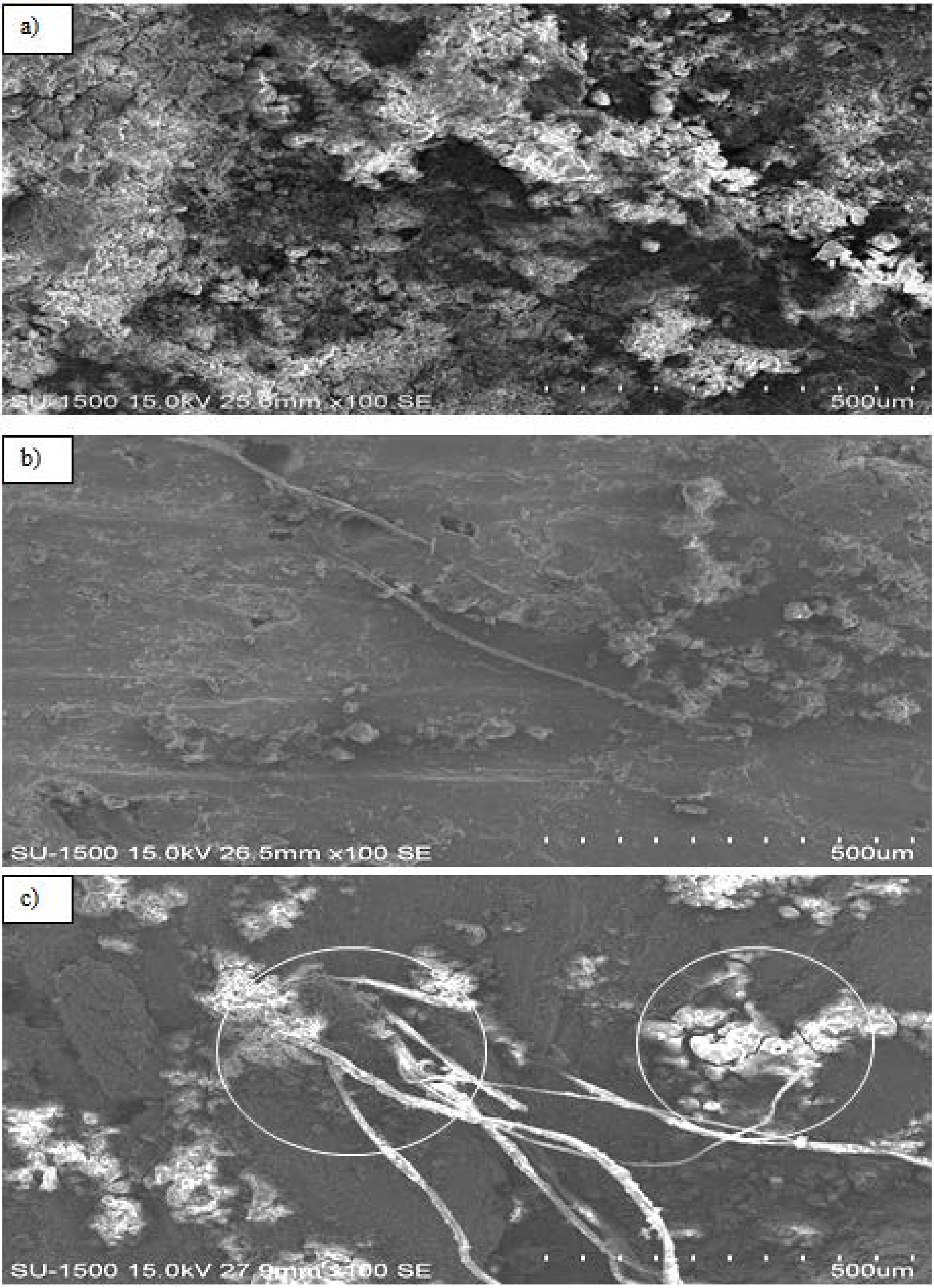


**Figure 3.** Shows corroded surface of the a) as cast Al7075 alloy, b) Al/ 5 wt. % of basalt short fiber and c) Al/ 10 wt.% of basalt short fiber composite

## 4. Conclusion

Based on the systematic study of the corrosion characteristics of Al/basalt short fiber the following conclusions are made:

- Al 7075/basalt short fiber MMCs were successfully fabricated using compo-casting method.
- Al 7075/basalt short fiber MMCs were found to corrode in 1M HCl solution.
- The corrosion rates of Al 7075/basalt short fiber MMCs as well as the matrix alloy were decreased with increasing exposure duration. However, increasing the weight percent of the basalt fiber tends to decrease the corrosion rate of the composite materials.

## References


[1] P. J. Ward, H. V. Atkinson, P. R. G. Anderson, L. G. Elias, B. Garcia, L. Kahlen and J-M. Rodriguez-Ibabe, “Semi-solid processing of novel MMCs based on hypereutectic aluminium-basal short fiber alloys” Acta Materialia, Vol. 44 (1996), No. 5 , pp.1717-1727.

[2] C. M. Ward-Close, L. Chandrasekaran, J. G. Robertson, S. P. Godfrey and D. P. Murgatroyde, “Advances in the fabrication of titanium metal matrix composite”, Materials Science and Engineering A, Vol. 263 (1999), No. 2, pp. 314-318.

[3] F. E. Kennedy, A. C. Balbahadur and D. S. Lashmore “The friction and wear of Cu-based basal short fiber carbide particulate metal matrix composites for brake applications”, Wear, Vol. 203-204(1997), pp.715-721.

[4] H. Akbulut, M. Durman and F. Yilmaz, “Dry wear and friction properties of $\delta$-$Al_2O_3$ short fiber reinforced Al-Si (LM 13) alloy metal matrix composites”, Wear, Vol. 215(1998), No.1-2, pp.170-179.

[5] B.M.Girish et.al. "Fractography, Fluidity and tensile properties of aluminium/Haematite particle composite", Journal of Mateials Engineering and performance, Vol. 8 (1999), No. 3, pp. 309-314.

[6] B.M.Satish et.al. "Effect of short glass fibers on the mechanical properties of cast ZA-27 alloy composites", Material and Design, Vol. 17 (1996), No. 5/6, pp. 245-250.

[7] P.Reynaud "Cyclic fatigue ceramic-matrix composites at ambient and elevated temperatures". Composite Science and Technology, Vol.56, (1996), pp. 809-814.

[8] Zhang H, Zuo Y. The improvement of corrosion resistance of Ce conversion films on aluminum alloy by phosphate-treatment. Applied Surface Science Vol. 254 (2008), No. 16, pp. 4930-4935.

[9] L.A. Dobrza´nski, A. Włodarczyk, M. Adamiak, “Proceedings of the Powder Metallurgy World Congress and Exhibition”, Vienna, 2004 (CD-ROM).

[10] L.A. Dobrza´nski, A. Włodarczyk, M. Adamiak, Proceedings of the 12th Scientific International Conference on Achievements in Mechanical and Materials Engineering (AMME’2003), Politechnika´ Slaska, Gliwice-Zakopane, 2003, pp. 297.

[11] Padro, A., Mercino, M.C., Viejo, F., “Influence of reinforcement proportion and matrix composition on pitting corrosion behavior of cast aluminium matrix composites”. Corros. Sci. Vol.47 (2005), pp. 1750–1764.

[12] Oguzie, E.E., “Corrosion inhibition of aluminum in acidic and alkaline media by Sansevieria trisfasciata extract”. Corros. Sci. Vol.49 (2007), pp. 1527–1539.

[13] Rehim, S.S.A., Hamdi, H.H., Mohammed, A.A., “Corrosion and corrosion inhibition of Al and some alloys in sulfate solutions containing halide ions investigated by an impedance technique”. Appl. Surf. Sci. Vol. 187(2002), pp. 279–290.

[14] Salih, S., Juaid, A.I., “Mono azo dyes compounds as corrosion inhibitors for dissolution of aluminum in sodium hydroxide solutions”. Portug. Electrochim. Act. Vol. 25 (2007), pp. 363–373.

[15] Satpati, A.K., Ravindran, P.V.,“Electrochemical study of the inhibition of corrosion of stainless steel by 1,2,3-benzotriazole in acidic media”. Mat. Chem. Phys. Vol. 109 (2008), pp. 352–359.

[16] Bakkar, A., Neubert, V., “Corrosion characterization of alumina–magnesium metal matrix composites. Corros. Sci. Vol. 49 (2007), pp. 1110–1130.

[17] Brett, C.M.A., “On the electrochemical behaviour of aluminum in acidic chloride solution”. Corros. Sci. Vol. 33 (1992), pp. 203–210.

[18] Candan, S., Biligic, E., “Corrosion behavior of Al–60 vol.% SiCp composites in NaCl solution”. Mater. Lett. Vol.58 (2004), pp. 2787–2790.

[19] Daniela Alina Necşulescu “The effects of corrosion on the mechanical Properties of aluminium alloy 7075-T6, U.P.B. Sci. Bull., Series B, Vol. 73, Iss. 1, 2011.

[20] R. Karthigeyan, et al. "Mechanical Properties and Microstructure Studies of Aluminium (7075) Alloy Matrix Composite Reinforced with Short Basalt Fibre", European Journal of Scientific Research; Vol.68 (2012), No.4, pp. 606-615.

[21] S. Ezhil Vannan, S. Paul Vizhian “Statistical Investigation on Effect of Electroless Coating Parameters on Coating Morphology of Short Basalt Fiber” Jordan Journal of Mechanical and Industrial Engineering**;** Vol. 8 (2014), No. 3, pp. 153- 160.

[22] S. Ezhil Vannan, S. Paul Vizhian “Microstructure and Mechanical Properties of as Cast Aluminium Alloy 7075/Basalt Dispersed Metal Matrix Composites” Journal of Minerals and Materials Characterization and Engineering, Vol.7 (2014), No.2, pp.182-193.

[23] S. Ezhil Vannan, S. Paul Vizhian “Corrosion Behaviour of Short Basalt Fiber Reinforced with Al7075 Metal Matrix Composites in Sodium Chloride Alkaline Medium” J. Chem. Eng. Chem. Res., Vol. 1 (2014), No. 1, pp. 1-5.

[24] D. M. Aylor and P. J. Moran, “Effect of reinforcement on the pitting behavior of aluminum-base metal matrix composites,” Journal of the Electrochemical Society, Vol. 132 (1985), No. 6, pp. 1277–1281.

[25] ASTM Standard, “Standard practice for laboratory immersion corrosion testing of metals,” American Society for Testing and Materials G31-72, 2004.

[26] ASTM Standard, “Standard practice for preparing, cleaning, and evaluating corrosion test specimens,” American Society for Testing and Materials G1-03, 2004.

[27] Weifeng Xu, Jinhe LIU, “Microstructure and pitting corrosion of friction stir welded joints in 2210-0 Aluminium alloy thick plate” Corrosion Science, Elsevier, Vol. 51(2009), pp.2743-275.

[28] B. P. Bofardi, “Control of environmental variables in water reticulating systems,” in Metals Handbook, vol. 13 of Corrosion, p. 487, ASM International, Materials Park, Ohio, USA, 9th edition, 1987.

[29] L. H. Hihara and R. M. Latanision, “Suppressing galvanic corrosion in graphite/aluminum metal-matrix composites,”Corrosion Science, Vol. 34 (1993), No. 4, pp. 655–665.

[30] J.M.G.DeSalazar, A.Urefia, S.Mazanedo and M.Barrens "Corrosion behaviour of AA6061 and AA7075 reinforced with Al2O3 particulates in aerated 3.5% chloride solution potentiodynamic measurements and microstructure evaluation", Corrosion Science, Vol. 41 (1999), pp 529-545.

[31] J.E. Castle, L.Sun and H.yan,"The use of scanning auger microscopy to locate cathodic centers in SiC/Al6061 MMC And to determine the current density at which they operate" Corrosion Science, Vol. 36 ( 1994), No. 6, pp1093-1110

[32] S.C. Sharma “Aging characterstics of short glass fiber reinforced ZA-27 alloy composites materials”, Journal of material engineering and performance, Vol. 7 (1998), No. 6, pp.741-750.

[33] B.M. Satish et.al. "Corrosion characteristics of ZaA-27/glass-fiber composites", Corrosion science, Vol. 39 (1997), No. 12, pp 2143-2150.

[34] M. A. Afifi **“**Corrosion Behavior of Zinc-Graphite Metal Matrix Composite in 1M of HCl”, Hindawi, Vol. 2 (2014), pp 1-8.

[35] B. Thirumaran, S. Natarajan, S. P. Kumaresh “Corrosion behaviour of CNT reinforced AA 7075 nanocomposites” Advances in Materials, Vol. 2 (2013), No. 1, pp 1-5.

[36] P.D. Reena Kumari, Jagannath Nayak, A. Nityananda Shetty “Corrosion behavior of 6061/Al-15 Vol. pct. SiC(p) composite and the base alloy in sodium hydroxide solution” Arabian Journal of Chemistry, Vol.15 (2012), pp 1-10.

JJMIE

Volume 9 Number 2, April.2015
ISSN 1995-6665
Pages 129 - 137

**Jordan Journal of Mechanical and Industrial Engineering**

# Sustainable Energy for Water Desalination System Relative to Basra Climate

Amani J. Majeed [*] [a], Ghadeer J. Mohammed[b], Dr. Ala'a Abdulrazaq[c]

[a] *Petroleum Engineering Dept., College of Engineering, Basra University, Iraq.*
[b] *Chemical Engineering Dept., College of Engineering, Basra University, Iraq.*
[c] *Chemical Engineering Dept., College of Engineering, Basra University, Iraq.*

*Received 17 June 2014* *Accepted 22 March 2015*

## Abstract

The use of solar energy in thermal desalination processes is one of the most promising applications of renewable energy technology. This paper deals with the principle of using solar energy to produce distillate water. The design model contains a solar collector that moves in two dimensions to absorb the direct solar energy, a heat exchanger, two multi-effect distillation units, and a condenser. This model was simulated under Basra weather conditions for four months in 2012. The results showed that the productivity of the proposed desalination system are 5.3, 6.4, 5.3, and 4.4m3/hour for the four months March, June, September and December, respectively. Moreover, inclusion of a thermal fluid heat transfer process, inside the absorber tubes, has improved the productivity of the system.



**Keywords:** *Solar energy; Desalination system; Basra weather conditions*.

## Nomenclature

| | |
|---|---|
| $A$ | Heat transfer area ($m^2$) |
| $A_{g2}$ | Outer side cross section area of glass envelope ($m^2$) |
| $A_T$ | Surface area of tube ($m^2$) |
| $C_{pc}$ | Heat capacity of cold fluid (kJ/kg.K) |
| $C_{ph}$ | Heat capacity of hot fluid (kJ/kg.K) |
| $D_{a2}$ | Outer side diameter of absorber (m) |
| $D_b$ | Bundle diameter (mm) |
| $D_g$ | Diameter of glass envelope (m) |
| $D_{g1}$ | Inner side diameter of glass envelope (m) |
| $D_s$ | Shell diameter (mm) |
| $d_e$ | Equivalent diameter (mm) |
| $d_i$ | Tube inside diameter (mm) |
| $d_o$ | Tube outside diameter (mm) |
| $F$ | Log mean temperature difference correction factor |
| $G$ | Gravitational acceleration ($m/s^2$) |
| $h_i$ | Heat transfer coefficient inside tube ($W/m^2.K$) |
| $h_{id}$ | Tube side fouling factor ($W/m^2.K$) |
| $h_o$ | Heat transfer coefficient outside tube ($W/m^2.K$) |
| $h_{od}$ | Shell side fouling factor ($W/m^2.K$) |
| $j_h$ | Heat transfer factor |
| $k_f$ | Thermal conductivity of fluid (W/m.K) |
| $K_t$ | Constant |
| $k_w$ | Thermal conductivity of tube wall material (W/m.K) |
| $L$ | Tube length (m) |
| $m^{\cdot}_c$ | Mass flow rate of cold fluid (kg/s) |
| $m^{\cdot}_h$ | Mass flow rate of hot fluid (kg/s) |
| $N_t$ | Number of tube in tube bundle |
| $n_1$ | Constant |
| $P$ | Pressure (bar) in Eq.( 21 , 26 )<br>Pressure ( KPa ) in Eq.( 5 ) |
| $P_C$ | Critical pressure (bar) |
| $P_r$ | Prandtl number |
| $P_t$ | Tube pitch (mm) |
| $Q^{\cdot}_{out}$ | Thermal loss from collector (kJ/s) |
| $Re$ | Reynolds number |
| $r_{a1}$ | Inner side radius of absorber (m) |
| $r_{a2}$ | outer side radius of absorber (m) |
| $r_{g1}$ | Inner side radius of glass envelope (m) |

[*] Corresponding author. e-mail:a_j295@yahoo.com.

| | |
|---|---|
| $r_{g2}$ | outer side radius of glass envelope (m) |
| $S$ | Dimensionless temperature ratio |
| $T_{a1}$ | Inner side temperature of absorber (K) |
| $T_{a2}$ | Outer side temperature of absorber (K) |
| $T_{c,in}$ | Tube side inlet temperature (K) |
| $T_{c,out}$ | Tube side outlet temperature (K) |
| $T_f$ | Temperature of heating transfer fluid (K) |
| $T_{g1}$ | Inner side temperature of glass envelope (K) |
| $T_{g2}$ | Outer side temperature of glass envelope (K) |
| $T_{h,in}$ | shell side inlet temperature (K) |
| $T_{h,out}$ | shell side outlet temperature (K) |
| $T_{lm}$ | Logarithmic mean temperature difference |
| $T_m$ | Mean temperature difference |
| $T_w$ | Tube wall temperature |
| $T_\infty$ | Temperature evaluation at free stream conditions |
| $t_{c,in}$ | Tube side inlet temperature (°C) |
| $t_{c,out}$ | Tube side outlet temperature (°C) |
| $t_{h,in}$ | shell side inlet temperature (°C) |
| $t_{h,out}$ | shell side outlet temperature (°C) |
| $U_o$ | Overall heat transfer coefficient based on tube outside area ($W/m^2.K$) |
| $u_T$ | Tube side fluid velocity (m/s) |
| $\varepsilon_{g1}$ | Inner side emissivity of glass envelope |
| $\varepsilon_{g2}$ | outer side emissivity of glass envelope |
| $\eta_{opt.}$ | Optical Efficiency |
| $\tau_g$ | Transmissivity of glass envelope |

## 1. Introduction

Sustainable Energy describes clean sources of energy that has fewer environmental impacts than conventional energy generating technologies. Sustainable sources of energy include solar, wind, hydro, biomass and geothermal. The lack of potable water poses a big problem in the arid regions of the world where freshwater is becoming more scarce and expensive. The availability of clean drinking water is one of the most important international health issues today. The growing world population, together with increased industrial and agricultural activity all over the world, contributes to the depletion and pollution of freshwater resources. Desalination is one of earliest forms of water treatment, still commonly used throughout the world today. Desalination is a process that removes dissolved minerals from seawater and treated wastewater. A number of technologies have been developed for desalination including reverse osmosis (RO), distillation, electro dialysis and vacuum freezing [1]. Distillation is a method of separating mixtures based on difference in their volatilities in a boiling liquid mixture. The most common method of distillation includes multistage flash (MSF), multi effect distillation (MED) and vapor compression (VC). In MSF, the feed water is heated and the pressure is lowered, so the water "flashes" into steam. In MED, the feed water passes through a number of evaporators in series. Vapor from one series is then condensed and evaporated in the next series to reduce the concentration of impurities [1].

Kalogirou [2] estimated that the production of $1000m^3$/day of freshwater requires 10,000 tons of oil per year. This is a significant as it involves a recurrent energy expense which few of the water-scarce areas of the world can afford. Large commercial desalination plants using fossil fuel are used by a number of oil-rich countries to supplement the traditional sources of water. People in many other countries have neither the money nor the oil resources to allow them to develop in a similar manner. Problems relevant to the use of fossil fuels could be resolved by considering possible utilization of renewable energy resources instead of fossil fuels.

Solar energy has the greatest potential of all the sources of the renewable energy and if a small amount of this form of energy could be used, it will be one of the most important energy supplies, especially when other sources in the country have depleted. Solar power is approximately equal to 1017 kW and the total demand is 1013 W. Therefore, the sun gives 1000 times more power than required. If 5% of this energy can be used, it will be 50 times what the world will require. The energy radiated by the sun on a bright sunny day is 4 to 7 kWh per $m^2$ [3].

Dai and Zang [4-5] proposed an open-air cycle desalination system, in which seawater heated by the sun in a collector and then sprayed on the surface of a honeycomb wall in the humidifier. The air that became hot and humid as it blown through the humidifier led to the condensation area between the feed water tubes, where it cooled and fresh water condensates in the collection container. In order to increase the thermal efficiency, the part of the warm seawater that was not picked up by the air in the honeycomb collected and led back into the seawater tank for another round in the humidification-dehumidification process. Since the air flowed in a straight line, unnecessary pressure losses were avoided. During experiments with this desalination system, a freshwater gain of 6.2 $kg/m^2$ per day was observed for cases when solar radiation was 700 $W/m^2$ and the operation time was 8 hours per day. The thermal efficiency of the system was estimated to be 85%.

An interesting study is presented by Chafik [6], where the air is heated and humidified in several steps inside a simple solar collector, This lead to higher vapour content in the air and a lower required airflow rate. Air with an initial temperature and specific humidity of 25ºC and 10 g vapour/kg dry air, respectively, enters the solar air-heating collector. During the first step in the collector, the air is warmed to 50ºC and then humidified by sprinklers with seawater until the air is approximately saturated. Due to the heat required for the evaporation of the water, the air temperature decreases to about the wet bulb temperature of 23ºC. In the next step, the air again heated to 50ºC and then humidified in the same way to vapor content of 28 g vapour/kg dry air. The air temperature goes down to 31ºC. During the third step the air is heated to 56ºC and humidified to 36 g vapour/kg dry air at 35ºC.

## 2. System Description

As shown in Figure (1) the proposed desalination system consists of a solar collector, a steam generator, a multi-effect distillation unit (MED) and a condenser. The reflective parabolic surface of collector focuses the solar direct radiation on the linear absorber.

The solar radiation is converted to thermal energy, which is absorbed by heat transfer fluid (HTF) flow through the collectors. The water is pumped from the sea through the condenser, where it is heated by energy transferred from the warm steam leaving the evaporator[7]. The water is then vaporized in the steam generator before it flows into the evaporators (MED) due to the absorption of heat from HTF out of the collectors.

## 3. Mathematical Modeling

### *3.1. Solar Collectors Design Equation*

In order to design the solar collector system and predict overall system performance, it was necessary to build a mathematical model for the parabolic trough solar collector.

In a steady state, the performance of a parabolic trough solar collector is described by an energy balance that indicates the distribution of incident solar energy into useful energy gain, thermal losses, and optical losses. The solar radiation absorbed by the receiver, $\dot{Q}_{abs}$, on an hourly basis is equal to the multiply of direct incident solar radiation $I_{dn}$, the optical efficiency $\eta_{opt}$, and the cross sectional area, $A_a$ as shown in Equation(1). The optical efficiency of a collector estimated Equation (2), where *A* is the effective area ratio [8].

$$\dot{Q}_{abs} = A_a\,\eta_{opt}\,I_{dn} \tag{1}$$

$$\eta_{opt} = r\,\tau_g\,\alpha\,A\,\eta_{op} \tag{2}$$

The thermal loss from the collector to the surroundings is calculated by considerable detail heat transfer Equation here [8].

$$\dot{Q}_{out} = \dot{Q}_{abs} - \dot{Q}_{loss} \tag{3}$$

The solar radiation, calculated by Equation (4), is absorbed by glass envelope and the absorber tube, the energy loss through glass envelope and support structure, calculated by Equation (5), is due to convection and radiation from glass to surrounding and conduction between the absorber and support structure, respectively.

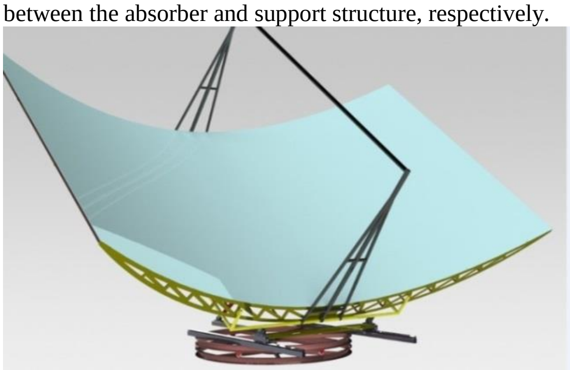

**Figure 2.** Parabolic Trough Collector with two-axis Tracking Surface

$$\hat{q}_{SolAbs} = q_i\,\alpha_g\,K_i + q_i\,\tau_g\,\alpha_a\,K_i \tag{4}$$

$$\hat{q}_{Thermalloss} = \sigma A_{g2}\,\varepsilon_{g2}\left(T_{g2}^{4} - T_{Sky}^{4}\right) + \pi D_g\,h(T_{g2} - T_{\Psi}) + \sqrt{hPAK}\left(T_{base} - T_{\infty}\right) \tag{5}$$

Where,

$$T_{sky} = 0.0552\,T_{\infty}^{1.5} \tag{6}$$

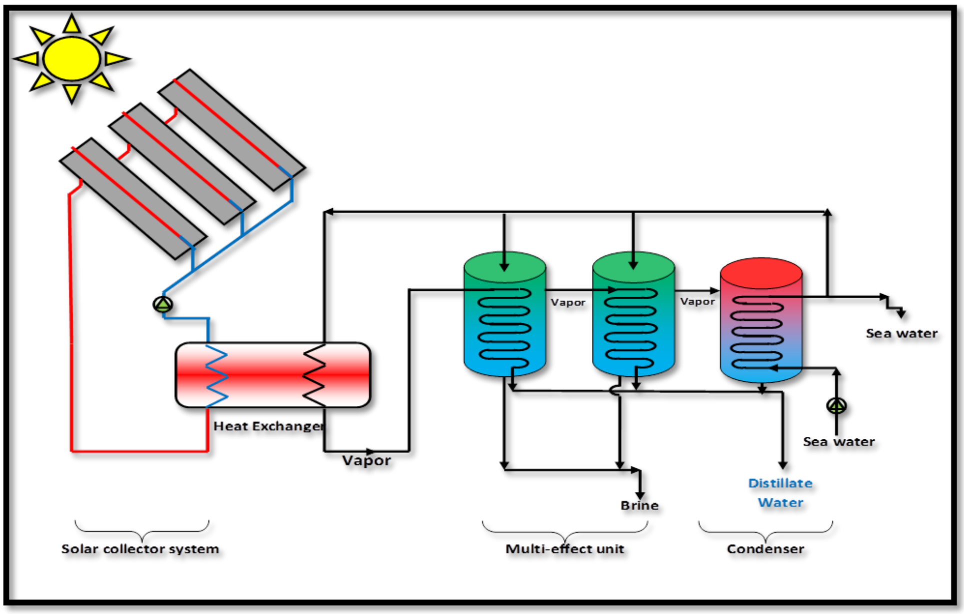


**Figure 1.** Schematic of the Thermal Solar Distillation system

For the outer surface of the glass, the heat gained from solar radiation ($\hat{q}_s$) and glass ($\hat{q}_g$) by conduction is equal to the heat losses from the outer surface to ambient by means of convection ($\hat{q}_c$) and radiation ($\hat{q}_r$), indicated in Equation (7).

$$\hat{q}_s + \hat{q}_g = \hat{q}_c + \hat{q}_r \tag{7}$$

Where,

$$\hat{q}_s = q_i \ \alpha_g \ K_i \tag{7a}$$

$$\hat{q}_g = \frac{2\pi k\left(T_{g1} - T_{g2}\right)}{ln\left(r_{g2} / r_{g1}\right)} \tag{7b}$$

$$\hat{q}_c = \pi D_g \ h\left( T_{g2} - T_\infty \right) \tag{7c}$$

$$\hat{q}_r = \sigma A_{g2} \ \varepsilon_{g2} \left( T_{g2}^4 - T_{sky}^4 \right) \tag{7d}$$

For the inner surface of glass, heat gained from the absorber outer surface to the inner surface of glass by convection ($\hat{q}_{c,g}$) and radiation ($\hat{q}_{r,g}$). It is equal to the heat loss by means of the conduction through glass as ($\hat{q}_g$) shown in Equation (8).

$$\hat{q}_g = \hat{q}_{c,g} + \hat{q}_{r,g} \tag{8}$$

Where,

$$\hat{q}_{c,g} = \pi D_{a2} \ h\left(T_{a2} - T_{g1}\right) \tag{8a}$$

$$q_{r,g} = \frac{\sigma \pi D_{a2}\left(T_{a2}^4 - T_{g1}^4\right)}{\frac{1}{\varepsilon_{a2}} + \frac{D_{a2}}{D_{g1}}\left(\frac{1}{\varepsilon_{g1}} - 1\right)} \tag{8b}$$

The heat conducted to absorber is equal to the heat transferred by convection from absorber to the heat transfer fluid shown in Equation (9) [9-14].

$$\hat{q}_{cond\text{-}a} = \hat{q}_{conv\_fluid} \tag{9}$$

Where;

$$\hat{q}_{cond\text{-}a} = \frac{2\pi k\left(T_{a1} - T_{a2}\right)}{ln\left(r_{a2} / r_{a1}\right)} \tag{9a}$$

$$\hat{q}_{conv\_fluid} = \pi \ D_h \ h\left(T_{a1} - T_f\right) \tag{9b}$$

*3.2. Heat Exchangers*

Heat exchangers are devices that facilitate the exchange of heat between two fluids at different temperatures while keeping them from mixing with each other. They are commonly used in practices in a wide range of application, from heating in household to chemical processing in large plants [15].

Heat exchangers may be called by other names depending upon their specific purpose. Such as, cooler, condenser, vaporizer, heater and if two process fluids exchange heat, the term heat exchanger is used [16].

*3.2.1. Calculate Heat Duty:*

According to the first law of thermodynamics, the heat transfer across a surface involving phase change is given by;

$$\begin{aligned} Q &= \dot{m}_c C_{Pc}\left(T_{c,out} - T_{c,in}\right) + \dot{m}_c \ \lambda \\ &= \dot{m}_h C_{Ph}\left(T_{h,in} - T_{h,out}\right) + \dot{m}_h \ \lambda \end{aligned} \tag{10}$$

The rate of heat transfer in a heat exchanger can also be expressed in an analogous manner to Newton's law of cooling as [15]

$$Q = U A \Delta T_m \tag{11}$$

In order to have good results, the following assumptions must be made:

- The heat exchanger is at steady state.
- Each stream has a constant specific heat.
- The overall heat transfer coefficient is constant.
- There are no heat losses from the heat exchanger.
- There is no longitudinal heat transfer in the heat exchanger.
- The flow is counter-current.

*3.2.2. Calculate Logarithmic Mean Temperature Difference:*

The logarithmic means of the terminal temperature differences [17] is calculated as:

$$\Delta T_{lm}\left(LMTD\right) = \frac{\left(t_{h,in} - t_{c,out}\right) - \left(t_{h,out} - t_{c,in}\right)}{ln\left(\frac{t_{h,in} - t_{c,out}}{t_{h,out} - t_{c,in}}\right)} \tag{12}$$

In design, a correction factor is applied to the $\Delta T_{lm}$ to allow for the departure from true countercurrent flow to determine the true temperature difference [18]

$$\Delta T_m = F \ \Delta T_m \tag{13}$$

The correction factor is a function of the temperature of the fluids and the number of tube and shell passes and is correlated as a function of two dimensionless temperature ratios [17]

$$R = \frac{t_{h,in} - t_{h,out}}{t_{c,out} - t_{c,in}} = \frac{\text{range of shell fluid}}{\text{range of tube fluid}} \tag{14}$$

$$S = \frac{t_{c,out} - t_{c,in}}{t_{h,in} - t_{c,in}} = \frac{\text{range of tube fluid}}{\text{maximum temperature difference}} \tag{15}$$

*3.2.3. Choose Shell and Tube Passes*

The single shell pass type is by far the most commonly used. The fluid in the tube is usually directed to flow back and forth in a number of “passes” through groups of tubes arranged in parallel, to increase the length of the flow path, In order to give the required tube-side design velocity. Exchangers are built with from one to up to about sixteen tube passes.

*3.2.4. Assume an Initial Value for the Overall Heat Transfer Coefficient*

There are many typical values for the heat transfer coefficient for a various type of heat exchanger which can be taken as a trail values for starting a thermal design. They are given in Table 1 [19]

*3.2.5. Calculate the Total Area of the Heat Exchanger*

$$A = \frac{Q}{U\,\Delta T_m} \tag{16}$$

*3.2.6. Choose Diameter and Length of Tubes*

Tubes diameters are in the range of 16mm to 50mm.Smaller diameters are preferred because they will give a more compact and therefore cheaper heat exchanger. Larger tubes will be selected for heavily fouling fluids.

The preferred lengths of tubes for heat exchangers are: 1.83 m, 2.44 m, 3.66 m, 4.88 m, 6.10 m and 7.32 m. The use of longer tubes will reduce the shell diameter which will generally result in a lower cost exchanger. The optimum tube length to shell diameter will usually fall within the range of 5 to 10 [19].

*3.2.7. Calculate Area of One Tube*

$$A_T = \pi d_0 L \tag{17}$$

*3.2.8. Calculate Number of Tube*

$$N_t = A / A_T \tag{18}$$

*3.2.9. Select Tube Pitch Arrangement*

The tubes in a heat exchanger are usually arranged in an equilateral triangular, square, or rotated square pattern.

- The triangular and rotated square patterns give higher heat-transfer rates and has higher shell side pressure drop.
- A square, or rotated square arrangement, is used for heavily fouling fluids.

$$P_t = 1.25\, d_0 \tag{19}$$

*3.2.10. Calculate Bundle Diameter*

The bundle diameter will depend not only on the number of tubes but also on the number of tube passes because spaces must be left in the pattern of tubes on the tube sheet to accommodate the pass partition plates.

$$D_b = d_o \left( \frac{N_t}{K_t} \right)^{1/n_1} \tag{20}$$

The values of $N_t$ and $K_t$ constants are given in Table 2 [19].

*3.2.11. Calculate the Shell-Bundle Clearance*

The shell diameter must be fit to the tube bundle to reduce bypassing round the outside of the bundle. The typical values of clearance are given in Figure 19 [19]. It will depend on the heat exchanger type.

$$D_s = D_b + clearance \tag{21}$$

*3.2.12. Calculate Tube Side Heat Transfer Coefficient*

1. Steam Generator:-

$$h_T = 0.104 (P_C)^{0.69} (q)^{0.7} [1.8 (P/P_C)^{0.17} + 4 (P/P_C)^{1.2} + 10 (P/P_C)^{10}] \tag{22}$$

2. Multi Effect (MED):-

$$h_T = 0.815 \left( \frac{\kappa_L \rho_L (\rho_L - \rho_V) g \lambda}{\pi \mu_L d_o (T_{sat} - T_w)} \right)^{0.25} \tag{23}$$

Where physical properties are at wall temperature

*Tw = Mean Shell Temperature + Mean Tube Temperature*

3. Condenser:-

$$h_T = 4200 (1.35 + 0.02\, t) u_T^{0.8} / d_o^{0.2} \tag{24}$$

*3.2.13. Calculate Shell-side Heat Transfer Coefficient*

1. Steam Generator:-

$$h_s = (\kappa_f / d_e)\, j_h\, Re\, Pr^{1/3} \tag{25}$$

Where physical properties are at mean shell temperature and

$$d_e = (1.10 / d_o) (P_t^2 - 0.917 d_o^2) \tag{26}$$

2. Multi Effect (MED):-

$$h_s = 0.104 (P_C)^{0.69} (q)^{0.7} [1.8 (P/P_C)^{0.17} + 4 (P/P_C)^{1.2} + 10 (P/P_C)^{10}] \tag{27}$$

3. Condenser:-

$$h_T = 0.725 \left( \frac{\kappa_L{}^3 \rho_L (\rho_L - \rho_V) g \lambda}{\mu_L d_o (T_{sat} - T_w)} \right)^{0.25} \tag{28}$$

Where physical properties are at wall temperature

*3.2.14. Select Fouling Factors*

Most fluids will foul the heat-transfer surfaces in an exchanger duo to the deposition of material which have a relatively low thermal conductivity and will reduce the overall heat transfer coefficient. The effect of fouling is allowed for in design by including the inside and outside fouling coefficients,Table 3 [19].

Fouling factor for seawater is 2000 W/m$^2$.°C
Fouling factor for water is 4000 W/m$^2$.°C
Fouling factor for HTF is W/m$^2$.°C

 

*3.2.15. Calculate the Overall Heat Transfer Coefficient:-*

$$\frac{1}{U_o}=\frac{1}{h_o}+\frac{1}{h_{od}}+\frac{d_o \ln\left(d_o/d_i\right)}{2k_w}+\left(d_o/d_i\right)\left(\frac{1}{h_{id}}+\frac{1}{h_i}\right) \quad (29)$$

## 4. Results and Discussion

Figures from (3) to (6) show that the absorbed solar energy (that absorbed by glass envelope and absorber tube) vs. time for a specified day 15th of each month in 2012, demonstrated that the value of solar energy that absorbed by absorber tube is larger than that absorbed by the glass envelope, this is acceptable because the absorbed energy depend on the absorptivity and the type of the absorber; therefore, when the absorber tube surface supported with selective coating, the tube absorbs large amount of energy because of the two dimensions parabolic through collector, the collector absorbed large amount of solar energy.

Figures from (7) to (10) explain the related collector outlet temperature (that out from solar collector) vs. time, and the temperature of heat transfer fluid that leave the heat exchanger which calculated through simulation with the discussed plant model for a specified day 15th of (March, June, September, and December) in 2012.

Figures (11) to (14) Show the effect of time on the value of the overall heat transfer coefficient in four different months. It is clear that the value of the overall heat transfer coefficient is increasing with time until 12 PM because with time temperature of HTF will be increased, and that because the amount of heat absorbed by the absorber tube glass will be increased until 12 PM. After 12 PM, temperature of HTF will be decreased with time and that because the amount of heat absorbed by the absorber tube glass will be decreased with time. The value of the overall heat transfer coefficient will be increased with time until 12 PM due to the increasing in the amount of heat absorbing by the tube glass and vs. versa.

Figures (15) to (17) Show the effect of time on the production of distillated water. These figures show that the production of distillated water will be increased with time, since the amount of steam produced from steam generator per hour is constant. So the water distillate per hour will be constant and the accumulative amount of distillated water will be increase with time.

The same figures Show the effect of time on the overall production of distillated water. These figures show that the production of distillated water will be increased with time, since the rate of steam produced from each effect which will inter the next effect is constant. So the rate of water distillate will be constant and the accumulative amount of distillated water will be increase with time.

Figure (18) shows that the large production of distillated water was been at June. This is because the hot weather of Basra and the long day hours at June, which means the amount of heat absorbed by the absorber tube glass will be larger than that at March, September and December.

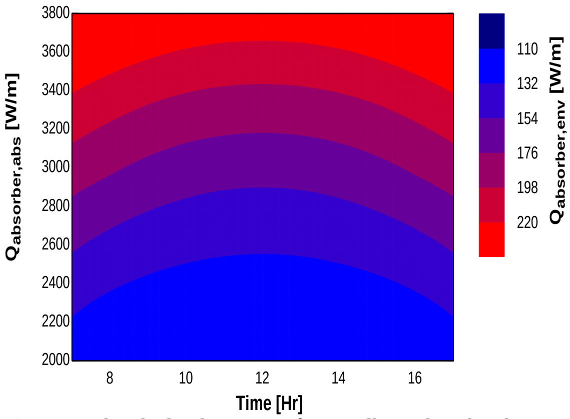


**Figure 3**. Absorbed Solar Energy from Collector by Absorber Tube & Class Envelope for 15 March 2012.

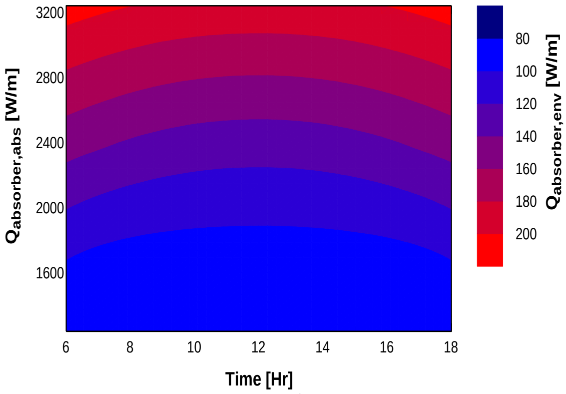


**Figure 4.** Absorbed Solar Energy from Collector by Absorber Tube & Class Envelope for 15 June 2012.

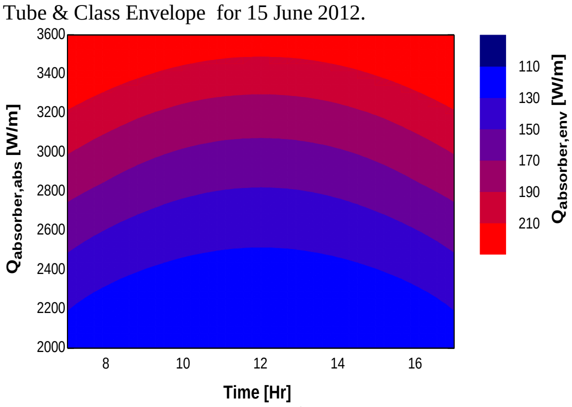


**Figure 5.** Absorbed Solar Energy from Collector by Absorber Tube & Class Envelope for 15September 2012.

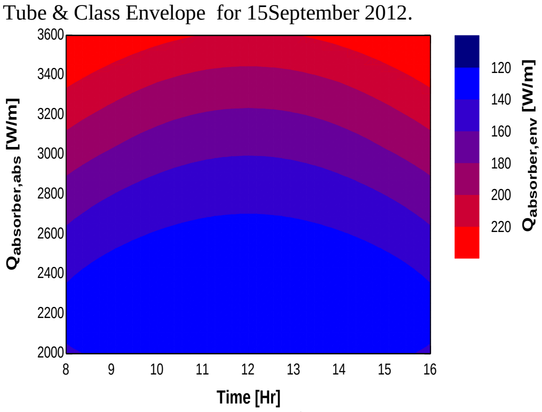


**Figure 6.** Absorbed Solar Energy from Collector by Absorber Tube & Class Envelope for 15 December 2012.

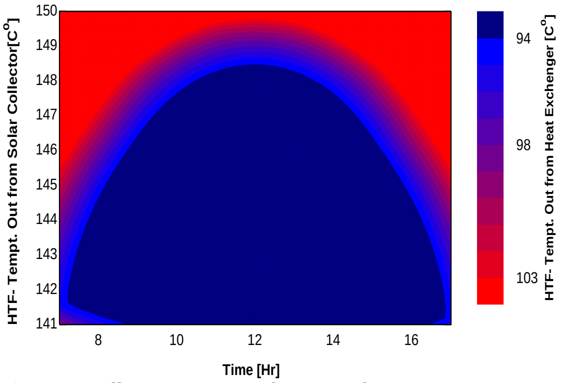


**Figure 7.** Collector & Heat Exchanger outlet temperature vs. time on 15 May 2012

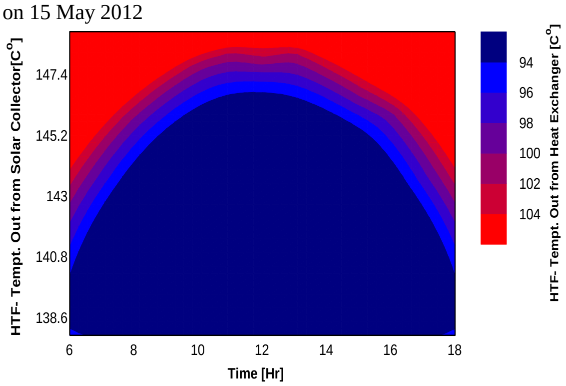


**Figure 8.** Collector & Heat Exchanger outlet temperature vs. time on 15 June 2012

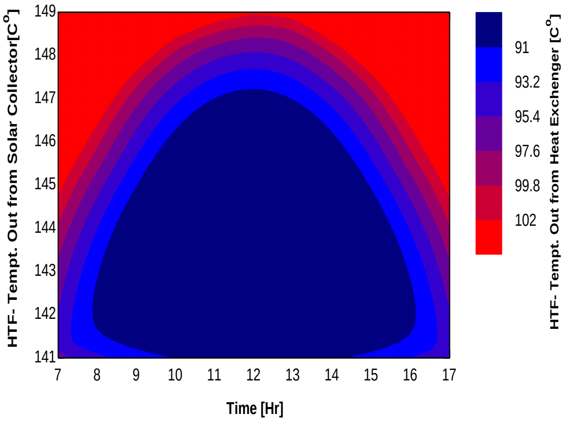


**Figure 9.** Collector & Heat Exchanger outlet temperature vs. time on 15 September 2012

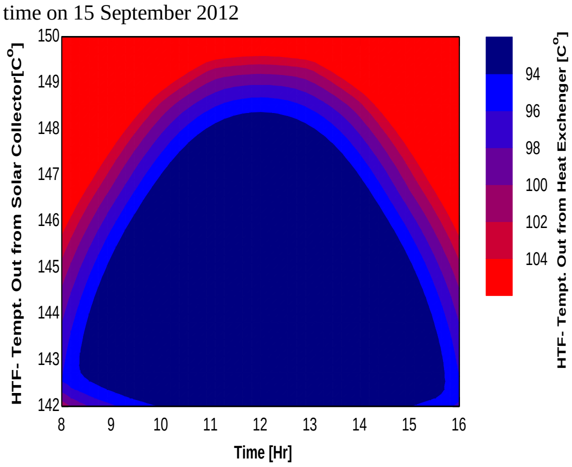


**Figure 10.** Collector & Heat Exchanger outlet temperature vs. time on 15 December 2012

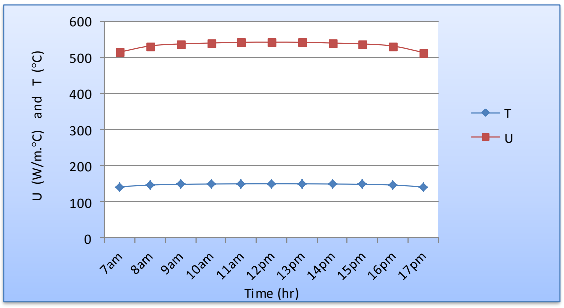


**Figure 11.** Shows the change in the values of temperature and overall heat transfer coefficient vs. time on March in the first effect.

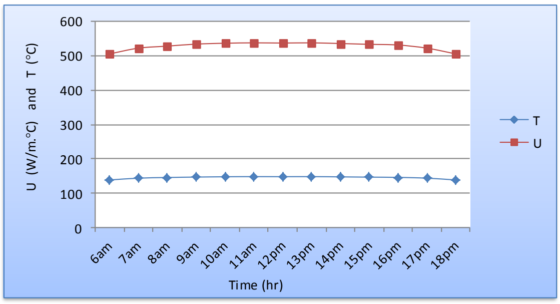


**Figure 12.** Shows the change in the values of temperature and overall heat transfer coefficient vs. time on June in the first effect.

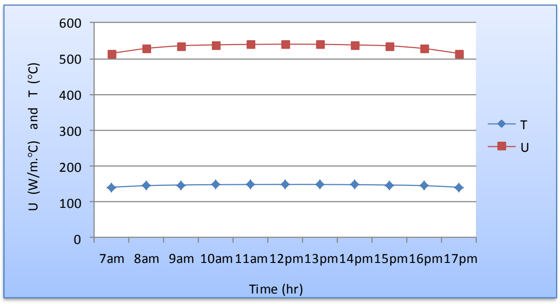


**Figure 13.** Shows the change in the values of temperature and overall heat transfer coefficient vs. time on September in the first effect.

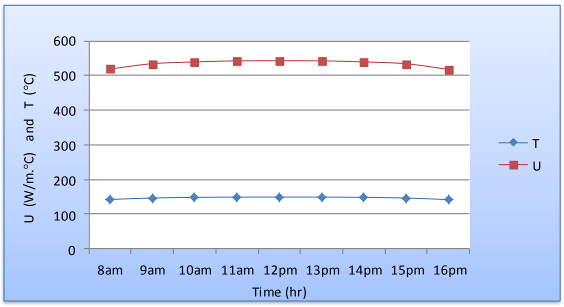


**Figure 14.** Shows the change in the values of temperature and overall heat transfer coefficient vs. time on November in the first effect.

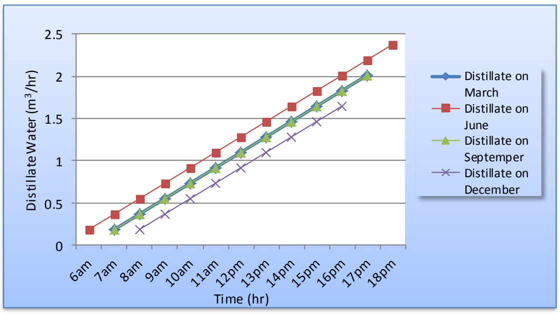


**Figure 15.** Shows the amount of water produce from first effect during four month.

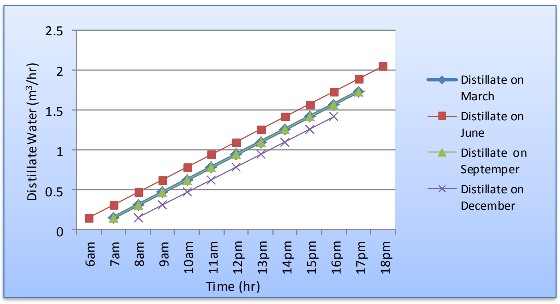


**Figure 16.** Shows the amount of water produce from second effect during four month.

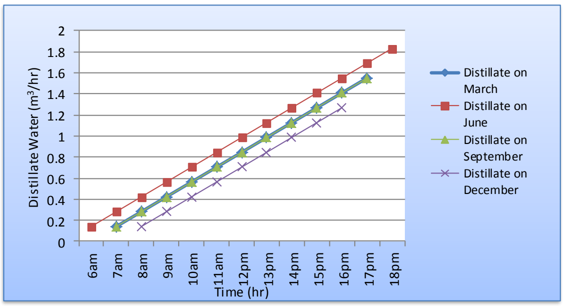


**Figure 17.** Shows the amount of water produce from condenser during four month.

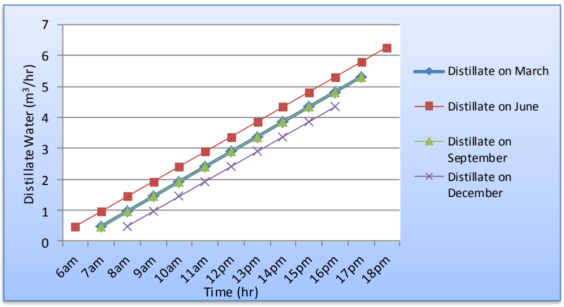


**Figure 18.** Shows the amount of water produce from the plant during four month.

## 5. conclusion

- The ability of using the solar system in the regions suffering from water scarcity. The nature of weather in Basra city support the ability of using the solar system with acceptable rate of production especially during the crises or emergency times.
- The record values of Basra climate conditions (solar intensity and outlet temperature of collector) for four months have shown a high fluctuation from month to month. So the water productivity varied between ( 4.4 - 6.4 ) $m^3$/hr.
- The relation between water productivity and solar intensity is proportional.

## References

[1] F.A. Oyawale, A.O. Odior, M.M. Ismaila, "Design and Fabrication of a Water Distiller". Journal of Emerging Trends in Engineering and Applied Sciences, Vol. 1 (2010) No. 2, 168-173.

[2] S.A. Kalogirou, "Seawater desalination using renewable energy sources". Progress in Energy and Combustion Science, Vol. 31 (2005) No. 3, 242–281.

[3] A. Kumar, G.D. Sootha, P. Chaturvadi, "Performance of a multi-stage distillation system using a flat-plate collector". Extended Abstract, ISES Solar World Congress, Kobe, Japan, (1989).

[4] Y.J. Dai, R.Z. Wang, H.F. Zhang, "Parametric analysis to improve the performance of a solar desalination unit with humidification and dehumidification". Desalination, Vol. 142 (2002) No. 2, 107-118.

[5] Y.J. Dai, H.F. Zhang, "Experimental investigation of a solar desalination unit with humidification and dehumidification". Desalination, Vol. 130 (2000) No. 2, 169-175.

[6] E. Chafik, "A new seawater desalination process using solar energy". Desalination, Vol. 153 (2003) No. 1-3, 25-37.

[7] C. Lourens, E. Uken, M. Kilfoil, "Low Temperature Solar Powered Distillation of Seawater". Cape Peninsula University of Technology, Cape, South Africa, 2006.

[8] N. Mukund, V. Muthu Raman, " Improved Method of Desalination of Seawater with Electric Power Generation using Solar Energy"2nd International Conference on Environmental Science and Development, Singapore, 2011.

[9] M. Khoukhi, S. Maruyama, "Theoretical approach of a flat plate solar collector with clear and low-iron glass covers taking into account the spectral absorption and emission within glass covers layer". Renewable Energy, Vol. 30 (2005) No. 8, 1177-1194.

[10] R. Forristall, "Heat Transfer Analysis and Modeling of a Parabolic Trough Solar Receiver Implemented in Engineering Equation Solver", National Renewable Energy Laboratory, (2003).

[11] M. Yaghoubi, F. Ahmadi, M. Bandehee, "Analysis of Heat Losses of Absorber Tubes of Parabolic through Collector of Shiraz (Iran) Solar Power Plant"Journal of Clean Energy Technologies, Vol. 1 (2013 ) No. 1, 33-37.

[12] WIRZ M. Optical and Thermal Modeling of Parabolic Through Concentrator Systems. Dissertation thesis, Bern, (2014).

[13] M. Yaghoubi, K. Azizian, A. Kenary, "Simulation of Shiraz solar power plant for optimal assessment". Renewable Energy, Vol. 28 (2003) No. 12, 1985–1998.

[14] Duffie JA., Beckman WA. Solar Engineering of Thermal Processes. 3rd ed. New York: John Wiley and Sons; 1991.

[15] Cengel Y., Cimbala J., Turner R. Fundamentals of Thermal-Fluid sciences. 4th ed. New York: McGraw-Hill; 2012.

[16] Couper JR., Penney WR., Fair JR. Chemical Process Equipment. 3rd ed. United Kingdom: Butterworth-Heinemann; 2012.

[17] Modi J. Quick Manual Design of Shell and Tube Heat Exchanger. M.Sc. Thesis, Poona University, India, 1991.

[18] Edwards J.E., "Design and Rating Shell and Tube Heat Exchangers", Process and Engineering Services to Industry Worldwide.

[19] Sinnott R.K. Coulson and Richardson's Chemical Engineering series. Volume 6. 3rd ed. United Kingdom: Butterworth-Heinemann; 1991.

## Appendix

**Table 1**. Typical overall coefficients [19],

**Shell and tube exchangers**

| Hot fluid | Cold fluid | $U$ (W/m$^2$°C) |
|---|---|---|
| *Heat exchangers* | | |
| Water | Water | 800–1500 |
| Organic solvents | Organic solvents | 100–300 |
| Light oils | Light oils | 100–400 |
| Heavy oils | Heavy oils | 50–300 |
| Gases | Gases | 10–50 |
| *Coolers* | | |
| Organic solvents | Water | 250–750 |
| Light oils | Water | 350–900 |
| Heavy oils | Water | 60–300 |
| Gases | Water | 20–300 |
| Organic solvents | Brine | 150–500 |
| Water | Brine | 600–1200 |
| Gases | Brine | 15–250 |
| *Heaters* | | |
| Steam | Water | 1500–4000 |
| Steam | Organic solvents | 500–1000 |
| Steam | Light oils | 300–900 |
| Steam | Heavy oils | 60–450 |
| Steam | Gases | 30–300 |
| Dowtherm | Heavy oils | 50–300 |
| Dowtherm | Gases | 20–200 |
| Flue gases | Steam | 30–100 |
| Flue | Hydrocarbon vapours | 30–100 |
| *Condensers* | | |
| Aqueous vapours | Water | 1000–1500 |
| Organic vapours | Water | 700–1000 |
| Organics (some non-condensables) | Water | 500–700 |
| Vacuum condensers | Water | 200–500 |
| *Vaporisers* | | |
| Steam | Aqueous solutions | 1000–1500 |
| Steam | Light organics | 900–1200 |
| Steam | Heavy organics | 600–900 |

**Table 2.** Fouling factors (coefficients), typical values [19].

| Fluid | Coefficient (W/m$^2$°C) | Factor (resistance) (m$^2$°C/W) |
|---|---|---|
| River water | 3000–12,000 | 0.0003–0.0001 |
| Sea water | 1000–3000 | 0.001–0.0003 |
| Cooling water (towers) | 3000–6000 | 0.0003–0.00017 |
| Towns water (soft) | 3000–5000 | 0.0003–0.0002 |
| Towns water (hard) | 1000–2000 | 0.001–0.0005 |
| Steam condensate | 1500–5000 | 0.00067–0.0002 |
| Steam (oil free) | 4000–10,000 | 0.0025–0.0001 |
| Steam (oil traces) | 2000–5000 | 0.0005–0.0002 |
| Refrigerated brine | 3000–5000 | 0.0003–0.0002 |
| Air and industrial gases | 5000–10,000 | 0.0002–0.0001 |
| Flue gases | 2000–5000 | 0.0005–0.0002 |
| Organic vapours | 5000 | 0.0002 |
| Organic liquids | 5000 | 0.0002 |
| Light hydrocarbons | 5000 | 0.0002 |
| Heavy hydrocarbons | 2000 | 0.0005 |
| Boiling organics | 2500 | 0.0004 |
| Condensing organics | 5000 | 0.0002 |
| Heat transfer fluids | 5000 | 0.0002 |
| Aqueous salt solutions | 3000–5000 | 0.0003–0.0002 |

**Table 3.** Constants for use in equation 20 [19].

| Triangular pitch, $p_t = 1.25d_o$ | | | | | |
|---|---|---|---|---|---|
| No. passes | 1 | 2 | 4 | 6 | 8 |
| $K_1$ | 0.319 | 0.249 | 0.175 | 0.0743 | 0.0365 |
| $n_1$ | 2.142 | 2.207 | 2.285 | 2.499 | 2.675 |
| Square pitch, $p_t = 1.25d_o$ | | | | | |
| No. passes | 1 | 2 | 4 | 6 | 8 |
| $K_1$ | 0.215 | 0.156 | 0.158 | 0.0402 | 0.0331 |
| $n_1$ | 2.207 | 2.291 | 2.263 | 2.617 | 2.643 |

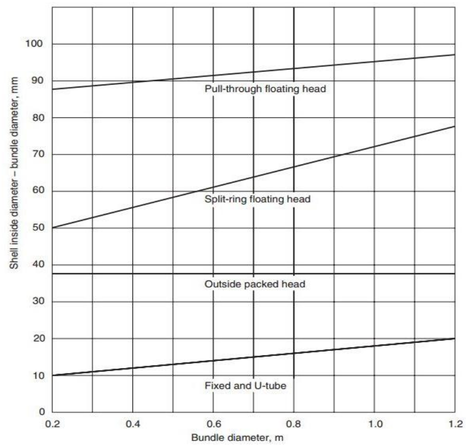


**Figure 19**. Shell-bundle clearance

JJMIE

Volume 9 Number 2, April.2015
ISSN 1995-6665
Pages 139 - 147

Jordan Journal of Mechanical and Industrial Engineering

# Computational Modeling of Temperature Field and Heat Transfer Analysis for the Piston of Diesel Engine with and without Air Cavity

Subodh Kumar Sharma* [a], Parveen Kumar Saini[b], Narendra Kumar Samria[c]

[a]*Research scholar, Department of Mechanical Engineering, National Institute of Technology Kurukshetra, Kurukshetra, INDIA*
[b]*Assistant Professor, Department of Mechanical Engineering, National Institute of Technology Kurukshetra, Kurukshetra, INDIA*
[c] *professor, Department of Mechanical Engineering, Banaras Hindu University, Varanasi, INDIA*

*Received 28 Jun 2014* *Accepted 24 April 2015*

**Abstract**

The present paper presents a theoretical study carried out to investigate the temperature field and heat transfer rate from the pistons of diesel engines with and without air cavity. The material was removed inside the piston, creating an air cavity. This cavity acts as an insulating medium which prevents the heat flow; thus, the need for providing insulation coating on piston crown is minimized. The main motive of this is to reduce the weight of the engine and the cost associated with thermal barrier coating. A detailed analysis was given for estimating the heat transfer rates to the cooling media and temperature field (isothermal distribution) in the piston body of water-cooled engines at different loads with and without air cavity. This analysis was done with numerical simulation models using FORTRAN programming. Results indicate that after creating an optimized air cavity in the piston, temperature, at all nodal point, decreases, which was presented in the form of contour bands and 4% of reduction in heat loss through piston, which leads to a better thermal efficiency. The FEA result provides effective theoretical evidence for further improving the pistons' performance. Additional benefits include protection of metal combustion chamber components from thermal stresses and reduced cooling requirements.



**Keywords:** *Combustion Chamber, Piston, Temperatures, Diesel Engine Components Temperature Field, Finite Elements*.

## Nomenclature

| | |
|---|---|
| $K_x, K_y, K_z$ | :Thermal conductivity in X, Y and Z direction respectively (W/m.K) |
| $q_E$ | : Heat conduction per unit volume (J/m$^3$) |
| $\rho$ | : Density of the material (kg m$^{-3}$) |
| $A^{(e)}$ | : Area of the Element (e) (m$^2$) |
| $V^{(e)}$ | : Volume of the Element (e) (m$^3$) |
| $C$ | : Specific Heat (W.Kg$^{-1}$.K$^{-1)}$ |
| $Ø$ | : Engine crank angle ($^o$CA) |
| $e$ | : Element Number (e) |
| $E$ | : Young's Modulus of Elasticity (N.m$^{-2}$) |
| $i, j, k$ | : Nodal Point Number of an element |
| $q_g$ | : Heat Generation per Unit Volume (J.m$^{-3}$) |
| $r_m$ | : Mean radius (m) |
| $r_{ij}$ | : Difference Between r Co-ordinates of Nodal Point i & j |
| $s_{ij}$ | : Distance between Nodal Points i & j |
| $N_s$ | : Shape factor |
| $T$ | : Temperature Variable (K) |
| $T_\alpha$ | : Surrounding Temperature (K) |
| $T_s$ | : Surface Temperature (K) |
| $H_c$ | : Convective heat transfer coefficient (W.m$^{-2}$.K$^{-1}$) |
| $\chi$ | : Variational Integral |
| $\chi_b$ | : Boundary Term of Variational Integral |
| $\chi_{bconv.}$ | : Variational Integral for convective boundary |
| $\chi_{bcont.}$ | : Variational Integral for contact boundary |
| $\chi_k^{(e)}$ | : Conductive matrix |
| $[k]^{(e)}$ | : Stiffness matrix |
| $\{t\}^{(g)}$ | : Global temperature |

## 1. Introduction

The present scenario of the energy crisis and the increasing requirement of internal combustion engines with heavy loads has made it necessary to find new ways of using petroleum fuel more efficiently in the internal combustion engine. To obtain high efficiency, fuel energy

* Corresponding author. e-mail: subodh_meet@yahoo.com.

is not to be wasted due to heat losses through combustion chamber components. One of the most changeling components for analysis is the piston due to its reciprocating motion. In the diesel engine, almost 30% of the fuel energy is wasted due to heat losses through combustion chamber components [1]. For an optimum design consideration of internal combustion engine, the knowledge of heat transfer rate from the working gases to the piston and from the wall of combustion chamber is of great importance. Heat transfer affects the thermodynamic performance of the engine and the result in thermal loading imposes a limit on the engine rating. For that reason, knowledge of the heat transfer in internal combustion engines is important to understand such systems [1, 2]. In addition, it is essential for the assurance of the stability of the engine components to avoid engine body distortions and to improve the engine design related to weight and auxiliary energy consumption. In the case of the engine piston, such knowledge is necessary to have a thorough understanding of heat flux, temperature and the distribution of these parameters. Engine heat transfer phenomena have been broadly analyzed for many decades [3-8]. Numerous mathematical models have been proposed including correlations based on dimensional analysis, which are widely accepted [7, 8]. In addition, Computational Fluid Dynamics (CFD) and/or Finite Element Method (FEM) codes, used for heat transfer simulations, require the assessment of this temperature to provide boundary conditions where convergence is attained through an iterative process [9, 10]. Furthermore, thermal analyses require the gas-side wall temperature to calculate temperature distribution and the thermo-mechanical behavior of components [11, 12]. Thermodynamic analysis of spark ignition engines is introduced by implementing temperature dependent specific heats [13, 19, 22]; it is found that the constant specific heat models can only be used for very small temperature variations so far large changes in temperature, variable specific heat models should be implemented. Understanding the temperature field in parts of internal combustion engine is most important in order to discover the points of highest thermal stress [14-18]. Further, a finite element model of gasoline spark engine was successfully developed and simulated and analyzed heat transfer during the combustion process, obtaining temperature distribution across the major engine component [20]. Temperature and the thermal stress field of the convention and ceramic coated piston of diesel engine were investigated by using the wavelet finite-element method, ANSYS software [21]. In addition, ceramic-coated pistons are being widely used in the internal combustion engine to improve the performance of the engine. This coating works as an insulating layer that reduces heat losses of the internal combustion engine and obtains higher efficiency. For a better performance and stress distribution over the whole combustion chamber components, the optimum coating thickness is found to be near 1 mm. It was also found that, with increasing the thickness of the coating, top surface temperature of the piston increased in a decreasing rate [22, 23]. During thermal cycling from room temperature to 1150°C, the thermal conductivity and diffusivity of TBC coating increase [24]. Other studies showed the effect of thermal barrier coatings on diesel engine performance of PZT loaded cyanate modified epoxy coated combustion chamber [25]. For instance, pistons are very important component in a diesel engine blast chamber due to their operational conditions. To improve the engine performance, most of the studies focused on heat transfer analysis with thermal barrier coated piston [26-29]. A new trend in the field of the internal combustion engine has been taken to make it adiabatic by creating an air cavity inside all the parts like cylinder wall, cylinder head and engine valves. By creating an air cavity inside the engine piston, the weight and cost associated with Thermal Barrier Coating (TBC) are minimized.

The specific objective of this paper is to predict the temperature field developed and the heat transfer rate through the diesel engine piston, considering the spatial variation of heat fluxes with and without the air-cavity and compare the behavior of the conventional (without air cavity) piston and piston with air cavity under thermal loading conditions. This approach is based on energy balances theory.

## 2. Statement of the Problem

Due to the depletion of energy at a tremendous rate, the present paper investigates the employing of air cavity inside the piston, which was found to be a good functional solution for the imminent lack of energy. So, this investigation is concerned with temperature distribution and heat transfer analysis in the piston (with and without air cavity) of the AV1 diesel engine, as shown in Figure 1. The engine is a single cylinder engine. The compression ratios and, consequently, the power and the torque are different. Selected technical data for the AV1 engine are provided in Table 1. The piston diameter is 75 mm and depth is 72 mm while the thickness of cavity in the piston is 4 mm and the height is 10 mm. The thickness of the piston ring is 10 mm. The thermo physical materials properties and heat transfer parameter for four different cases of engine loading of the piston are given in Tables 2 and 3. In Table 3, T and H represent the temperature and heat transfer coefficient; subscripts g, w and a represent the boundaries of the piston on the gas side (combustion chamber), water jacket side, and air side (crank case). Using the governing equation and the appropriate boundary conditions, the mathematical variational statement of the problem was obtained and then a 2-dimensional finite element model was formulated. With the help of these boundary conditions and finite element technique, temperature distribution and heat transfer analysis over the piston were analyzed by using FORTRAN programming. Figure 2 represents the meshed piston model with all the boundaries conditions.

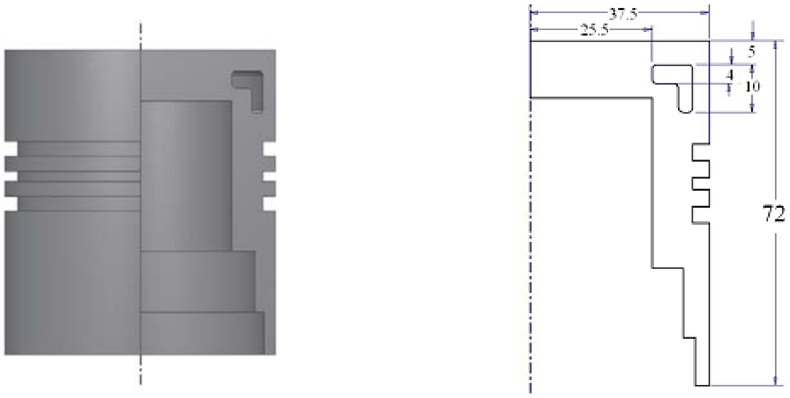


**Figure 1.** Model of Diesel Engine Piston

**Table 1**. Engine and their specification [26]

| **Specification** | **Type** | **Specification** | **Type** |
|---|---|---|---|
| Cooling | Water-Cooled Engine | Governing | Class"B1" |
| Model | AV1 | Power rating | 5 hp |
| No. of Cylinders | 1 | Fuel injection | Direct Injection |
| Cubic Capacity (ltr) | 0.553 | Rated Speed (rpm) | 1500 |
| Overall Dimensions of the standard engine | | 617 X 504 X 843 (L X B X H) | |

**Table 2.** Thermo physical properties of metal [26]

| **Sr. No.** | **Properties** | **Aluminium** | **Cast iron** | **Steel** |
|---|---|---|---|---|
| 1 | Thermal conductivity ($W.m^{-1}.K^{-1}$) | 175 | 70 | 50 |
| 2 | Density ($Kg.m^{-3}$) | 2700 | 7200 | 7850 |
| 3 | Thermal diffusivity ($m^2.hr^{-1}$) | 0.259 | 0.04563 | 0.044 |
| 4 | Specific Heat ($KJ.Kg^{-1}.K^{-1}$) | 0.8958 | 0.5860 | 0.4730 |

## 3. Boundary Condition at the Combustion Chamber Components

One of the most fundamental factors in temperature prediction at the combustion chamber components is the correct application of boundary conditions. This involves the ambient temperature and heat transfer coefficients at the various areas of the above components. The instantaneous values of heat transfer coefficient ($h_g$) and temperature ($t_g$) at combustion gas side is a function of crank angle (Ø) [2, 3, 5, 11, 17, 18]. Afterwards, the mean value of the heat transfer coefficient $H_g$ and the resulting gas temperature $T_g$ over the complete four-stroke engine cycle are calculated from the formulae given in Ref. [9,18] as:

$$Hg = \frac{1}{Ø0}\int_0^{Ø0} hg(Ø)dØ \qquad (1)$$

$$Tg = \frac{\int_0^{Ø0} hg(Ø)\mathrm{tg}(Ø)\mathrm{d}Ø}{\int_0^{Ø0} hg(Ø)\mathrm{d}Ø} \qquad (2)$$

In the present study, the following correlation, which was obtained by using the formula given by Eichelberg [9, 18], was used to predict instantaneous heat transfer coefficients. The instantaneous value of heat transfer coefficient $h_g$ (Ø) on the gaseous face at any crank angle (Ø) is obtained from the pressure-crank angle diagram as:

$$h_g (Ø) = 7.64(S)^{1.5}[P_g (Ø)\, T_g (Ø)]^{0.5}\ (W\, m^{-2}\, K^{-1}) \qquad (3)$$

where
$P_g$ ($\phi$) is gas pressure ($N/m^2$)
$T_g$ ($\phi$) is gas temperature (°C)
$S$ is mean piston speed (m/s)

In the thermal analysis, cycle averaged values of combustion heat transfer coefficient and combustion temperature were used for piston top. Temperature and heat transfer coefficient boundary conditions, for all the parts of the piston, were determined based on the authors' experience and on literature [18]. The thermal boundary conditions consist of applying a convection heat transfer coefficient and the bulk temperature, and they are applied to the piston crown, piston ring land sides, piston ring groove lands, and piston under crown surfaces. The temperature and heat transfer coefficients, in the combustion chamber in all the loading condition, were identified based on data provided in a previous research paper [13, 26]; they are presented in Table 3.The adopted heat transfer coefficient on the contact surfaces are $H_a$ (heat transfer coefficient at piston under crown surface) = 174.3 w/m$^2$k, *H1* (heat transfer coefficient at ring lands and piston skirt upper and lower side) = 290.54w/m$^2$k, *H2* (heat transfer coefficient at ring lands and piston skirt contact surfaces) = 20 w/m$^2$k, *H3* (heat transfer coefficient between piston rings and cylinder wall contact surfaces) = 38346 w/m$^2$k, *H4* (heat transfer coefficient between piston and cylinder wall contact surfaces) = 2324w/m$^2$k, $H_w$ (heat transfer coefficient through cylinder wall to water) = 1859.2w/m$^2$k, and temperature on water side ($T_w$) was 120$^{\circ}$C and on crank case side ($T_a$) it was 80$^{\circ}$C.

## 4. Finite Element Formulation of Heat Transfer Equations

The variational method constitutes a powerful approach to the formulation of an element relationship. In the theory of finite element analysis, first, the proper variational principle is selected and, then, the function involved is expressed in terms of approximate assumed displacements, which satisfies the given boundary conditions. Then, by minimizing the approximate function, a set of governing equations is developed for the whole piston body. Computer algorithm and FORTRAN program code are developed to solve these equations in order to find the unknown parameters, i.e., the temperature and the heat flow rate.

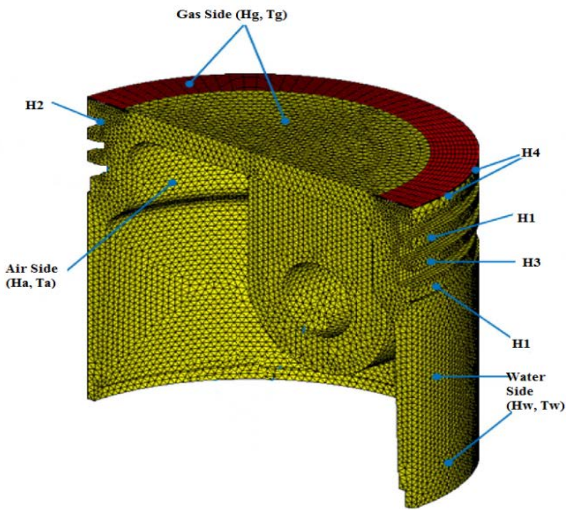


**Figure 2.** Meshed view of Piston Model

### *4.1. Heat Transfer Equation for Conduction*

The generalized governing differential equation for heat conduction can be represented as [1, 4]:

$$K\nabla^2 T + q_E - \rho C\frac{\partial T}{\partial t} = 0 \tag{4}$$

where,

$K$ – Thermal conductivity in X, Y and Z direction, respectively

$q_E$ – Heat conduction per unit volume

$\rho$ – Density of the material

$C$ – Heat transfer capacity of the material

And in cylindrical co-ordinates, three dimensional generalized governing differential equations for heat conduction with considering steady state and no internal heat generation can be represented as, Eq. (4) which can be written as:

$$\nabla^2 T = \frac{\partial^2 T}{\partial r^2} + \frac{1}{r}\left(\frac{\partial T}{\partial r}\right) + \frac{1}{r}\left(\frac{\partial^2 T}{\partial \theta^2}\right) + \frac{\partial^2 T}{\partial Z^2} = 0 \tag{5}$$

Let us consider that there are "*N*" numbers of nodal points having temperature $t_1$, $t_2$, $t_3$ …..$t_n$ whose values are to be determined by the finite element method. Here the principle of minimization is used in order to get the unknown temperatures. First, the variation integrals are differentiated with respect to the corresponding nodal points and equated to zero to yield the temperature at that point. Let us consider a triangular element having nodes *i*, *j*, *k* in anticlockwise direction. Assuming a linear polynomial equation of temperature can be represented as;

$$t^e = c_1 + c_2 r + c_3 z$$

Let $t_1$, $t_2$, $t_3$ and $(r_i, z_i)$, $(r_j, z_j)$, $(r_k, z_k)$ be the temperature and ($r$, $z$) co-ordinates of an element having nodes *i*, *j*, *k* , respectively.

The variational integral in axis symmetric co-ordinate system for heat conduction can be represented as:

$$\chi_K^{(e)} = \frac{1}{2}(2\pi K)\iint_A \left[[\frac{\partial t}{\partial r}]^2 + [\frac{\partial t}{\partial z}]^2\right] r dr dz \tag{6}$$

Here a linear polynomial is chosen to approximate the variation of temperature within an element in terms of the temperature at the nodal points of the elements. Polynomials are chosen in such a way that maintains continuity along the element boundaries. The shape function $N_i$, $N_j$ and $N_k$ are chosen for a particular element according to variations of the parameters within the elements. The Polynomial, chosen in terms of shape function, is given by in Eq. (7):

$$t(r,z) = [N_I \quad N_J \quad N_K]\begin{Bmatrix} t_i \\ t_j \\ t_k \end{Bmatrix} = [N]^{(e)}\{t\}^{(e)} \tag{7}$$

where the constants are

$$N_i = \frac{[a_i + b_i r + c_i z]}{\Delta} \quad ; N_j = \frac{[a_j + b_j r + c_j z]}{\Delta};$$

$$N_k = \frac{[a_k + b_k r + c_k z]}{\Delta}$$

$$a_i = (r_j z_k - z_j r_k),\ a_j = (r_k z_i - z_k r_i),$$

$$a_k = (r_i z_j - z_j r_i),$$

$$b_i = (z_j - z_k),\quad b_j = (z_k - z_i),\quad b_k = (z_j - z_i),$$

$$c_i = (r_k - r_j),\quad c_j = (r_i - r_k),\quad c_k = (r_j - r_i)$$

Differentiating the above equation (7) with respect to co-ordinates (*r*, *z*), which is shown in equation (8):

$$\frac{\partial t^{(e)}}{\partial r} = [b_i \quad b_j \quad b_k]\{t\}^{(e)} = [b]^{(e)}\{t\}^{(e)}$$

(8)

$$\frac{\partial t^{(e)}}{\partial z} = [c_i \quad c_j \quad c_k]\{t\}^{(e)} = [c]^{(e)}\{t\}^{(e)}$$

With the help of Eq. (8), the minimization of variational integral $\chi_K^{(e)}$ is carried out, which is shown in Eq. (9):

$$\chi_K^{(e)} = \frac{1}{2}(2\pi K)\iint_A \left[[[b]^2\{t\}^{\{e\}}]^2 + [[c]^2\{t\}^{(e)}]^2\right] rdrdz \quad (9)$$

**Table 3.** Heat transfer parameter for four different cases of engine loading [26]

| Parameter | Case 4 (Full Load) | Case 3 (3/4 Load) | Case 2 (Half Load) | Case 1 (No Load) |
|---|---|---|---|---|
| Temperature in °C | | | | |
| $T_g$ (Gas side) | 1000 | 800 | 600 | 400 |
| $T_w$ (Water side) | 120 | 120 | 120 | 120 |
| $T_a$ (Air side) | 80 | 80 | 80 | 80 |
| Heat transfer coefficients (Gas side, Water side, Air side) (W $m^{-2}$ $K^{-1}$) | | | | |
| $H_g$ (Gas side) | 290.5 | 232.4 | 174.3 | 116.2 |
| $H_w$ (water side) | 1859.2 | 1859.2 | 1859.2 | 1859.2 |
| $H_a$ (Air side) | 174.3 | 174.3 | 174.3 | 174.3 |
| Heat transfer coefficients between piston, ring and cylinder wall (W $m^{-2}$ $K^{-1}$) | | | | |
| $H_1$ | 290.5 | 290.5 | 290.5 | 290.5 |
| $H_2$ | 20.0 | 20.0 | 20.0 | 20.0 |
| $H_3$ | 38346.0 | 38346.0 | 38346.0 | 38346.0 |
| $H_4$ | 2324.0 | 2324.0 | 2324.0 | 2324.0 |

By simplifying the above equation and using delta operator function, Eq. (9) can be rewrite as:

$$\frac{\partial \chi_k^{(e)}}{\partial \{t\}^{(e)}} = \left(2\pi K A^{(e)} r_c\right)\left[[b]^{(e)^t}[b]^{(e)}\right] + \left[[c]^{(e)^t}[c]^{(e)}\right]\{t\}^{(e)} \quad (10)$$

where

$$\iint_A rdrdz = A^{(e)} r_c \quad r_c\,(mean\ radius) = \frac{r_i + r_j + r_k}{3}$$

Let $A^{(e)}\, r_c = V^{(e)}$; where $V^{(e)}$ is the volume of an element.

After putting the value of $[b]^{(e)}$, $[b]^{(e)t}$, $[c]^{(e)}$ and $[c]^{(e)t}$ in equation (10), generate the stiffness matrix:

$$\frac{\partial \chi_k^{(e)}}{\partial \{t\}^{(e)}} = \left(2\pi K V^{(e)}\right)\left[\begin{Bmatrix} b_i \\ b_j \\ b_k \end{Bmatrix}[b_i \quad b_j \quad b_k] + \begin{Bmatrix} c_i \\ c_j \\ c_k \end{Bmatrix}[c_i \quad c_j \quad c_k]\right]\{t\}^{(e)} \quad (11)$$

After solving the above equation, the conductive matrix becomes:

$$\frac{\partial \chi_k^{(e)}}{\partial \{t\}^{(e)}} = \left[\begin{bmatrix} k_{11} & k_{12} & k_{13} \\ k_{21} & k_{22} & k_{23} \\ k_{31} & k_{32} & k_{33} \end{bmatrix}\right]\begin{Bmatrix} t_i \\ t_j \\ t_k \end{Bmatrix} = [k]^{(e)}\{t\}^{(e)} \quad (12)$$

where $[k]^{(e)} = \text{stiffness matrix}$

### 4.2. Heat Transfer Equation for Contact Boundary

The generalized governing differential equation for contact boundary can be represented as [4]:

$$q_c = K_1\left[\frac{\partial T}{\partial n}\right]^e = -K_2\left[\frac{\partial T}{\partial n}\right]^p \quad (13)$$

where $q_c = h_c(T^e - T^p)$ (14)

Variational formulation for contact boundary between 2 elements (*e*) and (*p*) can be written as:

$$\chi_{bcont\,.} = \frac{h_c}{2}\int_{si}^{sj} [\{t\}^e - \{t\}^p]^2\, 2\pi r ds \quad (15)$$

Solving it further in a similar fashion as done in the conductive boundary, it was found that the contact boundary variational integral of heat transfer after differentiation, with respect to temperature of contact surface that yields a set of linear equations, to be a contribution to the global set of equation:

$$\frac{(\partial \chi_{bcont\,.})e}{\partial \{t_s\}^e} = \frac{2\pi h_c r_m r_{ij}}{6\cos\theta}\begin{bmatrix} 2 - \frac{\varepsilon}{2} & 1 \\ 1 & 2 + \frac{\varepsilon}{2} \end{bmatrix} * \begin{Bmatrix} \{\{t_s\}^e - \{t_s\}^p\}_1 \\ \{\{t_s\}^e - \{t_s\}^p\}_2 \end{Bmatrix} \quad (16)$$

### 4.3. Heat Transfer Equation for Convective Boundary

The generalized governing differential equation for heat convection can be represented as [4]:

$$-K\left(\frac{\partial T}{\partial n}\right) = h(T - T_\infty) \quad (17)$$

The variational formulation for convective boundary can be represented as:

$$\delta\chi_{bconv\,.} = \int_A -K\left(\frac{\partial T}{\partial n}\right)\delta T dS = \int_A h(T - T_\infty)\,\delta T dS \quad (18)$$

$$\delta\chi_{bconv\,.} = \int_i^j -Kr\left(\frac{\partial T}{\partial n}\right)\delta T dS \quad (19)$$

where, *i* and *j* are the two nodal points of the element of side *s*.

Let

$$\frac{r}{s} = cos\,\theta\,, \qquad \left(\frac{\partial T}{\partial n}\right) = h(t - t_\infty)\ and\ ds = \frac{dr}{cos\,\theta}$$

$$T(s) = N_{si}\,t_i + N_{sj}\,t_j = [N_s]\{t\} \tag{20}$$

where $N_{si}$ and $N_{sj}$ are the shape factor.

$$N_{si} = \frac{s_j - s}{s_{ij}} = \frac{\frac{(r_j - r)}{cos\,\theta}}{\frac{r_{ij}}{cos\,\theta}} = \frac{(r_j - r)}{r_{ij}} \tag{21}$$

$$N_{sj} = \frac{s - s_i}{s_{ij}} = \frac{\frac{(r - r_i)}{cos\,\theta}}{\frac{r_{ij}}{cos\,\theta}} = \frac{(r - r_i)}{r_{ij}} \tag{22}$$

With the help of Eqs. (20), (21) and (22), the minimization of variational integral for convective boundary can be represent as:

$$\frac{\partial \chi_{bconv.}}{\partial\{t_s\}} = \frac{2\pi h}{cos\,\theta}\int_i^j ([N_s]^T[N_s]\{t\})\,rdr - \frac{2\pi h t_\infty}{cos\,\theta}\int_i^j ([N_s]^T)\,rdr \tag{23}$$

$$\frac{\partial \chi_{bconv.}}{\partial\{t_s\}} = \frac{2\pi h r_m r_{ij}}{6cos\,\theta}\begin{bmatrix} 2 - \frac{\varepsilon}{2} & 1 \\ 1 & 2 + \frac{\varepsilon}{2} \end{bmatrix}\begin{Bmatrix} t_{si} \\ t_{sj} \end{Bmatrix} - \begin{Bmatrix} (ht_\infty)_1 \\ (ht_\infty)_2 \end{Bmatrix} \tag{24}$$

where,

$$r_m = \frac{r_i + r_j}{2}, r_{ij} = r_j - r_i\,, r_j = r_m - \frac{r_{ij}}{2}\,, \varepsilon = \frac{r_{ij}}{r_m}$$

$$\frac{\partial \chi_{bconv.}}{\partial\{t_s\}} = [H]_s\{t\}_s - \{ht_\infty\} \tag{25}$$

## 5. Temperature Field Calculations

The prediction of the temperature distribution in the piston involves the solution of the heat conduction, contact and convection equation with the appropriate boundary conditions. For this purpose, the finite-element model of piston was considered. These models give satisfactory results with a significant computer time economy.

We can develop the variational integral of heat transfer globally with the help of equations (12), (16) and (25), which represent in equation (26).

$$\frac{\partial\{X\}^g}{\partial\{t\}^g} = [K]^g\{t\}^g + [H]^g\{t\}^g - \{ht_\infty\}^g = 0 \tag{26}$$

where, $\partial\{X\}^g$=Variational integral of heat transfer globally

Let

$$[K]^{(g)} + [H]^g = [D]^g$$

$$\{ht_\infty\}^{(g)} = \{V\}^{(g)}$$

Thus

$$[D]^{(g)}\{t\}^{(g)} = \{V\}^{(g)} \tag{27}$$

$$\{t\}^{(g)} = [DI]^{(g)}\{V\}^{(g)} \tag{28}$$

where

$$[DI]^{(g)} = [D]^{(g)^{-1}},\ \{t\}^{(g)} = \ global\ temperature$$

The solution of the reduced steady-state heat conduction problem in the *r*, *z* coordinate system is found through sub-dividing the piston into a number of elements and nodes. Every element exists in thermal equilibrium with its neighboring elements. After formulating the heat transfer equations, a computational code to solve the mathematical model through FORTRAN language is generated, and the temperature at all the nodes is found. Then the temperature field (isothermal distribution curve) in the diesel engine piston model is obtained.

## 6. Discussion of Results

As results indicate, the thermal energy is much more utilized to generate work output due to air cavity. It reduces the weight and cost of the piston because the cost associated with thermal barrier coating is reduced on the piston crown. This new method should be supported by research comprising the application of thermodynamic principles and the fundamental equations of heat transfer. Here, the finite element analysis is used to obtain temperature at all the nodal points. The results of calculations carried out are presented in Figures 3-7. Figures 3-6 show the temperature field (isothermal distribution) and Figure 7 shows the heat flow rate through the piston under four different engine thermal loading conditions having gas temperatures of 1000°C, 800°C, 600°C and 400°, respectively, with and without air cavity. The continuous lines show the temperature field and the heat flow rate for conventional piston, while the dotted lines show the temperature field and the heat flow rate for the case when there is an air cavity inside the piston. The maximum and minimum temperature values are determined as 449°C and 110°C at the top and bottom surface of conventional piston bowl, respectively. And in air cavity piston, the maximum and minimum temperature values are determined as 464°C and 111°C at the top and bottom surface of the piston bowl, as shown in Table 4. Movement of the maximum temperature from the piston top surface to the bottom surface of the piston is attributed to the fact that the top surface has a relatively larger heat transfer coefficient as compared to the bottom surface. Since the inner side surface of the piston was voided circumferentially with a relatively very low conduction coefficient material, i.e., air, so heat transfer was reduced considerably to it. Therefore, the top surface temperature, as observed, was high as compared to the conventional piston. The maximum surface temperature of the base metal of the cavity piston is seen to be 464°C. It, as shown, increases the combustion chamber temperature of the engine. The comparison shows that there is a tendency to decrease the heat flow rate in the air cavity piston body.

To check the validity of the heat transfer model, the heat balance approached was adopted. According to the principle of the conversion of energy, at a steady state condition, the heat entering to the piston from gas side is equal to the heat lost to water and air. It was found that the temperature, at all the nodal points, was accurate as they are satisfying heat flow boundary conditions. Hence, the results are meaningful. Initially, the piston was heated at a much higher rate, as the temperature was less. Gradually, the temperature increases and as a result of this the heat input to it decreases till the steady state condition is reached as shown in Figure 7. Figure 7 shows the variation in heat gain by the piston from hot gases ‘Qg’, heat lost to cooling water ‘Qw’ and heat lost to air ‘Qa’ under four different engine thermal loading conditions, for both cases with and without air cavity in the diesel piston. It seems that piston received the heat from hot gases, which increases with the increase in the engine loads. Similarly, the heat lost to water, and heat lost to air, also increases with the increase in engine loads, as shown in Table 5. In Figure 7, it can be observed that the error is very small between the heat supplied (Qg) by the combustion gasses and the heat rejected to water (Hw) and air sides (Ha). It represents a uniform percentage throughout all the tests. As expected, for steady state conditions, the heat transfer rate increases with engine loading condition, with a maximum observed at full load. Here, in the present analysis, the heat balance equation is satisfied for all the different loading conditions. So it presumed that the obtained temperature field and heat flow rate are accurate as they are satisfying heat flow boundary conditions. Hence, the results are meaningful. The influence of air cavity is shown by the fact that the temperature variation in the piston is reduced by the application of this cavity. Hence, the air cavity plays an important role in reducing the temperature levels of the piston and, thus, reduces the thermal stresses, reduces the heat loss through the piston and improves the work output.

**Table 4.** Maximum and minimum temperature in the engine piston

| | Conventional Piston | | Air-cavity piston | |
|---|---|---|---|---|
| | Max. Temp. (°C) | Min. Temp. (°C) | Max. Temp. (°C) | Min. Temp. (°C) |
| Case 1 (No Load) | 463.769 | 111.227 | 449.689 | 111.288 |
| Case 2 (Half Load) | 345.378 | 110.760 | 335.352 | 110.798 |
| Case 3 (3/4 Load) | 261.291 | 110.434 | 254.831 | 110.459 |
| Case 4 (Full Load) | 188.850 | 110.155 | 185.738 | 110.170 |

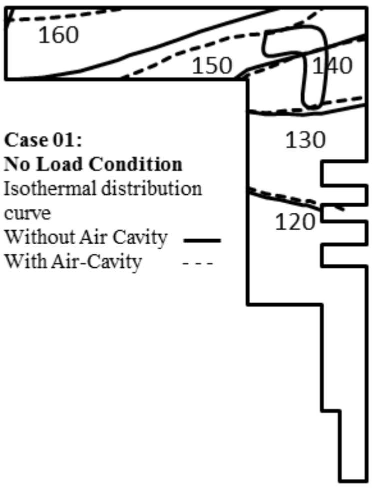


**Figure 3.** Temperature field at no load

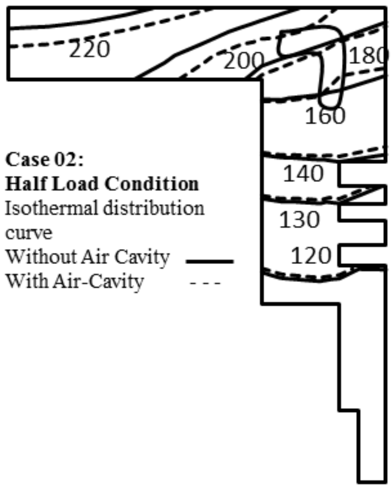


**Figure 4.** Temperature field at 1/2 load

 

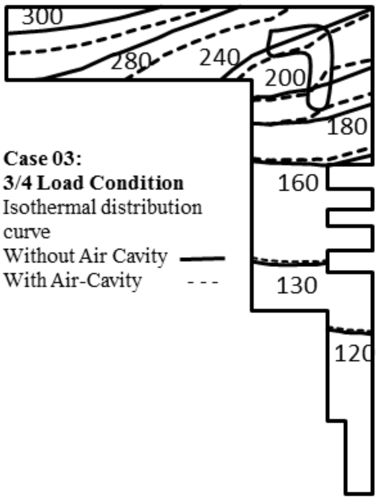


**Figure 5.** Temperature field at 3/4 load

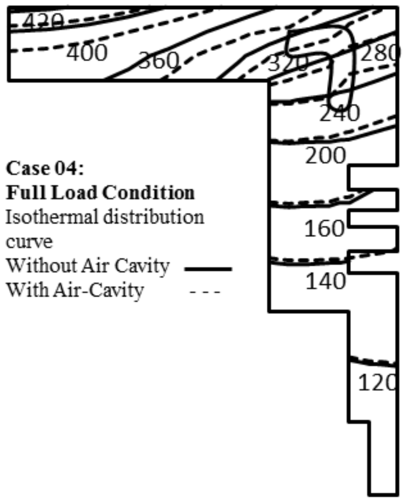


**Figure 6.** Temperature field at full load

**Table 5.** heat flow rates through piston with gas temperature

| Heat Flow rate (kW/Hr) | Conventional Piston (Without air cavity) | | | | Air-cavity piston | | | |
|---|---|---|---|---|---|---|---|---|
| | No Load | Half Load | 3/4 Load | Full Load | No Load | Half Load | 3/4 Load | Full Load |
| $Q_g$ | 5.094 | 9.797 | 15.341 | 23.417 | 5.298 | 10.179 | 15.924 | 24.354 |
| $Q_a$ | 2.605 | 3.282 | 4.072 | 5.198 | 2.708 | 3.407 | 4.231 | 5.406 |
| $Q_w$ | 2.489 | 6.515 | 11.268 | 18.219 | 2.588 | 6.762 | 11.707 | 18.945 |

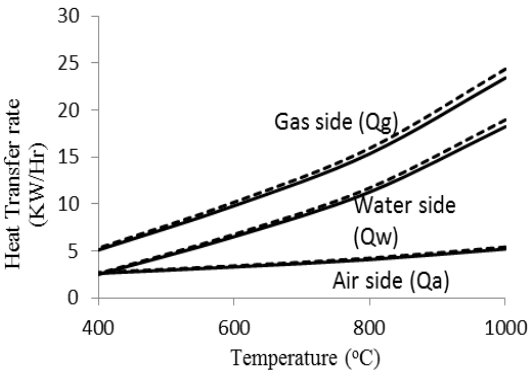


**Figure 7.** Variation of the heat flow rates through piston with gas temperature

## 7. Conclusion

The present study indicates that an air cavity applied in the piston has the following effects:

- It decreases the overall body temperature of the piston. The values of temperature and thus thermal stress will further decrease by increasing the cavity thickness up to a certain limit.
- By the application of this cavity in the piston, the reduction in heat loss through the piston is found to be nearly 4%. The percentage distribution of heat loss through cooling media remains unaffected at low loads while it is significantly affected at high loads.

The temperature and heat transfer are obtained by indirect evaluation of the boundary conditions of the piston. The variational integral method in FEM presented here may be used for other parts of I.C. engines, such as the inlet and exhaust valves, cylinder heads, etc. This method is a powerful tool for the design engineer when used in the early stages of the design of a semi-adiabatic engine. In development work, it enables the development engineer to narrow the range of the experimental work and thus save considerable time and expense.

## References

[1] H. Yasar, H.S. Soyhan, H. Walmsley, B. Head, C. Sorusbay, “Double-Wiebe function: an approach for single-zone HCCI engine modeling”. Applied Thermal Engineering, Vol. 28 (2008), 1284-1290.

[2] R. Stone, “Introduction to Internal Combustion Engines”. New York: Macmillan; 1999.

[3] C. F. Taylor, T. Y. Toong, “Heat transfer in internal-combustion engines”. ASME paper 57-HT-17 (1957).

[4] G. A. Woschni, “Universally applicable equation for the instantaneous heat transfer coefficient in the internal combustion engine”. SAE 670931 (1967).

[5] G. F. Hohenberg, “Advanced approaches for heat transfer calculation”. SAE 790825 (1979).

[6] J. Chang, O. Guralp, Z. Filipi, D. Assanis, T. Kuo, P. Najt, R. Rask, "New heat transfer correlation for an HCCI engine derived from measurements of instantaneous surface heat flux". SAE 2004-01-2996 (2004).

[7] G. Borman, K. Nishiwaki, "Internal combustion engine heat transfer". Progress in Energy and Combustion Science, Vol. 13 (1987) No. 1, 1-46.

[8] P. Tamilporai, N. Baluswamy, P.M. Jawahar, S. Subramaniyam, S. Chandrasekaran, K. Vijayan, S. Jaichandar, J. R. Janci, K. Arunachalam, "Simulation and analysis of combustion and heat transfer in low heat rejection diesel engine using two zone combustion model and different heat transfer models". SAE 2003-01-1067 (2003).

[9] V. Esfahanian, A. Javheri, M. Ghaffarpour, "Thermal analysis of an SI engine piston using different combustion boundary condition treatments". Applied Thermal Engineering, Vol. 26 (2006), 277-287.

[10] A. Jafari, S. K. Hannani, "Effect of fuel and engine operational characteristics on the heat loss from combustion chamber surfaces of SI engines". International Communications in Heat and Mass Transfer, Vol. 33 (2006) No. 1, 122-134.

[11] I. Taymaz, "An analysis of residual stresses in thermal barrier coatings: a FE performance assessment". Plasma Processes and Polymers, Vol. 6 (2009), 599-604.

[12] E. Buyukkaya, M. Cerit, "Thermal analysis of a ceramic coating diesel engine piston using 3-D finite element method". Surface and Coatings Technology, Vol. 202 (2007) No. 2, 398-402.

[13] E. Abu-Nada, I. Al-Hinti, A. Al-Sarkhi, B. Akash, "Thermodynamic modeling of spark-ignition engine: Effect of temperature dependent specific heats". International Communication in Heat and Mass Transfer, Vol. 33 (2006), 1264–1272.

[14] R. Soltani, H. Samadi, E. Garcia, T. W. Coyle, "Development of alternative thermal barrier coatings for diesel engines". SAE International, Vol. 01 (2005), 65-72.

[15] J. B. Heywood, "Internal Combustion Engine Fundamentals". McGraw-Hill Inc New York, 1988.

[16] C. D. Rakopoulos, K. A. Antonopoulos, D. C. Rakopoulos, E. G. Giakoumis, "Investigation of the temperature oscillations in the cylinder walls of a diesel engine with special reference to the limited cooled case". International Journal of Energy Research, Vol. 28 (2004), 977–1002.

[17] Ravindra Prasad and N. K. Samria, "Transient Heat Transfer Studies on a diesel engine valve". International Journal of Mechanical Science, Vol. 33 (1991), 179-195.

[18] David R. Buttsworth, A. Agrira, R. Malpress, T. Yusaf, "Simulation of instantaneous heat transfer in spark ignition internal combustion engines: Unsteady thermal boundary layer modeling". Journal of Engineering for Gas Turbines and Power, Vol. 133 (2011), 45-56.

[19] A. Mohammadi, M. Yaghoubi, "Estimation of instantaneous heat transfer coefficient in spark-ignition engines". International Journal of Thermal Science, Vol. 49 (2010), 1309-1317.

[20] T. T. Mon, R. Mamat, Kamsah Nazri, "Thermal analysis of SI Engine using simplified finite element model". World Congress on Engineering, London, U.K., Vol. 3 (2011), 66-71.

[21] B. Zhao, "Thermal stress analysis of ceramic coated diesel engine piston based on the wavelet finite element method". Journal of Engineering Mechanics, Vol. 138 (2012), 166-172.

[22] A. Al-Sarkhi, B. Akash, E. Abu-Nada, and I. Al-Hinti, "Efficiency of Atkinson Engine at Maximum Power Density using Temperature Dependent Specific Heats". Jordan Journal of Mechanical and Industrial Engineering, Vol. 2 (2008), 71-75.

[23] Muhammet Cerit, "Thermo mechanical analysis of a partially ceramic coated piston used in an SI engine". Surface Coating & Technology, Vol. 205 (2011), 3499–3505.

[24] Tyler R. Kakuda, Andi M. Limarga, T. D. Bennett and David R. Clarke, "Evolution of thermal properties of EB-PVD 7YSZ thermal barrier coating with thermal cycling". Acta Material, Vol. 57 (2009), 2583-2591.

[25] K. R. Vijaya Kumar, V. Sundareswaran, "The Effect of Thermal Barrier Coatings on Diesel Engine Performance of PZT Loaded Cyanate Modified Epoxy Coated Combustion Chamber". Jordan Journal of Mechanical and Industrial Engineering, Vol. 5 (2011) No. 5, 403-406.

[26] S. K. Sharma, P. K. Saini, N. K. Samria, "Experimental thermal analysis of diesel engine piston and cylinder wall". Journal of engineering, Article ID 178652 (2015), 1- 10.

[27] Ravindra Prasad, N. K. Samria, "Heat transfer and stress fields in the inlet and exhaust valve of a semi-adiabatic diesel engine". Computer Structure, Vol. 34 (1990), 165-711.

[28] V. P. Singh, P. C. Upadhyay, N. K. Samria, "Some heat transfer studies on a diesel engine piston". International Journal of Heat & Mass Transfer, Vol. 29 (1986), 812-814.

[29] Ravindra Prasad, N. K. Samria, "Transient heat transfer analysis an internal combustion engine piston". Computer Structure, Vol. 34 (1990), 781-193.

[30] S. K. Sharma, P. K. Saini, N. K. Samria, "Modelling and analysis of radial thermal stresses and temperature field in diesel engine valves with and without air cavity". International Journal of Engineering, Science and Technology, Vol. 5 (2013) No. 3, 111-123.

JJMIE

Volume 9 Number 2, April.2015
ISSN 1995-6665
Pages 149 - 157

Jordan Journal of Mechanical and Industrial Engineering

# Heatline Visualization of Buoyancy-Driven Flow inside a Nanofluid-Saturated Porous Enclosure

Iman Zahmatkesh*

*Department of Mechanical Engineering, Mashhad Branch, Islamic Azad University, Mashhad, Iran*

*Received 15 Jan 2015* *Accepted 27 April 2015*

**Abstract**

In the present paper, the heatline visualization technique is utilized to understand heat transport path for buoyancy-driven flow inside a rectangular porous enclosure saturated with nanofluids. For this purpose, the mass, momentum and energy conservation equations are solved numerically adopting a control-volume based computational procedure. Moreover, the dimensionless heat function equation is utilized to determine the heat flow pattern inside the enclosure. Computations are undertaken for Cu, $Al_2O_3$, and $TiO_2$ nanoparticles in the base fluid of water and corresponding results in terms of dimensionless distributions of streamlines, isothermal lines, and heatlines as well as numerical values for flow strength and the average Nusselt number are compared with those of pure water under different Darcy-Rayleigh numbers. Additionally, the consequences of the nanoparticle fraction and the enclosure aspect ratio on the buoyancy-driven flow are analyzed. Inspection of the presented results indicates that among Cu-water, $Al_2O_3$-water, and $TiO_2$-water nanofluids, the Cu-water one produces higher heat transfer rates that is attributed to higher thermal conductivity of the Cu nanoparticles.



**Keywords:** *Nanofluid, Porous Media, Buoyancy-Driven Flow, Heatline, Enclosure*.

**Nomenclature**

| | |
|---|---|
| *AR* | aspect ratio of the enclosure |
| *Cv* | constant-pressure specific heat |
| *Da* | Darcy number |
| *g* | gravitational acceleration |
| *h* | heat function |
| *H* | enclosure height |
| *k* | thermal conductivity |
| *K* | medium permeability |
| *L* | enclosure length |
| *Nu* | local Nusselt number |
| $\overline{Nu}$ | average Nusselt number |
| *Ra* | Darcy-Rayleigh number |
| *T* | temperature |
| *u,v* | velocity components in x- and y-directions |
| *x,y* | Cartesian coordinates |
| *X,Y* | dimensionless coordinates |

**Greek symbols**

| | |
|---|---|
| $\alpha$ | thermal diffusivity |
| $\beta$ | thermal expansion coefficient |
| $\theta$ | dimensionless temperature |
| $\mu$ | dynamic viscosity |
| $\pi$ | dimensionless heat function |
| $\rho$ | density |
| $\phi$ | nanoparticle fraction |
| $\psi$ | stream function ($m^2$s-1) |
| $\Psi$ | dimensionless stream function |

**Subscripts**

| | |
|---|---|
| *bf* | base fluid |
| *C* | cold |
| *nf* | nanofluid |
| *p* | nanoparticle |

## 1. Introduction

Recent years have witnessed extensive research on convective heat transfer of nanofluids in the view of their abnormally better thermophysical properties. Thereby, it is not surprising to see some previous interests on the analysis of buoyancy-driven flow inside nanofluid-saturated porous enclosures. Sun and Pop [1], Chamkha and Ismael [2], Ahmed *et al.* [3], Rashidi *et al.* [4],

* Corresponding author. e-mail: zahmatkesh5310@mshdiau.ac.ir.

Bourantas *et al.* [5], Sheremet *et al.* [6], and Nguyen *et al.* [7] contributed some important findings in this field.

In spite of this, all the previous investigations on nanofluid-saturated porous enclosures were based on streamlines and isotherms. Although streamlines can adequately explain fluid flow, isotherms may not be sufficient for heat transfer analysis since heat flux lines are non-orthogonal to isotherms in a convection dominant regime. A more vigorous mean for the visualization of heat transfer in a two-dimensional convective transport process is provided by the distribution of heatlines. The concept of heatlines was introduced by Kimura and Bejan [8] as the trajectories of flow of heat energy and its use for visualization purposes is increasing (e.g., Saleh and Hashim [9-10], Basak *et al.* [11], and Rahman *et al.* [12]). The heatline visualization technique can be employed to observe not only path of heat flow but also intensity of heat flux at any location of domain for a convection heat transfer problem.

The objective of the present study is to visualize heat and fluid flow inside a nanofluid-saturated porous enclosure. For this purpose, streamlines, isothermal lines, and heatlines are obtained and plotted for enclosures saturated with Cu-water, $Al_2O_3$-water, or $TiO_2$-water nanofluids with different nanoparticle fractions, Darcy-Rayleigh numbers, and enclosure aspect ratios. Moreover, variations of the flow strength and the average Nusselt number with these parameters are presented. Based on the performed literature survey, this is the first study on the application of heat function on buoyancy-driven flows inside nanofluid-saturated porous enclosures.

## 2. Mathematical Formulation

An isotropic, homogenous, nanofluid-saturated porous enclosure is considered here with water as the base fluid. Figure 1 displays a schematic representation of this enclosure. Here, the left wall is heated and the right wall is cooled. Meanwhile, the horizontal walls are thermally insulated. The established flow is considered incompressible, Newtonian, and laminar. It is assumed that Local Thermal Equilibrium (LTE) exists between the nanofluid and the porous medium. The LTE is also assumed between the nanoparticles and the base fluid. The former is assumed here to be made up of Cu, $Al_2O_3$, or $TiO_2$. Except for the density in the body force term in the momentum equation for which the Oberbeck-Boussinesq approximation is adopted, thermophysical properties of the nanoparticles and the base fluid are kept constant with the numerical values reported in Table 1. The Darcy model, which assumes proportionality between velocity and pressure gradient, is used here to simplify the momentum equations. This model has been extensively used to study a number of fluid mechanics and heat transfer problems associated with fluid-saturated porous media (e.g., Duwairi *et al.* [13], Rashidi *et al.* [14]). With these assumptions, governing equations for continuity, momentum, and energy take the form of:

$$\frac{\partial u}{\partial \mathrm{x}}+\frac{\partial v}{\partial \mathrm{y}}=0, \tag{1}$$

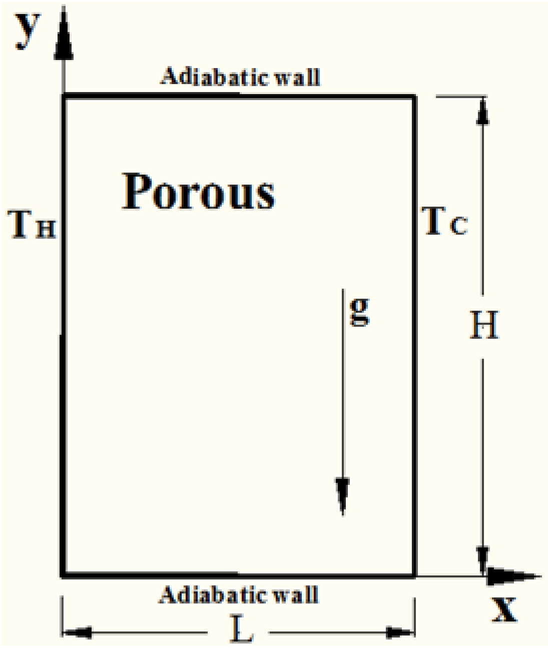


**Figure 1.** Schematic representation of the porous enclosure.

**Table 1.** Thermophysical properties of the nanoparticles and the base fluid at 300K.

| Material | $C_p$ $(Jkg^{-1}K^{-1})$ | $\rho$ $(kgm^{-3})$ | $k$ $(Wm^{-1}K^{-1})$ | $\beta\times10^{-5}$ $(K^{-1})$ |
|---|---|---|---|---|
| Pure water | 4179 | 997.1 | 0.613 | 21 |
| Copper (Cu) | 385 | 8933 | 401 | 1.67 |
| Alumina ($Al_2O_3$) | 765 | 3970 | 40 | 0.85 |
| Titanium oxide ($TiO_2$) | 686.2 | 4250 | 8.9538 | 0.9 |

$$u=-\frac{K}{\mu_{nf}}\frac{\partial p}{\partial x}, \tag{2}$$

$$\begin{aligned} v=\frac{Kg}{\mu_{nf}}\big[&\phi\rho_p\beta_p+(1-\phi)\rho_f\beta_f \\ &-\phi(1-\phi)(\rho_p-\rho_f)(\beta_p \\ &-\beta_f)\big](T-T_C)-\frac{K}{\mu_{nf}}\frac{\partial p}{\partial y}, \end{aligned} \tag{3}$$

$$u\frac{\partial T}{\partial x}+v\frac{\partial T}{\partial y}=\alpha_{nf}\left(\frac{\partial^2 T}{\partial x^2}+\frac{\partial^2 T}{\partial y^2}\right) \tag{4}$$

Here, $x$ and $y$ are the Cartesian coordinates while $u$ and $v$ are the velocity components in the $x$- and $y$-directions, respectively. $T$ is the temperature, $K$ is the medium permeability, $p$ is the pressure, $\rho$ is the density, $\mu$ is the dynamic viscosity, $\beta$ is the thermal expansion coefficient, $\alpha$ is the effective thermal diffusivity, and $\phi$ is the nanoparticle fraction. In the equations above, the subscripts $p$, $f$, and $nf$ stand for the nanoparticles, the base fluid, and the nanofluid, respectively.

The effective dynamic viscosity of the nanofluid is calculated from the Brinkman model [15]:

$$\mu_{nf} = \frac{\mu_f}{(1-\phi)^{2.5}}, \tag{5}$$

while the Maxwell-Garnetts model [16] is employed for the effective thermal conductivity:

$$\frac{k_{nf}}{k_f} = \frac{(k_p + 2k_f) - 2\phi(k_f - k_p)}{(k_p + 2k_f) + \phi(k_f - k_p)} \tag{6}$$

The effective thermal diffusivity of the nanofluid is defined as:

$$\alpha_{nf} = \frac{k_{nf}}{\rho_{nf}\, c_{p,nf}}, \tag{7}$$

with the heat capacitance of the nanofluid being in the form of:

$$\rho_{nf}\, c_{p,nf} = (1-\phi)\rho_f c_{p,f} + \phi\rho_p c_{p,p}. \tag{8}$$

Eliminating pressure terms in the momentum equations by applying cross-differentiation yields:

$$\frac{\partial u}{\partial y} - \frac{\partial v}{\partial x} = -\frac{Kg}{\mu_{nf}}\left[\phi\rho_p\beta_p + (1-\phi)\rho_f\beta_f - \phi(1-\phi)(\rho_p - \rho_f)(\beta_p - \beta_f)\right]\frac{\partial T}{\partial x}. \tag{9}$$

Introducing stream function (i.e.,$\psi$) as:

$$u = \frac{\partial \psi}{\partial y}, v = -\frac{\partial \psi}{\partial x}, \tag{10}$$

automatically satisfies the continuity equation. Moreover, equations (4) and (9) take the form of

$$\frac{\partial^2 \psi}{\partial x^2} + \frac{\partial^2 \psi}{\partial y^2} = -\frac{Kg}{\mu_{nf}}\left[\phi\rho_p\beta_p + (1-\phi)\rho_f\beta_f - \phi(1-\phi)(\rho_p - \rho_f)(\beta_p - \beta_f)\right]\frac{\partial T}{\partial x} \tag{11}$$

and

$$\frac{\partial \psi}{\partial y}\frac{\partial T}{\partial x} - \frac{\partial \psi}{\partial x}\frac{\partial T}{\partial y} = \alpha_{nf}\left(\frac{\partial^2 T}{\partial x^2} + \frac{\partial^2 T}{\partial y^2}\right) \tag{12}$$

To obtain dimensionless governing equations, the following dimensionless variables are defined:

$$X = \frac{x}{L}, Y = \frac{y}{H}, AR = \frac{H}{L}, \Psi = \frac{\psi}{\alpha_f},$$
$$\Theta = \frac{T - T_C}{T_H - T_C}, Ra = \frac{Kg\rho_f\beta_f(T_H - T_C)H}{\mu_f\alpha_f} \tag{13}$$

Here, $AR$ is the enclosure aspect ratio and $Ra$ is the Darcy-Rayleigh number.

Substituting equation (13) into equations (11) and (12) yields:

$$\frac{\partial^2 \Psi}{\partial X^2} + \frac{\partial^2 \Psi}{\partial Y^2} = -Ra(1-\phi)^{2.5}\left[(1-\phi) + \phi\left(\frac{\rho_p}{\rho_f}\right)\left(\frac{\beta_p}{\beta_f}\right) - \phi(1-\phi)\left(\frac{\rho_p}{\rho_f} - 1\right)\left(\frac{\beta_p}{\beta_f} - 1\right)\right]\frac{\partial \Theta}{\partial X} \tag{14}$$

$$\frac{\partial \Psi}{\partial Y}\frac{\partial \Theta}{\partial X} - \frac{\partial \Psi}{\partial X}\frac{\partial \Theta}{\partial Y} = \frac{\alpha_{nf}}{\alpha_f}\left[AR\frac{\partial^2 \Theta}{\partial X^2} + \frac{1}{AR}\frac{\partial^2 \Theta}{\partial Y^2}\right]. \tag{15}$$

The dimensionless boundary conditions for the problem at hand are:

$$X = 0, 0 < Y < 1: \Psi = 0, \Theta = 1, \tag{16a}$$
$$X = 1, 0 < Y < 1: \Psi = 0, \Theta = 0, \tag{16b}$$
$$0 < X < 1, Y = 0: \Psi = 0, \frac{\partial \theta}{\partial Y} = 0, \tag{16c}$$
$$0 < X < 1, Y = 1: \Psi = 0, \frac{\partial \theta}{\partial Y} = 0. \tag{16d}$$

The local and the average Nusselt numbers at the hot (left) wall are calculated from the following expressions:

$$Nu = \frac{hH}{k_f} = -\frac{k_{nf}}{k_f}AR\left[\frac{\partial \Theta}{\partial X}\right]_{Y=0}, \tag{17}$$

$$\overline{Nu} = \int_0^1 Nu dY. \tag{18}$$

**Heat Function**

The heat function, defined by Kimura and Bejan [8], can be easily generalized to nanofluids problems as:

$$-\frac{\partial h}{\partial x} = \rho_{nf}\, c_{p,nf}\, v(T - T_C) - k_{nf}\frac{\partial T}{\partial y}, \tag{19}$$

$$\frac{\partial h}{\partial y} = \rho_{nf}\, c_{p,nf}\, u(T - T_C) - k_{nf}\frac{\partial T}{\partial x}, \tag{20}$$

With $h$ being the heat function.

Adopting the dimensionless parameters defined by equation (13), the dimensionless form of equations (19) and (20) take the form of:

$$\frac{\partial \Pi}{\partial X} = \frac{\rho_{nf}\, c_{p,nf}}{\rho_f c_{p,f}}\theta\frac{\partial \Psi}{\partial X} + \frac{1}{AR}\frac{k_{nf}}{k_f}\frac{\partial \theta}{\partial Y}, \tag{21}$$

$$\frac{\partial \Pi}{\partial Y} = \frac{\rho_{nf}\, c_{p,nf}}{\rho_f c_{p,f}}\theta\frac{\partial \Psi}{\partial Y} - AR\frac{k_{nf}}{k_f}\frac{\partial \theta}{\partial X}, \tag{22}$$

where $\pi$ is the dimensionless heat function:

$$\Pi = \frac{h}{k_f(T_H - T_C)}. \tag{23}$$

Assuming $h$ to be a continuous function to its second-order derivatives, equations (21) and (22) lead to the following second-order differential equation for the dimensionless heat function:

$$\frac{\partial^2 \Pi}{\partial X^2} + \frac{\partial^2 \Pi}{\partial Y^2} = \frac{\rho_{nf}\, c_{p,nf}}{\rho_f c_{p,f}}\left[\frac{\partial}{\partial X}\left(\theta\frac{\partial \Psi}{\partial X}\right) + \frac{\partial}{\partial Y}\left(\theta\frac{\partial \Psi}{\partial Y}\right)\right] + \left(\frac{1}{AR} - AR\right)\frac{k_{nf}}{k_f}\frac{\partial^2 \theta}{\partial X \partial Y} \tag{24}$$

With this definition of the heat function, the positive sign of $\pi$ denotes counter-clockwise heat flow while clockwise heat flow is represented by the negative sign of $\pi$.

The boundary conditions for the dimensionless heat function equation can be obtained from the integration of equations (21) and (22) along the enclosure boundary that yields:

$$0 < X < 1, Y = 0:\ \Pi(X,0) = \Pi(0,0) \quad (25a)$$

$$0 < X < 1, Y = 1: \Pi(X,1) = \Pi(0,1), \quad (25b)$$

$X = 0, 0 < Y < 1$:

$$\Pi(0,Y) = \Pi(0,0) - \int_0^Y AR\frac{k_{nf}}{k_f}\frac{\partial\theta}{\partial X}dY = \Pi(0,0) + \int_0^Y Nu.dY, \quad (25c)$$

$X = 1, 0 < Y < 1$:

$$\Pi(1,Y) = \Pi(1,0) - \int_0^Y AR\frac{k_{nf}}{k_f}\frac{\partial\theta}{\partial X}dY = \Pi(1,0) + \int_0^Y Nu.dY \quad (25d)$$

An important point in the determination of heat function goes back to its reference value. In this study, the value of heat function at the origin point is assumed to be $\pi(0, 0) = 0$.

Solution of equation (24) yields the values of the dimensionless heat function for the nodes inside the enclosure while drawing of the iso-lines of the heat function generates heatlines.

## 3. Solution Procedure

The resulting dimensionless partial differntial equations (equations (14), (15), and (24)) are solved simultaneously along with the corresponding boundary conditions (equations (16) and (25)). For this purpose, a control-volume based computational procedure is used. The governing equations are converted into a system of algebraic equations through integration over each control volume. The algebraic equations are solved by a line-by-line iterative method. The method sweeps the domain of integration along the *x* and *y* axes and uses Tri-Diagonal Matrix Algorithm (TDMA) to solve the system of equations. The employed FORTRAN code is essentially a modified version of a code built and validated in previous works [17-19]. The convergence criterion employed is the maximum residuals of all variables which must be less than $10^{-5}$. To obtain a grid suitable for the range of Darcy-Rayleigh number studied here, a grid independence test is performed. It was observed that refinement of grid from 200 x 200 to 300 x 300 may not change the average Nusselt number values more than 1%. Thereby, a 200 x 200 grid is selected for the current computations.

## 4. Simulation Results

Since this is the first study on the application of heat function on buoyancy driven flows inside nanofluid-saturated porous enclosures, no previous results are available for the purpose of validation. Hence, the accuracy of the developed code is firstly tested with the classical natural convection heat transfer of pure fluid ($\phi = 0$) in a square porous enclosure with differentially-heated vertical walls and insulated horizontal walls. Accordingly, the obtained numerical values for the dimensionless temperature ($\phi$) at the adiabatic walls are compared with those of Badruddin *et al.* [20] in Figure 2. As can be observed, current results are in excellent agreement with previously published works. Additionally, the validity of this solver, in the computation of nanofluid flows, is examined. For this purpose, natural convection heat transfer of Cu-water nanofluid in a triangular enclosure is computed and the obtained numerical values for the average Nusselt number are compared with those given by other authors in Table 2. As can be observed, current results are in excellent agreement with previously published works. Moreover, contour plots of stream function and temperature are almost the same as those reported in open literature. They are not, however, presented here for the sake of brevity. This provides confidence to the developed code for further studies. Consequently, in what follows, the code is utilized for the analysis of the nanofluid-saturated porous enclosure depicted in Figure 1.

Simulation results in terms of dimensionless distributions of streamlines ($\psi$), isothermal lines ($\theta$), and heatlines $\pi$ for Cu-water, $Al_2O_3$-water, and $TiO_2$-water nanofluids in a square porous enclosure (i.e., with *AR = 1*) are indicated in Figure 3 that corresponds to *Ra* = 10 and $\phi = 0.1$. Here, the results of the pure water are also provided by the dashed lines for comparison. Moreover, numerical values of $|\Psi_{max}|$ and $\overline{Nu}$ for each case are illustrated.

**Table 2.** Comparison of the average Nusselt number in a nanofluid-saturated porous triangular enclosure with previously published works.

| | *Ra* = 500 | | *Ra* = 1000 | |
|---|---|---|---|---|
| | $\phi = 0$ | $\phi = 0.2$ | $\phi = 0$ | $\phi = 0.2$ |
| Sun and Pop [1] | 9.66 | 9.42 | 13.9 | 12.85 |
| Chamkha and Ismael [2] | 9.52 | 9.44 | 13.6 | 12.82 |
| Present study | 9.53 | 9.41 | 13.67 | 12.81 |

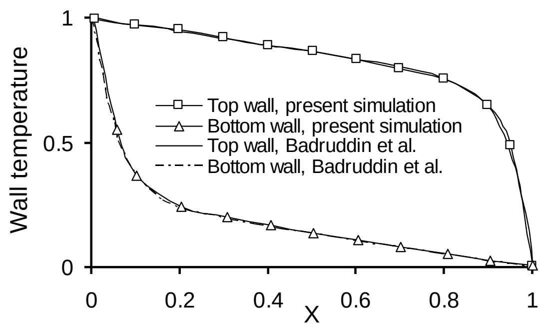


**Figure 2.** Computed adiabatic wall temperature compared with simulation results of Badruddin *et al.* [20].

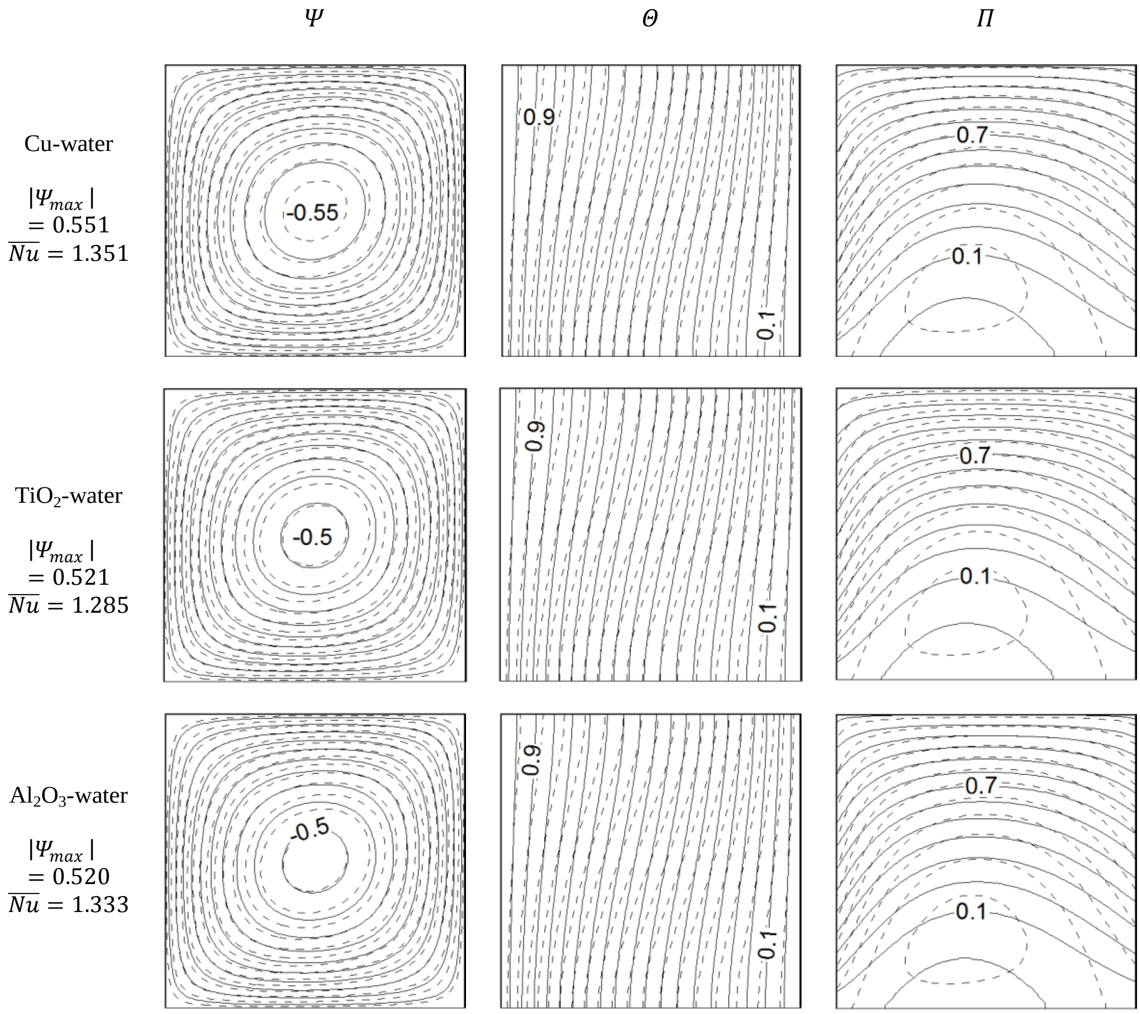


**Figure 3.** Distributions of streamlines, isothermal lines, and heatlines at $Ra = 10$ with $\phi = 0.1$ and $AR = 1$ (dashed lines correspond to pure water with $|\Psi_{max}| = 0.725$ and $\overline{Nu} = 1.067$).

The inspection of the streamlines as well as the isothermal lines demonstrates that close to the hot wall (i.e., the left wall), the fluid becomes heated and expands. This gives rise to an ascending motion. The fluid then changes its direction when reaching the neighborhood of the adiabatic wall. Thereafter, it releases heat at the cold wall (i.e., the right wall), becomes denser, and sinks down. These happenings result in the establishment of a closed-loop for fluid flow which transfers heat from the hot wall to the cold wall.

The combined effect of the fluid circulation and temperature distribution on the heat flow inside the enclosure is presented by the contour plots of heatlines. It is observed that heatlines emanate from hot wall and end on the cold wall implying the heat transport between the enclosure and its environment with no significant thermal mixing inside the enclosure.

The influence of nanoparticles on the buoyancy-driven flow is obvious. It is evident that with addition of the particles to the base fluid (i.e., water), the strength of the buoyancy-driven flow diminishes up to about 28%. Such an observation is in accord with the experimental evidence of Putra *et al.* [21] in non-porous environments and is attributed to the fact that densities of the current nanofluids are much higher than that of water. In spite of the observed decrease in $|\Psi_{max}|$, one may find up to about 27% increase in $\overline{Nu}$ with the particles addition. This is not a surprising effect due to the improvement of the thermal conductivity in this low-*Ra* environment.

To examine this behavior under different Darcy-Rayliegh numbers, the streamlines, isothermal lines, and heatlines for *Ra* = 100 and *Ra* = 1000 are plotted in Figures 4 and 5, respectively. Comparing the results of these figures with those in Figure 3 indicates that, at *Ra* = 10, the conduction heat transfer mechanism is dominant and the isotherms are nearly parallel to the vertical walls. The domination of conduction heat transfer in this low-*Ra* circumstance can also be observed in the heatline pattern since no passive area exists. It can be witnessed that with the increase in *Ra*, the flow strength enhances and thereby, the isotherms become gradually distorted. This also leads to the clustering of the heatlines from the hot to the cold wall and generates passive heat transfer area in which heat is rotated without having significant effect on heat transfer between the walls. Dense heatlines appearing in the vicinity of the mid parts of the vertical walls at *Ra* = 1000 depict higher heat transfer rates there. It is interesting to observe that, with the increase in *Ra*, the pattern of the heatlines approaches to that of the streamlines; this is attributed to the domination of the convective mode of heat transport.

The inspection of the numerical values of $|\Psi_{max}|$ and $\overline{Nu}$ for the current nanofluids and those of pure water at $R_a = 100$ demonstrates up to about 16% decrease in $|\Psi_{max}|$ and up to about 15% decrease in $\overline{Nu}$ with the particles addition. At $Ra = 1000$; however, these diminishments take the values of 8% and 10%, respectively. This indicates that, with the increase in the Darcy-Rayleigh number, the effect of particles addition decreases.

Comparing the results of the current nanofluids leads one to conclude that the Cu-water nanofluid produces higher heat transfer rates in all circumstances. This is more clearly demonstrated in Figures 6 and 7 wherein the numerical values of the average Nusselt number for the three nanofluids in a wide range of nanoparticle fraction ($0< \phi <0.2$) and Darcy-Rayliegh number ($10< Ra <1000$) are provided. The physical reasoning for this behavior is the higher thermal conductivity of the Cu nanoparticles (see Table 1) and is in accord with the previous observations of Cho *et al.* [22].

Finally, the effect of enclosure aspect ratio on the buoyancy-driven flow is analyzed. To this aim, simulation results of $AR = 4$ are compared with those of $AR = 1$ in Figure 8. The presented results correspond to $Ra = 100$ and $\phi = 0.1$.

The influence of enclosure aspect ratio on the establishment of flow and thermal fields as well as heat transport path inside the enclosure is obvious. Comparing the numerical values of $|\Psi_{max}|$ and $\overline{Nu}$ in this Figure with those of Figure 4 indicates that with the increase in the enclosure aspect ratio, the strength of the buoyancy-driven flow decreases but the corresponding heat transfer rate enhances. The heat transfer enhancement occurs as a consequence of increase in the surface area of the non-adiabatic walls with respect to the adiabatic ones and is also observable from the dense heatlines in Figure 8. This is more clearly demonstrated in Figure 9 wherein the variations of the average Nusselt number with the enclosure aspect ratio for the current nanofluids are plotted. The figure indicates that in all of the analyzed enclosures, the Cu-water nanofluid produces higher heat transfer rates.

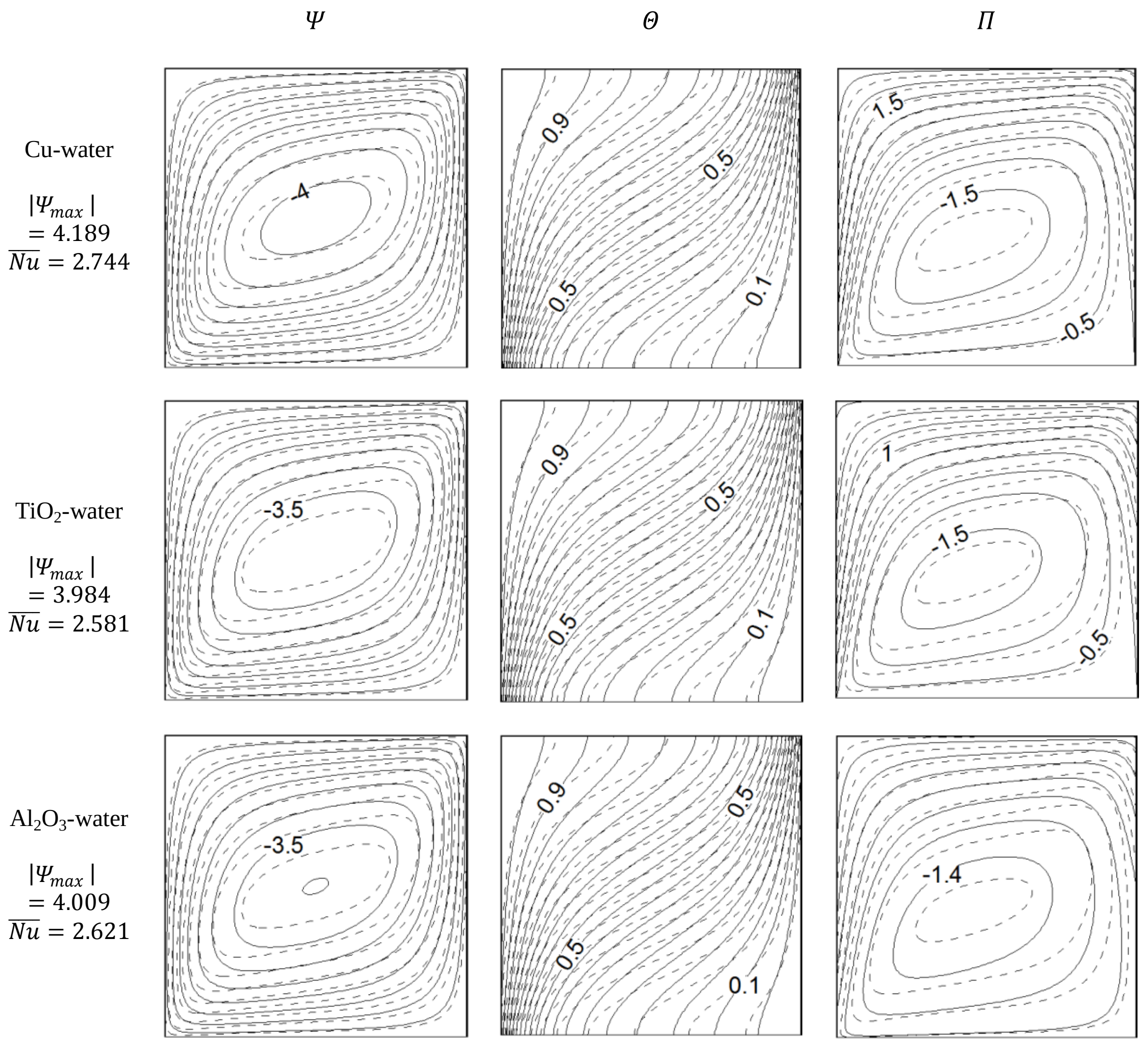


**Figure 4.** Distributions of streamlines, isothermal lines, and heatlines at $Ra = 100$ with $\phi = 0.1$ and $AR = 1$ (dashed lines correspond to pure water with $|\Psi_{max}| = 4.746$ and $\overline{Nu} = 3.025$).

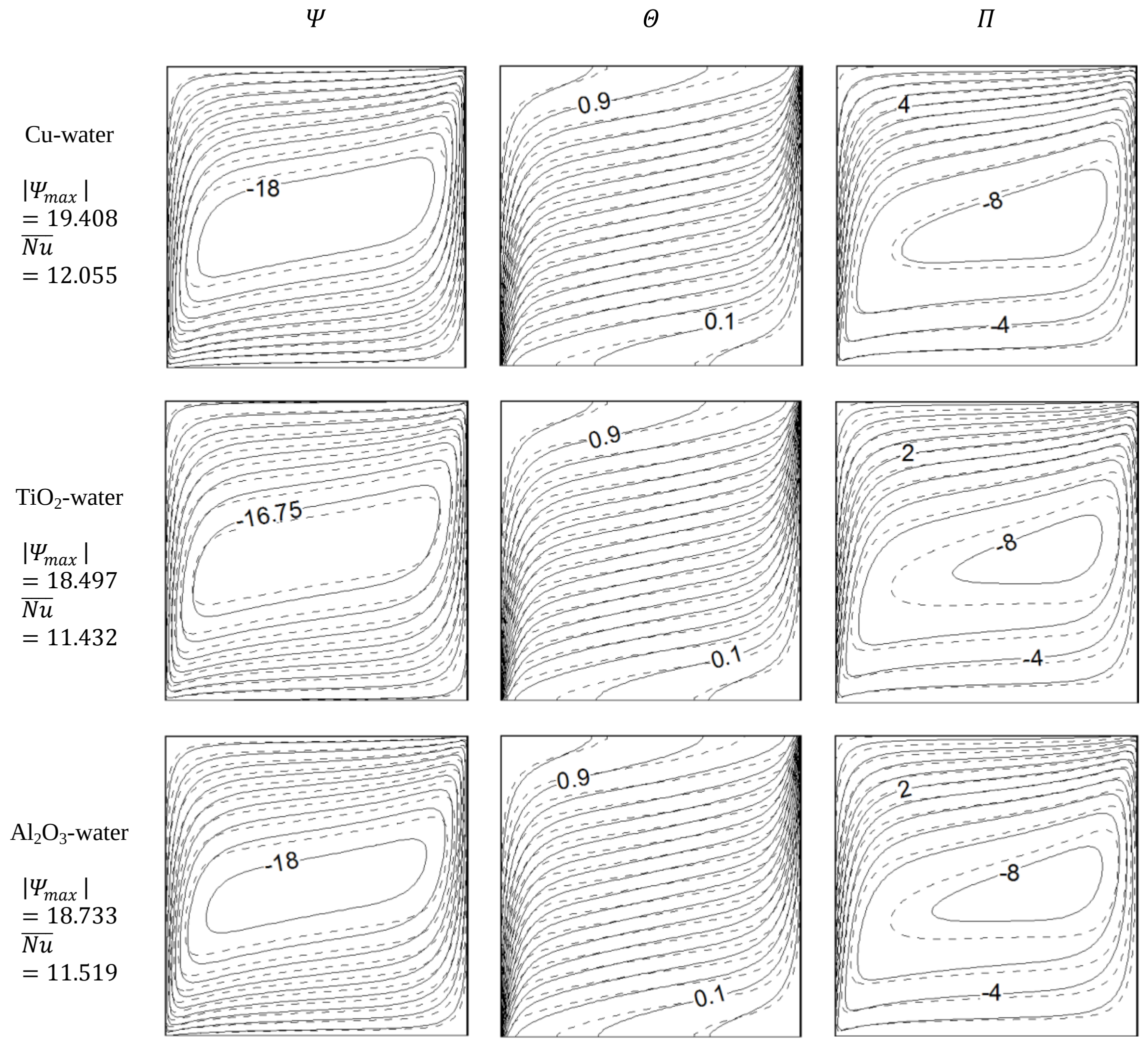


**Figure 5.** Distributions of streamlines, isothermal lines, and heatlines at $Ra = 1000$ with $\phi = 0.1$ and $AR = 1$ (dashed lines correspond to pure water with $|\Psi_{max}| = 20.071$ and $\overline{Nu} = 12.697$).

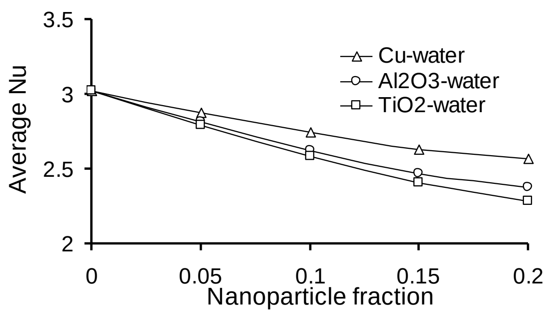


**Figure 6.** Variations of the average Nusselt number with nanoparticle fraction for the current nanofluids at $Ra = 100$

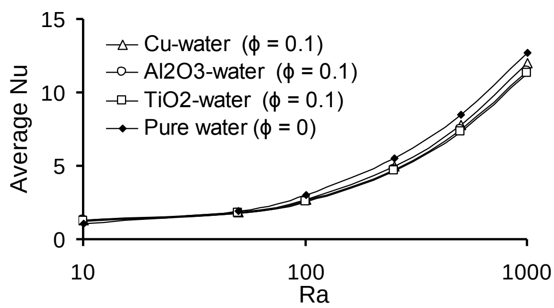


**Figure 7.** Variations of the average Nusselt number with Darcy-Rayliegh number for the current nanofluids with $\phi = 0.1$

 

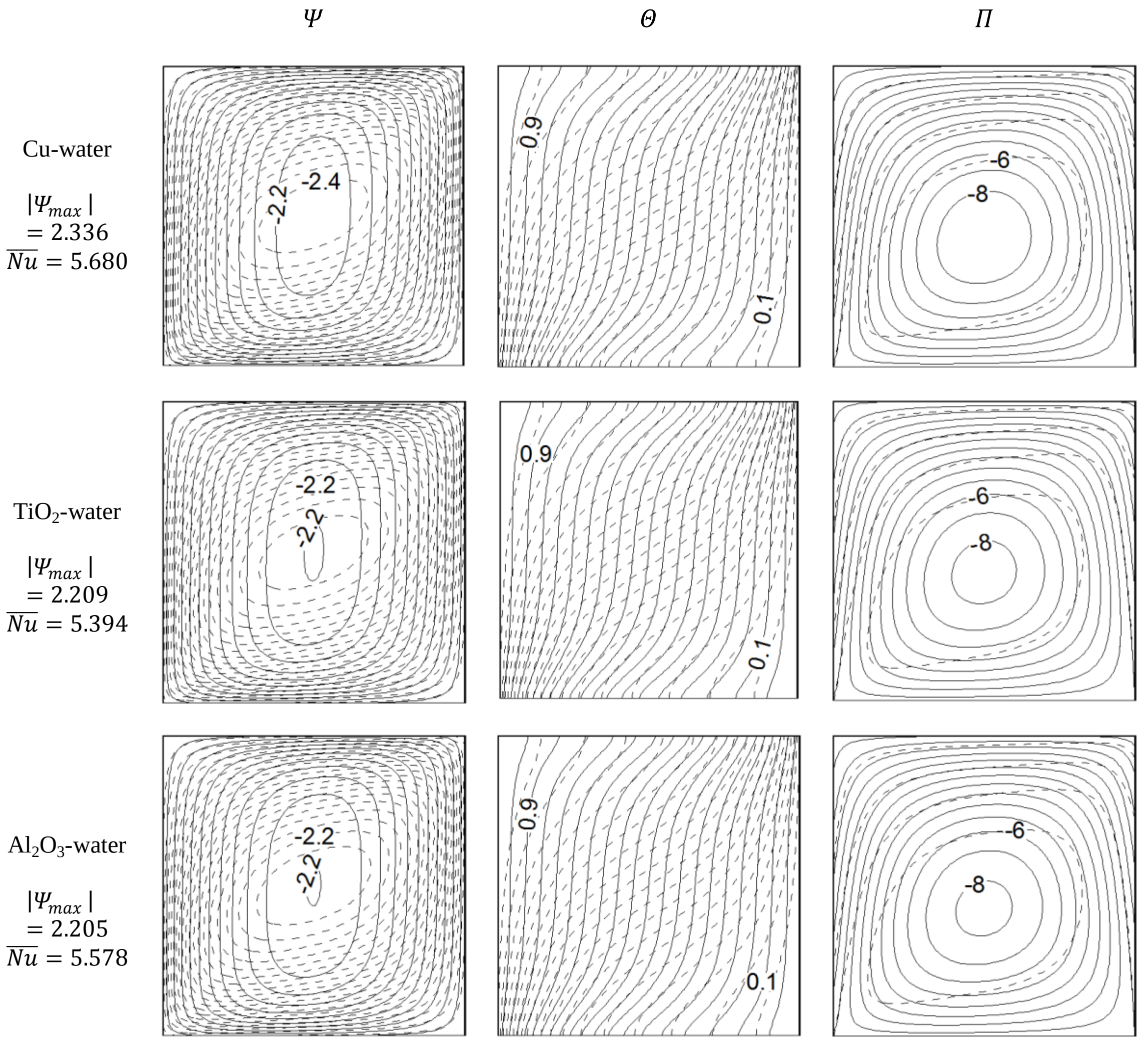


**Figure 8.** Distributions of streamlines, isothermal lines, and heatlines at $Ra = 100$ with $\phi = 0.1$ and $AR = 4$ (dashed lines correspond to the same nanofluid but with $AR = 1$).

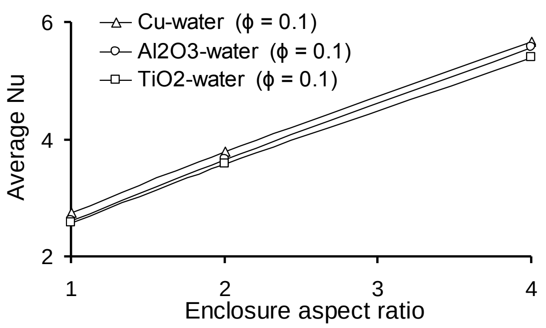


**Figure 9.** Effect of enclosure aspect ratio on the average Nusselt number at $Ra = 100$.

## 5. Concluding Remarks

The heatline visualization technique and its application to buoyancy-driven flow inside a nanofluid-saturated porous enclosure were discussed in the present study. Simulation results in terms of dimensionless distributions of streamlines, isothermal lines, and heatlines as well as numerical values of $|\Psi_{max}|$ and $\overline{Nu}$ for Cu-water, $Al_2O_3$-water, and $TiO_2$-water nanofluids were compared with those of pure water under different Darcy-Rayleigh numbers. Additionally, the consequences of the enclosure aspect ratio on the buoyancy-driven flow were clarified. Inspection of the presented results indicated how the establishment of the flow and thermal fields as well as the path of heat flow inside the enclosure may be influenced by the presence of the nanoparticles. It is found that among the current nanofluids, the Cu-water one produces higher heat transfer rates that is attributed to higher thermal conductivity of the Cu nanoparticles.

## References

[1] Q. Sun, I. Pop, “Free convection in a triangle cavity filled with a porous medium saturated with nanofluids with flush mounted heater on the wall”. International Journal of Thermal Sciences, Vol. 50 (2011) No. 11, 2141-2153.

[2] A.J. Chamkha, M.A. Ismael, “Conjugate heat transfer in a porous cavity filled with nanofluids and heated by a triangular thick wall”. International Journal of Thermal Sciences, Vol. 67 (2013) 135-151.

[3] S.E. Ahmed, A.M. Rashad, R.S.R. Gorla, "Natural convection in triangular enclosures filled with nanofluid saturated porous media". Journal of Thermophysics and Heat Transfer, 27 (2013) No. 4, 700-706.

[4] M.M. Rashidi, E. Momoniat, M. Ferdows, A. Basiriparsa, "Lie group solution for free convective flow of a nanofluid past a chemically reacting horizontal plate in a porous media". Mathematical Problems in Engineering, Article ID 239082 (2014).

[5] G.C. Bourantas, E.D. Skouras, V.C. Loukopoulos, V.N. Burganos, "Heat transfer and natural convection of nanofluids in porous media". European Journal of Mechanics-B/Fluids, 43 (2014) 45-56.

[6] M.A. Sheremet, I. Pop, M.M. Rahman, "Three-dimensional natural convection in a porous enclosure filled with a nanofluid using Buongiorno's mathematical model". International Journal of Heat and Mass Transfer, Vol. 82 (2015) 396-405.

[7] M.T. Nguyen, A.M. Aly, W.W. Lee, "Natural convection in a non-Darcy porous cavity filled with Cu-water nanofluid using the characteristic-based split procedure in finite-element method". Numerical Heat Transfer, Part A, Vol. 67 (2015) No. 2, 224-247.

[8] S. Kimura, A. Bejan, "The "heatline" visualization of convective heat transfer". Journal of Heat Transfer, Vol. 105 (1983) No. 4, 916-919.

[9] H. Saleh, I. Hashim, "Heatline visualization of natural convection in an inclined square porous enclosure with sinusoidal boundary conditions". Journal of Porous Media, Vol. 16 (2013) No. 10, 875-885.

[10] H. Saleh, I. Hashim, "Heatline visualization of conjugate heat transfer in square porous enclosure". Journal of Porous Media, Vol. 16 (2013) No. 12, 1119-1132.

[11] T. Basak, A.K. Singh, T.P.A. Sruthi, S. Roy, "Finite element simulations on heat flow visualization and entropy generation during natural convection in inclined square cavities". International Communications in Heat and Mass Transfer, Vol. 51 (2014) 1-8.

[12] M.M. Rahman, H.F. Oztop, S. Mekhilef, R. Saidur, J. Orfi, "Simulation of unsteady heat and mass transport with heatline and massline in a partially heated open cavity". Applied Mathematical Modelling, Vol. 39 (2015) No. 5-6, 1597-1615.

[13] H.M. Duwairi, O. Abu-Zeid, R.A. Damesh, "Viscous and Joule heating effects over an isothermal cone in saturated porous media". Jordan Journal of Mechanical and Industrial Engineering, Vol. 1 (2007) No. 2, 113-118.

[14] M.M. Rashidi, O. Anwar Beg., N. Rahimzadeh, "A generalized differential transform method for combined free and forced convection flow about inclined surfaces in porous media". Chemical Engineering Communications, Vol. 199 (2012) No. 2, 257-282.

[15] H.C. Brinkman, "The viscosity of concentrated suspensions and solutions". Journal of Chemical Physics, Vol. 20 (1952) No. 4, 571-581.

[16] Maxwell J. A treatise on electricity and magnetism. 2nd ed. Cambridge: Oxford University Press; 1904.

[17] I. Zahmatkesh, "On the importance of thermal boundary conditions in heat transfer and entropy generation for natural convection inside a porous enclosure". International Journal of Thermal Sciences, Vol. 47 (2008) No. 3, 339-346.

[18] I. Zahmatkesh, "Dependence of buoyancy-driven flow inside an oblique porous cavity on its orientation". Emirates Journal for Engineering Research, Vol. 18 (2013) No. 2, 53-61.

[19] I. Zahmatkesh, "Effect of a thin fin on natural convection heat transfer in a thermally stratified porous layer". Emirates Journal for Engineering Research, Vol. 19 (2014) No. 2, 57-64.

[20] I.A. Badruddin, Z.A. Zainal, P.A.A. Narayana, K.N. Seetharamu, "Heat transfer in porous cavity under the influence of radiation and viscous dissipation". International Communications in Heat and Mass Transfer, Vol. 33 (2006) No. 4, 491-499.

[21] N. Putra, W. Roetzel, S.K. Das, "Natural convection of nano-fluids". Heat and Mass Transfer, Vol. 39 (2003) No. 8-9, 775-784.

[22] C.C Cho, C.L. Chen, C.K. Chen, "Natural convection heat transfer and entropy generation in wavy-wall enclosure containing water-based nanofluid". International Journal of Heat and Mass Transfer, Vol. 61 (2013) 749-758.

المملكة الأردنية الهاشمية

الجامعة الهاشمية

# المجلة الأردنية
# للهندسة الميكانيكية والصناعية

# JJMIE

**مجلة علمية عالمية محكمة**

تصدر بدعم من صندوق البحث العلمي

http://jjmie.hu.edu.jo/

ISSN 1995-6665

# المجلة الأردنية للهندسة الميكانيكية والصناعية

## مجلة علمية عالمية محكمة

المجلة الأردنية للهندسة الميكانيكية والصناعية: مجلة علمية عالمية محكمة تصدر عن الجامعة الهاشمية بالتعاون مع صندوق دعم البحث العلمي في الأردن



**ترسل البحوث إلى العنوان التالي**


رئيس تحرير المجلة الأردنية للهندسة الميكانيكية و الصناعية

الجامعة الهاشمية

كلية الهندسة

قسم الهندسة الميكانيكية

الزرقاء - الأردن

هاتف : 00962 5 3903333 فرعي 4537

Email: jjmie@hu.edu.jo

Website: www.jjmie.hu.edu.jo